Università degli Studi di Firenze

DOTTORATO DI RICERCA IN
"*Spettroscopia Atomica e Molecolare*"

CICLO XXV

COORDINATORE Prof. Francesco Pavone

Transport in complex heterogeneous photonic structures

Settore Scientifico Disciplinare FIS/03

Dottorando
Dott. Romolo Savo

Tutore
Prof. Diederik S. Wiersma

Anni 2010/2012

Abstract

Proper understanding of multiple scattering of light is essential in many areas of science and technology. The interest ranges from fundamental photonics and the quest for the elusive phenomena of Anderson localization, to atmospherical optics and climate research, to applied spectroscopy. In biomedical optics, proper account of light scattering is necessary to extract information on crucial parameters such as blood oxygenation and hemoglobin concentration. In industry, non-destructive testing of e.g. food products or pharmaceuticals involve spectroscopic measurements on materials in which light is multiply scattered. This broad interest is reflected by an enormous body of science regarding light transport in turbid media. Typically, light transport is in these areas is viewed as a random walk based on independent and exponential distributed steps, and that the diffusion constant is given by the famous relation $D = \frac{1}{3} v_E l_t$ (where v_E is the energy velocity and l_t the average length of the exponential steps). This picture is appropriate for systems where scatterers are uniformly, but randomly, distributed in space. However, there are many systems in which scatterers are not uniformly distributed. An obvious example is our atmosphere, having complex cloud layers that determines our earth's solar energy balance. In recent years, such aspects of light transport are receiving increasing attention, and an area that could be referred to as anomalous transport of light has been formed. Along with the current interest in super-diffusion coming from the atmospherical optics community, the recent introduction of well-controlled heterogeneous laboratory systems with superdiffusive properties (so called Lévy glass [1]) has further increased the interest in this topic. However, how heterogeneous distributions of scatterers influence light transport remains poorly understood. The main aim of this thesis is to fill this gap, both experimentally and theoretically.

Since full understanding of transport requires information on dynamics, a main target has been to develop a time-resolved system capable of study-

ing light transport in strongly heterogeneous systems such as Lévy glasses. To study the transmission through a Lévy glass, very high time-resolution is required, and the system constructed and used within the frame of this thesis is based on femtosecond lasers and optical gating, achieving excellent temporal stability, time-resolution on the order of 100 fs and good control over light injection and collection. The system is described in detail in Chapter 3. Extensive experimental work on the features of transport in Lévy glasses has been carried out and is reported in Chapter 4 (material currently being prepared for publication). In short, this chapter reports on the first observation of dynamical signatures of superdiffusion for light, obtained by observing the dependence on the sample thickness of the time-resolved transmission. This work also show that the typical scaling exponents of such dependence are sensitive to the degree of heterogeneity of the sample. Theoretically, large efforts have been directed towards developing rigorous models of transport in heterogeneous systems (one aim being to have something to compare experiments with). The outcome of these efforts is a solid probabilistic account of transport in complex heterogeneous systems, available as an arXiv preprint [2] and is under review for Physical Review E (here given in Chapter 5). There, we provide an analytical expression for the diffusion constant in holey systems having the form of sphere packings (in case of weak step correlations), and discuss the role of step correlations and finite sample size.

Although the main aim was to explore light transport in complex turbid materials, the high performance and careful control of the time-resolved instrumentation also opened for making other interesting contributions to the field of multiple scattering and diffuse optics. While some of these contribution are still to be finished, there are already two papers accepted. In the first article, published in Applied Physics B [3], the setup was used to measure the optical properties of strongly scattering nanoporous zirconia ceramics, revealing how small changes in pore size (from 50 to 150 nm) influence scattering strength (transport mean free paths ranging from 2.3 to 1.2 microns at 810 nm). This work is discussed in Section 3.7. The second article, accepted for Optics Letters [4], deals with the more general problem of dynamics of transport through media with homogeneously distributed scatterers. There, we show that careful assessment of early dynamics can reveal single scattering characteristics (scattering mean free path l_s and single scattering anisotropy g) even in regimes normally considered to be fully diffusive and where the similarity relations of diffuse light transport suggests that these parameters are inaccessible. The key here is, of course, not a flaw in the similarity relation, but that the diffusion approximation does not hold for the first light propagating through the system. The opportunity of resolving the ambiguity in g and l_s by looking at early dynamics was discussed already in the classic paper of Paterson, Wilson and Chance [5], but has remained unexplored due to the though experimental requirements. Our contribution on this is therefore of broad general interest, since single scattering properties often are of diagnostic value in material characterization.

This important contribution is covered in Chapter 6.

Contents

Introduction

The appearance of objects depends on how light interacts with them. Phenomena like absorption, reflection, refraction or scattering determine the properties of the images that we perceive. Scattering in particular. The single scattering from a small particle can be seen as a diffraction phenomena spreading light all around. For example the molecules floating in the atmosphere produce single scattering of solar light, which is particularly efficient in the blue region of the spectrum and gives to the sky its color. Even clouds owe their color to scattering, but in this case solar light interacts multiple times with the condensed water droplets before exiting the medium. This multiple scattering interaction often turns out to be efficient over the whole visible spectrum, giving to the object a white appearance. Together with clouds also snow, milk, paper and foams look white because of multiple scattering. Multiple scattering of light is widespread and many other media multiply scatter light even if they do not appear white. This is the case for biological tissues, wood and concrete, where the absorption dominates in determining the color.

In general, media characterized by a microscopic heterogeneity induce multiple scattering of light. This can be seen as a consequence of the spatial fluctuation of the refractive index, which prevents light to propagate undisturbed. Many of these media are significantly disordered and the spatial variation of the refractive index is essentially random. This class of materials is often referred to as turbid media or (optically) disordered media. The investigation of light transport in disordered media is a wide field of research. It includes atmospherical optics, biomedical optics and material science. Light and disorder have also been an important tool of investigation for basic scientific problematics like the Anderson localization.

A powerful picture of the optical properties of disordered media is provided by an ensemble of single point scatterers randomly distributed in space. Light transport in such environment can be described as a random walk of

"energy packets" bouncing around through the scatterers. The particular spatial distribution of the scatterers determines the step-length distribution of the random walk, which plays an essential role in the transport properties. It is well known that in homogeneous disordered media, where scatterers are uniformly distributed, step lengths are exponentially distributed around the scattering mean free path l_s. This length gives the typical size of the steps, defining a local region where the next scattering event will most likely take place. In this condition transport is inherently local and as a consequence of the Central-Limit Theorem it becomes diffusive.

However, many turbid media are far from being homogeneously disordered, since they are characterized by a position dependent density of scatterers. In this media the (optical) heterogeneity is (spatially) heterogeneous, a situation which can be modeled by the presence of voids between scatterers creating free-propagation regions for light. Many biological tissues are heterogeneous in this sense, especially the brain tissue. Heterogenous disorder is also characteristic of foams, colloids, polymers, paper and pharmaceutical tablets, which are all materials of interest for industry and used in technology. This kind of double heterogeneity affect the step-length distribution of light, which is not anymore a simple exponential as in homogeneous disordered media. A complete understanding of light transport in heterogeneous disorder is lacking and the necessity of contributions in this fields is fueled by the interest in basic science as well as by the potential applications in novel method for spectroscopy.

An extreme side of heterogeneity is represented by fractals, which are complex structures whose heterogeneity is spread over many length scales in a self-similar fashion. Many important disordered systems can be thought as fractals in a statistical sense, having a power law distribution of the size of the heterogeneities. One example is the cloudy atmosphere, where clouds define scattering layers for solar light separated by a very broad distribution of distances. Others are polymers and porous materials which may present self-similarity on certain length scales. Transport on fractals is expected to be *anomalous* compared to the diffusion typical of homogeneous disordered media. This can be due to trapping effects or on contrary to a heavy non-local coupling probability in the transport process. Standard laws of diffusion need to be generalized, requiring the constructive comparison between models and experimental observations. However a direct and accurate characterization of light transport in many fractal systems can be extremely challenging. The interest in characterizing and understanding transport in fractals goes even beyond optics and wave scattering phenomena. Indeed it is emerging that relevant complex networks as the Internet, DNA assemblies, living cells and fractures in rocks have a fractal-like topology. Transport in all these systems is based on the same statistical random walk process, giving to the investigation of light transport in fractals a wide and general value. Transport laws observed for light could be applied to describe processes like transfer of information or money and the spreading of diseases.

In this work we employ the tools of photonics to investigate the basic

laws of transport in disordered fractal-like systems. The idea is to create an optical analogue of a relevant model of complexity and use light as an investigation tool. We have experimentally investigated light transport in optically disordered materials dubbed Lévy glasses, where disorder is engineered to obtain a fractal-like heterogeneity. We have focused on the dynamic properties of light transport, which have been probed by means of ultrafast time-resolved transmission measurement. A considerable effort has been dedicated to the design and implementation of the experimental setup, which is based on a non-linear optical gating technique.

In parallel we have developed a general theoretical framework for accounting of the effects of heterogeneities in turbid media even in the diffusive regime. Indeed if the heterogeneities have a typical size, which is smaller than the size of the systems, the diffusive nature of transport is untouched. However, a common assumption is that the characteristic parameters of diffusion are kept unchanged, like the scattering mean free path and diffusion constant. Part of the work presented here is a theoretical and numerical investigation on the effects of heterogeneities on these parameters.

Even in homogeneous disordered media diffusive transport breaks down when the thickness of the sample is few times the scattering mean free path. This effect is usually observable looking at the light crossing the media with few scattering events, which is the first detected signal in a time-resolved transmission measurement. In the last part of this work we have investigated, experimentally and numerically, the influence of single scattering properties on the multiply scattered light in such transport regime. We have focused on the possibility to assess information on both the single scattering anisotropy and the diffusion constant by using one single measurement. The possibility to simultaneously retrieve these two information could dramatically improve the diagnostic capabilities of diffusive time-resolved spectroscopy.

CHAPTER 1

Light transport in disordered media

Light propagation in dielectric media is governed by Maxwell's equations [6] [7]. At the macroscale the interaction between the electromagnetic field and the atoms can be included in the dielectric constant $\epsilon(\mathbf{r})$. In homogeneous media $\epsilon(\mathbf{r})$ is constant in space and its main effect is to vary the velocity of light propagation (for real ϵ). When instead ϵ presents a local abrupt alteration light *scatters*. Scattering can be seen as a diffraction phenomena from a point object spreading light all around.

Heterogeneous dielectric media, which here we consider non-dissipative and non-magnetic, have a position-dependent dielectric constant, which fluctuates around a mean value. Usually ϵ is decomposed as $\epsilon(\mathbf{r}) = \overline{\epsilon} + \delta\epsilon(\mathbf{r})$. The fluctuating term $\delta\epsilon(\mathbf{r})$ is what generate scattering in the medium. When the fluctuation is strong the medium becomes optically turbid.

Turbid media can be described as an ensemble of single point scatterers distributed in a disordered fashion. To derive the electromagnetic field in the medium we would need a precise knowledge of the scatterers position and then we should face a very complicated analytical problem solving Maxwell's equations. This should be done for example when shining light on a sheet of paper. However if we could also retrieve the information of the scatterers position, in a certain region, and solve the equations, the result would change moving on the paper, since the position of the scatterers changes due to disorder.

This is why a stochastic approach is more useful. In disordered media scatterers are assumed to be randomly distributed, and propagation of light equivalent to a random walk. The optical transport properties are included in the statistics of the scattterers spatial distribution. For example when scatterers are uniformly distributed the transport is diffusive.

In this chapter we will introduce the basic concepts to describe the in-

teraction of light with disorder. The aim to draw the link between single scattering, multiple scattering and diffusion.

1.1 Single scattering

Consider a plane wave encountering a single scatterer. The far field can be decomposed in a first term given by the incoming field and in a scattered field in the form of a spherical wave [8]

$$E(\mathbf{r}) = e^{i\mathbf{k}\cdot\mathbf{r}} + \frac{e^{ik_0 r}}{r} f(\mathbf{k}, \mathbf{k}').fig. \tag{1.1}$$

We have considered one polarization direction and treated the electromagnetic field as a scalar field. Equation 1.1 defines the *scattering amplitude* $f(\mathbf{k}, \mathbf{k}')$ [m]. The scattering amplitude depends on the incident direction $\mathbf{k}$, on the direction of scattering $\mathbf{k}'$ and on the free-space wavelength $k_0 = 2\pi/\lambda$. Since we consider elastic collision the modulus k_0 of the wave vector $\mathbf{k}$ is conserved, hence $k_0 = |\mathbf{k}| = |\mathbf{k}'|$. In the general case of vectorial fields the scattering amplitude depends also on the incident polarization direction $\hat{\varepsilon}_i$, thus $f = f(k_0, \theta, \hat{\varepsilon}_i)$.

It can be often assumed that the scattering amplitude is independent from the incident direction $\mathbf{k}$. This is true for spherical scatterers or also, on average, when scatterers are randomly oriented. Further, it is commonly assumed that the scattering is symmetric for the azimuthal angle ϕ. Eventually the scattering depends only on the angle θ between $\mathbf{k}$ and $\mathbf{k}'$, as shown in fig. 1.1. If the scattering amplitude does not depend on θ the scattering is isotropic.

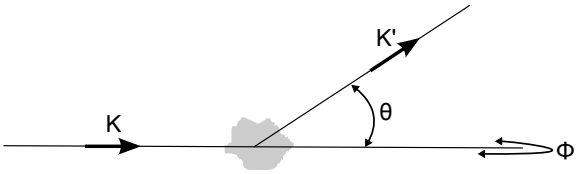

Figure 1.1 – Single scattering of a scalar plane wave. In the far field the probability to be scattered at an angle θ is given by the phase function $p(\cos\theta)$.

In order to characterize the scattering efficiency in the direction $\mathbf{k}'$ we consider the flux F_{out} of the scattered wave (flux of the Poynting vector), which gives the power scattered in that direction. We define the *differential scattering cross section* by the ratio between the flux emerging in an element $d\Omega$ of the solid angle and the incident flux F_{inc} per unit surface

$$\partial\sigma_s(\theta) = \frac{dF_{\text{out}}/d\Omega}{dF_{\text{inc}}/dS} \tag{1.2}$$

which have the dimension of [m^2]. In the far field the scattering cross section is equal to the square of the scattering amplitude

$$\partial\sigma_s(\theta) = |f(k_0, \theta)|^2 \tag{1.3}$$

where we do not specify the dependence on the wavelength. It then follows the definition of the *total scattering cross section*

$$\sigma_s = \int_\Omega \partial\sigma(\theta) d\Omega = 2\pi \int_0^\pi \partial\sigma(\theta) \sin\theta d\theta \tag{1.4}$$

which gives the total probability of scattering. The explicit expression of the scattering cross sections depends on the scatterer size (compared to the wavelength) and on scatterer shape. There are some cases in which the scattering cross sections can be analytically calculated, as for the Rayleigh and Mie scattering [9, 10].

Normalizing the differential scattering cross section with the scattering cross section yields the *scattering phase function*, which is usually expressed as a function of $\cos\theta$

$$p(\mathbf{k}, \mathbf{k}') = p(\cos\theta) = \frac{\partial\sigma_s(\theta)}{\sigma_s} \tag{1.5}$$

In the far field the scattering phase function is the normalized probability distribution to scatter at an angle θ from the incident direction. The average value of $\cos\theta$

$$g = \langle\cos\theta\rangle = \int_\Omega p(\cos\theta)\cos\theta d\Omega, \tag{1.6}$$

quantifies the scattering anisotropy, defining the *anisotropy factor* or *g-factor*. A g-factor equal to 0 indicates isotropic scattering while g-factor value equal to 1 indicates a completely forward scattering.

1.2 Multiple scattering

In the presence of disorder different scattering regimes are possible depending on the cross section of the single scatterer and on the scatterers density [6, 8, 9, 11–13]. When scatterers are dilute enough so that light exits the medium after having scattered once on average, there is a single scattering regime. If instead light undergoes multiple scattering events before leaving the medium, we are in a multiple scattering regime. Such difference is sketched in fig. 1.2.

In nature multiple scattering of light from disordered media is easily recognizable since objects looks white under the sun light. Indeed when deep in the multiple scattering regime the wavelength dependence of the single scatterer cross section never breaks down multiple scattering, thereby obtaining a broad band scattering response. Milk, snow, paper or also pharmaceutical tablets appear white because light is back-scattered at all optical frequencies. Also clouds are white because of multiple scattering of solar light on condensed water droplets. Their appearance contrasts the blue of the sky which instead is generated from single scattering with the atmosphere [15]. Foams as well appear white due to multiple scattering of light, see fig. 1.3.

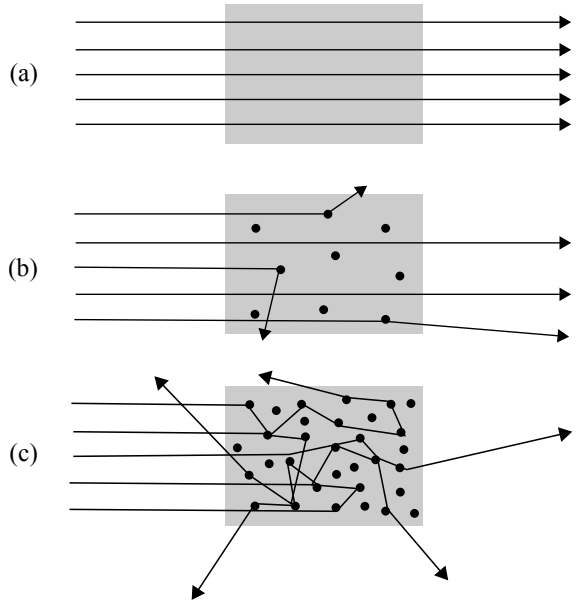

Figure 1.2 – Different scattering regimes induced by disorder. Light is sketched in the ray optics limit. (a) The medium is optically homogeneous and the refractive index n does not present abrupt alterations creating scattering. Waves propagate undisturbed with velocity $v = c_0/n$; (b) Single scattering regime: on average light scatters only once before leaving the sample. In this regime the optical properties of the medium are defined by the single scattering features; (c) Multiple scattering regime: multiple scattering events considerably increase the probability to be back-scattered at all wavelength and decrease the transmission probability. Light propagates along random paths as in a random walk. Picture modified from [14]

1.2.1 A random walk for light

One of the effect of scattering is to randomize the direction of propagation of the wave, see fig. 1.2(c). The more isotropic is the single scattering event the more efficient is the randomization. It thus follows, for the moment in an intuitive way, that the propagation of light in the multiple scattering regime is equivalent to a random walk. We can consider a collective effect of multiple scattering the definition of an infinite set of optical random paths which the light can follow to propagate into the medium. In a *mesoscopic* system [8], where the coherence length of light is longer than the typical travelled distances, each random path has, most probably, accumulated a different phase. As a consequence, in each point of the medium, many waves with random phase interfere. The intensity of light in a point $\mathbf{r}$ of the medium at time t is given by

$$I(\mathbf{r},t) = \frac{c_0 n_{\text{eff}}}{2} |\mathbf{E}_1(\mathbf{r},t) + \mathbf{E}_2(\mathbf{r},t) + \mathbf{E}_3(\mathbf{r},t) + \cdots|^2 \tag{1.7}$$

where the $\mathbf{E}_i(\mathbf{r},t)$ are the fields of the scattered waves, c_0 is the speed of light in vacuum and n_{eff} is the effective refractive index. The interference terms

Figure 1.3 – Multiple scattering of light is in our common landscapes. Clouds and the foam of breaking waves are white under the sun light because of multiple scattering. Picture courtesy of Max Orazi

emerging from the square of the modulus define a random distribution of regions with constructive and destructive interference. For instance this effect is observable in the far field of the transmission of a laser beam through a sheet of paper. In fig. 1.4(a) we show the typical intensity pattern we would observe, known as *speckle*. If we change the light injection point the speckle pattern changes. Iterating the procedure and averaging over enough positions, which represent different disorder configuration, the bright and dark spot disappear leaving place to an incoherent intensity profile 1.4(b). Averaging out of interference effects takes place in weak scattering conditions, thus when the distances between scatterers is much larger than the wavelength. It is also necessary that there is no positional correlation among the scatterers, which corresponds to a truly random disorder. When the interference contributions average to zero the field intensity in one point is the simple sum of the intensities of the scattered waves

$$I(\mathbf{r}, t) = I_1(\mathbf{r}, t) + I_2(\mathbf{r}, t) + I_3(\mathbf{r}, t) + \cdots \tag{1.8}$$

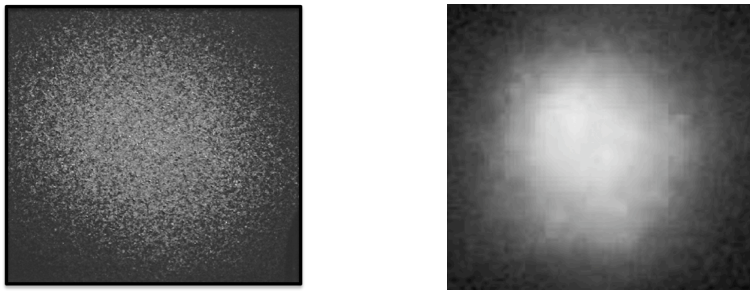

(a) (b)

Figure 1.4 – Average over disorder of interference affects in weak scattering conditions. (a) A typical speckle pattern: bright spots are given by constructive interference, while dark spot are the result of destructive interference between multiply scatter light. (b) Average over thousands of injection points of the obtained speckle patterns. What emerges is a incoherent transmission profile. Picture (b) modified from [1]

In this framework light transport in random media can be described by energy packets bouncing around as in a random walk. A real nature of the energy packets is inexistent and it would be incorrect to call them photons, since photons emerge from a quantization of the electromagnetic field. This is a misconception termed as the "photonic confusion" by Mishchenko for example [7, 13]. However, denominations like "photon random walk" and "photon migration" represent a rather established terminology. The concept of a random walk for light is a focal point in this work, always meaning that the average time-dependent light energy density distribution in the considered media, which is called the propagator, is equal to the one that would be obtained by a suitable random walk of fictitious particles carrying energy. Later on, in Section 1.3, we will introduce the radiative transfer

theory, which is a theoretical framework for a description of light transport based on a on the random walk model.

Since light propagates as a random walk we can associate to the multiple scattering process a step-length probability distribution, describing the distribution of distances light travels between two scattering events. The more suitable distribution to use depends on the topology of the disorder.

Although this description of light transport does not consider the phase of the wave, a coherent effect, the back-scattering enhancement, can be described by the random walk model. In this case the constructive interference of time-reversal paths, which have accumulated the same phase delay, creates an enhancement of the back-scattered light. This is also known as weak localization [16–18].

The wave nature of light becomes instead predominant, and the random walk model breaks down, when the scattering is so strong that on average light scatters before having completed one wavelength oscillation. This is the kind of disorder which can bring to Anderson localization [19].

1.2.2 Homogeneous disorder

Homogeneous disordered media are characterized by a random distribution of scatterers with a constant spatial density. In this disorder condition the multiple scattering process presents a typical distance between two scattering events, the *scattering mean free path* l_s, which is position independent. The scattering mean free path is linked to the single scattering properties by

$$l_s = \frac{1}{n\sigma_s} \tag{1.9}$$

where n is the number density of scatteres (number of scatterers in the unit volume) and σ_s the total scattering cross section of the single scatterer.

More precisely in homogeneous disordered media the step-length distribution of light $p(l)$ is exponential with mean value l_s

$$p(l) = \frac{1}{l_s} \exp\left(-\frac{l}{l_s}\right), \tag{1.10}$$

as stated by the Beer-Lambert law. Many light transport properties does not depend directly on l_s but on the average distance after which the propagation direction is completely randomized, which is called the transport mean free path l_t [20]. When the scattering is isotropic $l_t = l_s$ while for anisotropic scattering l_t is bigger than l_s being

$$l_t = \frac{l_s}{1-g} \tag{1.11}$$

where g is the anisotropy factor of eq. 1.6. The difference between l_s and l_t is sketched in fig. 1.5. In general transport is essentially determined by l_t, meaning that transport characterized by anisotropic scattering and scattering mean-free l_s, is equivalent to transport with isotropic scattering and

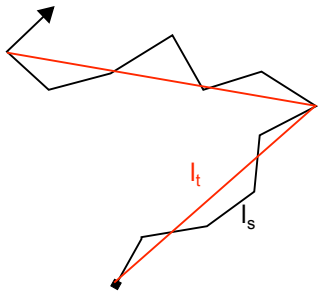

Figure 1.5 – Sketch of a multiple scattering process highlighting the difference between the scattering mean free path l_s and the transport mean free path l_t.

scattering mean free path equal to l_t. This is known as the *similarity relation*, which will be discusses more in detailed in Chapter 6.

Absorbtion

The Beer-Lambert law can be extended to media with absorption by considering the *absorption cross section* σ_a. Similarly to eq. 1.12 the average distance after which light is absorbed by the medium, the *absorption length* l_a, depends on σ_a as

$$l_a = \frac{1}{n\sigma_a} \tag{1.12}$$

When both scattering and absorption are present what defines the extinction of a light beam along the direction $\mathbf{k}$ is the *extinction cross section* [9]

$$\sigma_e = \sigma_s + \sigma_a \tag{1.13}$$

where all the quantities in the equation are a function of the wavelength. It follows that in presence of absorption the characteristic length entering the Beer-Lambert law is the *extinction length* l_e, given by

$$\frac{1}{l_e} = \frac{1}{l_s} + \frac{1}{l_a} \tag{1.14}$$

1.3 Radiative transfer

Radiative transfer theory is the general framework for describing light transport as an energy flow [13]. The radiative transfer equation (RTE) is the expression of the balance of energy inside a volume element of the scattering medium. To derive the equation we use the standard of expressing the scattering lengths l_s and l_a as scattering coefficient $\mu_s = 1/l_s$ and absorption coefficient $\mu_a = 1/l_a$. The energy balance is derived for the radiance $L = L(\mathbf{r}, t, \hat{\mathbf{s}})$ [W/m^{2}sr], which is the power per unit area and per unit solid angle along the direction $\hat{\mathbf{s}}$, inside a small volume V:

$$\frac{1}{v}\frac{\partial}{\partial t}L = -\hat{\mathbf{s}} \cdot \nabla L - L(\mu_s + \mu_a) + \mu_s \int_{4\pi} p(\hat{\mathbf{s}}, \hat{\mathbf{s}}')L d\Omega + Q \tag{1.15}$$

where v is the speed of light inside the medium. The variation in time of the radiance is given by the terms on the right-hand side of the equation, which are, in order of appearance:

1. energy crossing the volume boundaries;

2. energy loss due to scattering or absorption;

3. energy gain due to scattering from direction $\hat{\mathbf{s}}$ to direction $\hat{\mathbf{s}}'$. Inside the integral appears the scattering phase function, which is usually dependent only on $\hat{\mathbf{s}} \cdot \hat{\mathbf{s}}' = \cos\theta$.

4. energy gain due to sources $Q = Q(\mathbf{r}, t, \hat{\mathbf{s}})$ inside the volume.

1.3.1 Solving the radiative transfer equation

The RTE is a complicated equation, therefore numerical methods and analytical approximations are often used. Here we list the solution methods that have been considered throughout this work.

Sperical harmonics - P_n

In this method the radiance is expanded in a series of spherical harmonic functions. The degree of approximation is given by the number N of the considered terms, the so called P_n approximation. The solution has to be derived from a system of equations which may be solved numerically, resulting in a large computational cost. In the limit of $N \to \infty$ this method provides an exact solution of the RTE [21] [22].

Diffusion approximation

The diffusion approximation comes as a P_n solution for $N = 1$, together with some further approximations. This is the most popular solution method [13], since it provides analytical solutions whose degree of approximation is sufficient for many real situations. The diffusion theory will be covered in Section 1.4.

Monte Carlo

The Monte Carlo (MC) method explicitely exploits the random walk picture for transport introduced in Section 1.2.1 [23,24]. It involves a stochastic numerical simulation of the RTE by tracing fictional particles through the medium. The basic assumption is that the radiance is proportional to the spatial density of the traced particles. In the limit of an infinite number of particles traced, MC is an exact solution of the to the RTE. Additional insights on the MC approach will be introduced in Section 1.6.

1.4 Diffusion approximation

The diffusion approximation corresponds to a P_1 approximation of the radiative transfer equation in a homogeneous disordered media, therefore it supposes the existence of a finite scattering mean free path $l_s = 1/\mu_s$. The reduced scattering coefficient is defined as $\mu'_s = (1-g)\mu_s = 1/l_t$ as relative to the transport mean free path.

In order to derive the diffusion equation (DE) we adopt the derivation in [25,26]. For more insights on the topic the reader can also refer to [11,13]. We neglect absorption without loss of generality, since absorption can always be added at a later stage [25].

The P_1 approximation requires expanding the radiance in a series of spherical harmonics keeping the zeroth and first order terms, which correspond to the isotropic and first anisotropic terms of the series :

$$L(\mathbf{r}, t, \hat{\mathbf{s}}) \approx \frac{1}{4\pi}\Phi(\mathbf{r}, t) + \frac{3}{4\pi}\mathbf{F} \cdot \hat{\mathbf{s}} \tag{1.16}$$

where

$$\Phi(\mathbf{r}, t) = \int_{4\pi} L(\mathbf{r}, t, \hat{\mathbf{s}}) d\Omega \tag{1.17}$$

is the *fluence rate* [W/m^2] and

$$\mathbf{F}(\mathbf{r}, t) = \int_{4\pi} L(\mathbf{r}, t, \hat{\mathbf{s}})\hat{\mathbf{s}} d\Omega = F(\mathbf{r}, t)\hat{\mathbf{s}}_f \tag{1.18}$$

is the *diffuse flux* vector [W/m^2], pointing in the prevalent direction of energy flow $\hat{\mathbf{s}}_f$. A further assumption is that of a isotropic source

$$Q(\mathbf{r}, t, \hat{\mathbf{s}}) = \frac{1}{4\pi} Q_0(\mathbf{r}, t) \tag{1.19}$$

of dimensions [W/m^3]. Inserting eq. 1.16 and eq. 1.19 in the RTE (1.15) assuming $\mu_a = 0$, yields the two following coupled equations:

$$\frac{1}{v}\frac{\partial}{\partial t}\Phi(\mathbf{r}, t) + \nabla \mathbf{F}(\mathbf{r}, t) = Q_0(\mathbf{r}, t), \tag{1.20}$$

$$\left(\frac{1}{v}\frac{\partial}{\partial t} + \mu'_s\right)\mathbf{F}(\mathbf{r}, t) + \frac{1}{3}\nabla\Phi(\mathbf{r}, t) = 0. \tag{1.21}$$

one obtained by integrating over all $\hat{\mathbf{s}}$ and the other obtained by first multiplying by $\hat{\mathbf{s}}$ and then integrating over all $\hat{\mathbf{s}}$

In the hypothesis that the time variation of the diffused flux vector over one transport mean free path $l_t = 1/\mu'_s$ is negligible with respect to the vector itself:

$$\left|\frac{1}{v\mu'_s}\frac{\partial}{\partial t}\mathbf{F}(\mathbf{r}, t)\right| \ll |\mathbf{F}(\mathbf{r}, t)|, \tag{1.22}$$

eq. 1.21 reduces to the Fick's first law of diffusion

$$\mathbf{F}(\mathbf{r}, t) = -\frac{1}{v} D \nabla \Phi(\mathbf{r}, t) \tag{1.23}$$

where D is the diffusion constant

$$D = \frac{v}{3\mu_s'} = \frac{1}{3} v l_t \tag{1.24}$$

measured in [m^2/s]. Inserting the Fick's law in eq. 1.20 we obtain the diffusion equation (DE) for an homogeneous non-absorbing medium

$$\left(\frac{\partial}{\partial t} - D\nabla^2 \right) \Phi(\mathbf{r}, t) = v Q_0(\mathbf{r}, t). \tag{1.25}$$

The solution of the DE for an isotropic pulse-like source

$$Q_0(\mathbf{r}, t) = \delta(\mathbf{r} - \mathbf{r}')\delta(t) \tag{1.26}$$

in an unbounded homogeneous non-absorbing medium is

$$\Phi(\mathbf{r}, t) = \frac{v}{(4\pi D t)^{3/2}} \exp\left(\frac{-|\mathbf{r} - \mathbf{r}'|^2}{4Dt} \right). \tag{1.27}$$

1.4.1 The diffusion constant

An alternative derivation, explicitly based on random walk arguments, relates the diffusion constant D with the statistical first and second moments of the step-length distribution $p(l)$. This approach allows to derive a more general expression for D compared to that in eq. 1.24, which is instead obtained from the diffusion approximation of the radiative transfer equation. For further references see [27, 28]. We assume isotropic scattering, but the results can be applied to anisotropic scattering considering the step length l as the distance after which the direction of the walker is completely randomized.

Considering a random walker in 3 dimensions, its position $\mathbf{r}_n$ after n steps is given by

$$\mathbf{r}_n = \sum_{i=1}^{n} \mathbf{x}_i = \sum_{i=1}^{n} l_i \hat{\mathbf{x}}_i. \tag{1.28}$$

By letting the walker start from the origin, the average position (over many different trials) for $n \gg 1$ is

$$\langle \mathbf{r}_n \rangle = 0. \tag{1.29}$$

Therefore the mean square displacement (MSD) is

$$\langle \mathbf{r}_n^2 \rangle = \langle \sum_{i=1}^{n} \mathbf{x}_i \cdot \sum_{j=1}^{n} \mathbf{x}_j \rangle = \sum_{i=1}^{n} \langle \mathbf{x}_i^2 \rangle + \sum_{i=1}^{n} \sum_{j \neq i}^{n} \langle \mathbf{x}_i \cdot \mathbf{x}_j \rangle. \tag{1.30}$$

Since the scattering is isotropic, thus there is not orientational correlation between steps, the second term of eq. 1.30 vanishes and the variance becomes additive. Moreover, since all steps are statistically equivalent

$$\langle \mathbf{r}_n^2 \rangle = n \langle l^2 \rangle. \tag{1.31}$$

It is well known that the MSD of a diffusing particle in d dimensions grows in time as [8]

$$\langle \mathbf{r}^2(t) \rangle = 2dDt \tag{1.32}$$

and here we assume

$$\langle \mathbf{r}^2(t) \rangle = \langle \mathbf{r}_n^2 \rangle. \tag{1.33}$$

Considering the average time $\langle \Delta t \rangle$ to perform a step we have

$$t = n \langle \Delta t \rangle. \tag{1.34}$$

Moreover if each step is performed with velocity v we have

$$\langle \Delta t \rangle = \frac{\langle l \rangle}{v}. \tag{1.35}$$

Assembling together equations from 1.31 to 1.35 we obtain the expression

$$D = \frac{v}{2d} \frac{\langle l^2 \rangle}{\langle l \rangle}, \tag{1.36}$$

which gives the diffusion constant as the ratio of the first two moments of the step-length distribution characteristic of transport. We can retrieve the expression in eq. 1.24 by assuming an exponential step-length distribution as

$$p(l) = \frac{1}{l_t} \exp\left(-\frac{l}{l_t} \right). \tag{1.37}$$

Diffusion and Central-Limit Theorem

Consider a set of independent identically distributed (i.i.d.) random variables x_i distributed according to the function $p(x)$. The Central-Limit Theorem states that the random variable

$$x_n = \textstyle\sum_{i=1}^{n} x_i \qquad n \to \infty \tag{1.38}$$

is distributed according to a Gaussian function provided only that the second moment of $p(x)$ is finite [29]. When the random variable is the step length of a random walk in a transport process the displacement distribution tends to the one in eq. 1.27 after many steps. The Central-Limit Theorem is the root of the ubiquity of diffusion in nature, saying that diffusion is established each time the disorder of the system provides a ste-length distribution with a finite variance, which is the most common situation. The expression of the diffusion constant given in eq. 1.36 highlights the requirement of the Central-Limit Theorem, showing that the diffusion constant cannot not be correctly defined in the case of a step-length distribution with a diverging variance.

1.5 Diffusion on finite-size media

Here we seek for a solution of the diffusion equation (1.25) in a typical slab geometry, which is sketched in fig. 1.6. A slab is a 3D bulk medium infinite along the $\hat{x}$ and $\hat{y}$ axes, but finite along the $\hat{z}$ axis with thickness L. Study of transmission and reflection of light through a slab of a diffusive material is the object of many works [8]. This is a rather explored situation in the community of biomedical optics [5, 25], but other investigations regards light transport in strongly anisotropic scattering materials as liquid crystals [30, 31] and compressed powders [32]. Here we present some of the results obtained by Contini et al. [25] for the case of index-matched boundaries ($n_1 = n_0$), introducing an expression for the time-resolved and spatially-resolved transmission. This expression will be adopted as fitting function for some of the measurements presented along the thesis (see Chapter 3). For a treatment of the effects of the internal reflections at the boundaries due to an index-mismatched with the environment ($n_1 \neq n_0$) some classical papers to refer to are [33, 34].

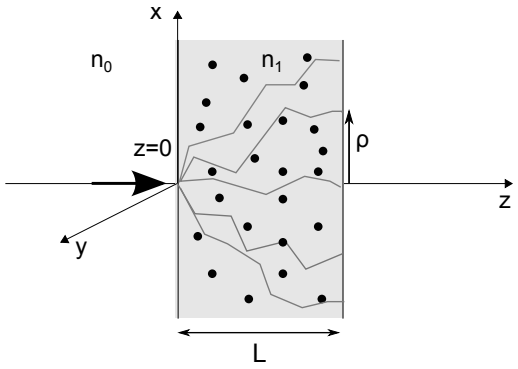

Figure 1.6 – Typical slab geometry and some notations. Gray lines sketch the propagation of light.

1.5.1 Boundary conditions

In many situations what defines the degree of approximation of the solution is the choice of the boundary conditions, which should describe as better as possible the real physical situation. The two most commonly used boundary conditions used to solve the diffusion equation are: the zero boundary condition and the extrapolated boundary condition. The zero boundary condition is the most simple and approximate, assuming the diffused fluence rate (eq. 1.17) equal to zero at the physical boundary. This can be a realistic approximation for very (optically) thick samples $L \gg l_t$, where thus the fluence at the boundary is much smaller than the fluence near the source. Assuming the source placed inside the medium and steady state condition, the energy distribution obtained with zero boundary condition

decreases linearly along the medium, see fig. 1.7(a). One more limitation of such approximation is the impossibility to take into account reflections at the boundaries for index-mismatched samples.

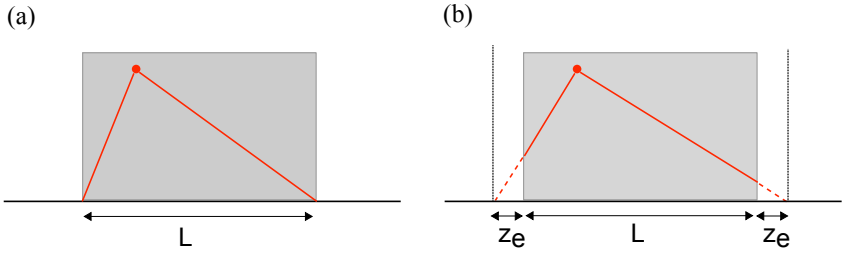

Figure 1.7 – Energy density distribution for a continuous source placed inside the slab for the two boundary conditions. (a) Zero boundary condition; (b) extrapolated boundary condition.

The extrapolated boundary condition assumes the fluence rate equal to zero at an extrapolated boundary outside the medium, see 1.7(b). This is a mathematical trick allowing to use the type of solution corresponding to zero boundary condition in a more realistic situation, where a fluence rate at the boundary exist. The extrapolated boundaries are both placed at a distance z_e, the *extrapolation length*, from the physical boundaries. By assuming a linear decay to zero of the fluence rate outside the medium, the extrapolation length results to be proportional to the transport mean free path l_t. In contrast to the zero boundary condition the extrapolated boundary condition allows to include the contribution to the fluence rate given by internal reflections, resulting in a dependence of z_e on the reflection coefficient characterizing the boundaries. A general expression of the extrapolation length including this dependence is [33]

$$z_e = \frac{2}{3}\frac{1+R}{1-R} l_t, \tag{1.39}$$

where $R = R(n_1/n_0)$ is the reflection coefficient [35] averaged over all incidence angles. Another expression which consider an higher order dependence on R is given in [36]. In both cases the extrapolation length for index matched boundaries ($R = 0$) is simplified to

$$z_e = \frac{2}{3} l_t \tag{1.40}$$

which is very close to the expression $z_e = 0.7104 l_t$ given by Milne solution. The Milne solution is indeed another frequently adopted expression for the extrapolation length [11].

1.5.2 Temporal and spatially resolved transmission

In a typical optical characterization experiment the light source is a laser beam shined on one of the surface of the sample, then the reflection or the

transmission is measured. Wether a collimated or a focused beam impinges on the sample, the propagation direction is randomized after a distance l_t, thus one of the model used to describe such source places an isotropic point source at a depth $z_0 = l_t$ inside the medium. Since we are considering a pulse source (see eq. 1.26), its analytical expression is

$$Q_0(\mathbf{r}, t) = \delta(x)\delta(y)\delta(z - z_0)\delta(t) \tag{1.41}$$

This model does not take into account the spatial extension of the real source created by the laser beam during the first scattering events. However, for optical thick media, the particular expression of the source does not significantly change the results. Alternative models for the source can be found for example in [25].

In order to solve the diffusion equation we assume the extrapolated boundary condition. However this condition cannot be achieved by placing only one isotropic point source inside the slab. A zero fluence at the boundaries can instead be obtained by placing, along the $\hat{z}$ axis of an infinite medium, an infinite series of equivalent sources positively and negatively charged [5, 25, 37]. In particular the sources are placed in

$$\begin{cases} z_{+,m} = 2m(L + 2z_e) + z_0 & \text{for positive sources} \\ z_{-,m} = 2m(L + 2z_e) - 2z_e - z_0 & \text{for negative sources} \end{cases} \tag{1.42}$$

with $m = (0, \pm 1, \pm 2, \cdots)$. The exact expression of the fluence rate $\Phi_+(\mathbf{r}, t)$ generated by the positive sources and of the fluence rate $\Phi_-(\mathbf{r}, t)$ generated from the negative sources can be derived. The total fluence rate is thus given by

$$\Phi(\mathbf{r}, t) = \Phi_+(\mathbf{r}, t) + \Phi_-(\mathbf{r}, t). \tag{1.43}$$

The slab configuration is inherently symmetric around the $\hat{z}$ direction, thus $\Phi(\mathbf{r}, t) = \Phi(\rho, t)$, where ρ is the radial distance from the $z = 0$ axis (see fig. 1.6). The time-resolved transmission is the diffuse flux at $z = L$, thus

$$T(\rho, t) = -\hat{q} \cdot \mathbf{F}(\rho, z = L, t) = -4\pi D \frac{\partial}{\partial z} \Phi(\rho, z = L, t), \tag{1.44}$$

where $\hat{q}$ is directed inward the medium. We report the explicit expression of the transmission for a non-absorbing medium

$$T(\rho, t) = \frac{\exp(-\frac{\rho^2}{4Dt})}{2(4\pi D)^{3/2} t^{5/2}} \sum_{m=-\infty}^{+\infty} \left[z_{1,m} \exp\left(-\frac{z_{1,m}^2}{4Dt} \right) - z_{2,m} \exp\left(-\frac{z_{2,m}^2}{4Dt} \right) \right], \tag{1.45}$$

where

$$\begin{cases} z_{1,m} = L(1 - 2m) - 4mz_e - z_0 \\ z_{2,m} = L(1 - 2m) - (4m - 2)z_e + z_0 \end{cases} \tag{1.46}$$

The number of necessary terms to keep in the series depends on the time-range and spatial-range to cover. This expression of the transmission gives

the probability distribution for a diffusive random walker (a "photon") to travel in a time interval t from one generic point on the surface of the medium to another generic point on the opposite surface. This is why the time-resolved transmission is also known as optical time-of-flight distribution (TOF).

The total transmission is obtained by integrating eq. 1.45 over the slab rear surface

$$\begin{aligned} T(t) &= \int_{+\infty}^{-\infty} T(\rho,t) 2\pi d\rho \\ &= \frac{1}{2(4\pi D)^{1/2} t^{3/2}} \sum_{m=-\infty}^{+\infty} \left[z_{1,m} \exp\left(-\frac{z_{1,m}^2}{4Dt}\right) - z_{2,m} \exp\left(-\frac{z_{2,m}^2}{4Dt}\right) \right]. \end{aligned} \tag{1.47}$$

1.5.3 Scaling laws

An alternative derivation of the total time-resolved transmission employs an eigenfunction expansion to solve the diffusion equation with a pulse source. Below we report an expression for the solution based on the one presented in [34]:

$$\begin{aligned} T(t) = &-\frac{2DI_0\pi}{(L+2z_e)^2} \times \\ &\sum_{n=1}^{\infty} n \sin\left(\frac{l_t+z_e}{L+2z_e} n\pi\right) \cos\left(\frac{L+z_e}{L+2z_e} n\pi\right) \exp\left(-\frac{\pi^2 n^2 Dt}{(L+2z_e)^2}\right) \end{aligned} \tag{1.48}$$

where I_0 is the intensity of the pulse source placed at a depth l_t inside the slab. The solution is obtained assuming the extrapolated boundary condition. A detailed derivation of the expression can be found in [38]. In most of the situations this expression is equivalent to the one in eq. 1.47 and the two can be derived from each other applying Poisson summation rules. For a discussion on the equivalence of the two solution see [39].

The expression in eq. 1.48 is more suitable for an analysis of the asymptotic behavior (long time) of the transmission. Indeed at long time the behavior of the summation in eq. 1.48 is determined by the lowest eigenvalue ($n = 1$) and the decay will eventually becomes a single exponential $\propto \exp(t/\tau)$ with decay constant

$$\tau = \frac{(L+2z_e)^2}{\pi^2 D}. \tag{1.49}$$

The typical time dependence of the diffusive transmission is show in fig. 1.8. The quadric scaling of $\tau(L+2z_e)$ is one of the fingerprint of diffusion dynamics, which can be observed by measuring τ for different sample thickness. In the limit $L \gg l_t$ the contribution of z_e is negligible and the scaling can be approximated as $\tau \propto L^2$.

However the role played by the extrapolation length becomes crucial when L is few times z_e. Is such condition it is essential a good estimation of the extrapolation length to observe the diffusive scaling. For example in strongly scattering medium it is not obvious the definition of an effective refractive index, which allows to include the contribution of internal reflections for the estimation of z_e using eq. 1.39. For a discussion on the importance of z_e in this scaling law see [40].

Evaluating the integral on time of eq. 1.48 we obtain the total transmission in steady state [41]. It emerges another important scaling law of diffusion

$$T = I_0 \left(\frac{l_t + z_e}{L + 2z_e} \right). \tag{1.50}$$

which is not directly related to the dynamic of transport, since it does not give a complete information on the diffusion constant. Also in this case the contribution of z_e vanishes in the asymptotic limit $L \gg l_t$ and eq. 1.50 takes the form of a Ohm's law for light $T \propto L^{-1}$.

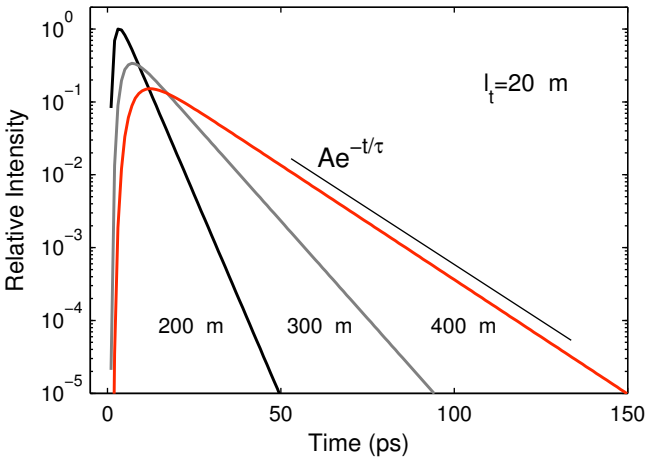

Figure 1.8 – Total time-resolved transmission out of a slab of diffusive medium with $l_t = 20\mu$m, calculated with eq. 1.48. The y-axis is in log scale. For long times the transmission becomes a single exponential of decay constant τ. The decay constant grows quadratically with the corrected thickness $L + 2z_e$.

1.6 Monte Carlo basics

The Monte Carlo (MC) method is a numerical technique used to solve many physical or mathematical problems based on stochastic processes. MC relies on the ability of computers to generate, with a certain approximation, a sequence of random numbers. Once the stochastic process has been modeled through a suitable set of equations each generated sequence of random

number determines a possible solution for the system. Iterating *ad infinitum* the process we obtain a frequency distribution of possible solutions representing a probability distribution for the result of the numerical experiment. Thanks to the increasing computer performance MC is becoming more and more powerful. Parallel computing is a precious help in reducing the simulation time. An impressive step forward have been the implementation of MC simulations on GPU hardware [42], which are able to speedup a typical simulation of light transport through turbid media of three order of magnitude. GPU-accelerated MC simulations have been used in Chapter 6. For an introduction to Monte Carlo simulations see [23] [43].

As we have mentioned in Section 1.3 applying MC to light transport corresponds to solve the radiative transfer equation, obtaining an exact solution for long enough simulations. MC does not consider all the approximation of diffusion theory, but requires only the energy conservation. Moreover it allows to handle any sample geometry.

Here we introduce and discuss the main physical concepts behind a Monte Carlo simulation of light transport in a non-absorbing finite-size disordered medium. The basic idea is to simulate a random walk of particles in a slab, launching millions of walkers in the medium, and count how many of the them are transmitted, where they exit the sample surface and how much time did they take to cross the sample. If necessary the random path performed by each walker can also be traced for each instant of time. Averaging over the paths of all the launched walkers we obtain the evolution in time of the particle density. The connection to radiative transfer is that the particle density $N(\mathbf{r}, t, \hat{\mathbf{s}})$ [$1/\mathrm{m}^3\mathrm{sr}$] in the direction $\hat{\mathbf{s}}$ is proportional to the radiance as

$$N(\mathbf{r}, t, \hat{\mathbf{s}}) = \frac{L(\mathbf{r}, t, \hat{\mathbf{s}})}{Ev} \tag{1.51}$$

where E is the carried energy per particles and v the propagation velocity. Usually it is assumed $v = c_0/n$, where n is the refractive index of the medium hosting the scatterers.

Here we consider a so called annealed disorder, where the frozen position of scatterers is neglected and at each step the particle sees a new statistically equivalent system. The transport properties of the medium are included in the simulation by defining the step-length distribution $p_l(l)$ and the scattering phase function $p_\theta(\cos\theta)$. Below we list and comment the main passages of a standard MC simulation.

Initialize the particle

The particle is launched in accordance to the kind of source we want to simulate. For a collimated source particles are injected in the slab volume (whose front surface can be placed at the origin) with a single direction. For a focused source the injection angles θ_i are uniformly distributed in the range $[-\theta_{NA}, \theta_{NA}]$, where $\theta_{NA} = \sin^{-1}(NA/n_0)$, with NA the numerical aperture of the focusing lens and n_0 the refractive index of the medium in which the

lens is embedded. In order to better simulate a pulse source the starting time t_0 can be chosen among a gaussian distribution of time centered in $t = 0$, whose width sets the temporal width of the pulse.

Move the particle

The particle will now take a step direction selected in the previous step. The length of the step depends on the step-length distribution $p_l(l)$. It means that we have to extract a random number l according to the probability density function $p_l(l)$. Commercial mathematical softwares(like *Matlab*) provides implemented random number generator for different distribution functions. In any case various techniques to obtain the desired distribution of random number from a uniform random number generator have been developed [23, 42, 43]. A simulation of transport in homogeneous disorder requires $p_l(l) = (1/l_s)e^{-l/ls}$.

Change direction

If the particle has not crossed one of the sample boundaries during the step, it will change direction once the step is terminated. The single scattering phase function, gives the angular probability distribution to scatter in the direction (θ, ϕ). Usually the azimuthal angle ϕ can be chosen uniformly in $\phi \in (0, 2\pi]$ and the phase function decides the probability $p_\theta(\cos\theta)$ to pick-up a $\cos\theta$ value between $[-1, 1]$. For isotropic scattering $\cos\theta$ is uniformly distributed in the interval. To better understand why the random value to generate is $\cos\theta$ and not directly θ the reader can refer to [44].

Boundary conditions

After each step it is necessary to check if the particle has crossed the sample boundaries. For a slab configuration of finite thickness L along $\hat{\mathbf{z}}$, the particle can travel undisturbed along the other two directions until one of the two conditions $z < 0$ (back-scattered) or $z > L$ (transmitted) is satisfied. All the simulation presented in the work are performed for index-matched slabs, thus when the walker is at the boundary it always exit the sample. For index matched samples the probability either to be transmitted or to be reflected inside the medium are given by the Fresnel reflection coefficient $R(\theta)$ [35], averaged over different polarization directions.

Time-resolved transmission

In order to obtain the time-resolved transmission $T(\rho, t)$ it is necessary to store for each walker the exit-time and the position (x, y) on the rear surface of the slab. If we are interested in the total time-resolved transmission the position (x, y) can be neglected.

CHAPTER 2

Transport in complex scale-invariant media and superdiffusion

The Central-Limit Theorem forces all transport processes with finite variance and uncorrelated steps to a diffusive propagation. One of the fingerprint of diffusion is the linear growing of the mean square displacement [8]

$$\langle x^2(t)\rangle = 2dDt \tag{2.1}$$

where d is the space dimension and D [m^2/s] is the diffusion constant.

When the nature of disorder deviates from being homogeneous but assumes a *fractal* geometry transport can be deeply modified. Fractal substrates are the extreme side of heterogeneity, which is not fixed to a typical length scale but is spread on many order on magnitude in a self-similar way.

Several systems have revealed a fractal geometry in their complex heterogeneity. Fractals are clouds [45] [46], snowflakes [47], nanoparticles and colloids aggregates [48, 49], polymers [50], porous media and fractures in rock [51, 52]. Recently it is emerged that important networks like DNA aggregates, living cells [53], ecosystems [54] and also the huge web of Internet [55, 56] are fractals.

A random walker on a fractal does not explore the space uniformly but can be forced to oversample some regions or to enhance the efficiency of exploration. Eventually transport on fractals is *anomalous* [47] [57], in the sense that the laws of diffusion have to be generalized. For example the mean square displacement can grow either sublinear or superlinear, so that eq. 2.1 has to be generalized as

$$\langle x^2(t)\rangle \propto D_\gamma t^\gamma \tag{2.2}$$

When $\gamma < 1$ there is *subdiffusion* while when $\gamma > 1$ there is *superdiffusion*. D_γ [m^2/s^γ] is a generalized diffusion constant.

Here we are interested in fractal-like structures which can generate superdiffusion. A random walk on such a substrate is known as a Lévy flight or also a Lévy walk. They are characterized by a power-law step-length distribution and thus by a diverging variance. As a consequence the Central-Limit theorem non longer holds and the transport can go beyond diffusion. A crucial aspect is that Lévy flights present a finite probability to perform very long jumps which critically enhanced the transport regime.

In this chapter we introduce the two main theoretical frameworks in which superdiffusion is modeled. One is the scaling theory and the other is the continuos-time-random walk (CTRW). We focus on the scaling properties of the superdiffusive propagator and on the scaling of measurable dynamic quantities which follows from this.

2.1 Basics on fractals

When observing an object we can often recognize a geometrical pattern of the structure. If the scale of observation is much larger than the length scale of the elementary components the fine structure we perceive is set by the magnification of the image. More likely increasing the magnification we will reveal different geometrical details since the structure of the elementary components begins to appear. Some structures are instead "assembled" so that sequentially increasing the magnification we always observe the same geometrical pattern. This is a scale-invariance property known as *self-similarity* and is one of the main features of fractals. The fractal self-smilarity usually leads to non-euclidean scaling laws characterized by non-integer scaling exponents [58] [47].

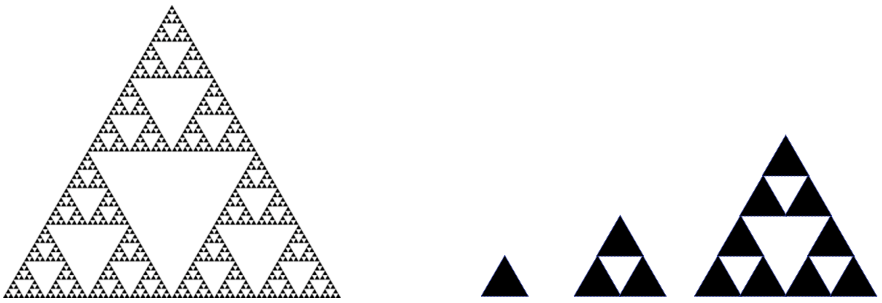

Figure 2.1 – Sierpinsky gasket in 2D. (a) The gasket is obtained dividing an equilateral triangle into four smaller triangles and taking out the central one. The generation procedure is iterated *ad infinitum*. The gasket shown is at its sixth generation. (b) Alternative generation of the gasket starting from a triangular genus.

A class of fractals is that of deterministic fractals, which are mathemat-

ical objects with a non-integer Hausdorff-Besicovitch dimension, also called fractal dimension d_f [58]. They are constructed with a rigorous deterministic recursive law. An example is the 2D Sierpinski gasket in fig. 2.1(a). It starts from an equilateral triangle, which subdivided into four smaller triangles taking out the central triangle. The procedure is called the generator and is iterated *ad infinitum*. The Sierpinski gasket can also be assembled in the other way around, starting from a triangular genus and building the gasket as shown in fig. 2.1 (b). The object obtained after one iteration (magnification $\times 2$) encloses exactly 3 of the original element. The *fractal dimension* is defined as $2^{d_f} = 3$, thus $d_f = \ln 3 / \ln 2 = 1.585$. Other celebrated deterministic fractals are the Koch curve and the Sierpinsky sponge. [47].

Many other objects have the self-similarity property of fractals, but only in a statistical sense. It means that changing the scale of observation is the distribution of geometrical features to be invariant. Such objects belongs to the family of statistical fractals, whose fractal dimension d_f is defined by looking at the scaling of their mass M with their linear size L [59]:

$$M \propto L^{d_f} \tag{2.3}$$

Fractals have non-integer value of d_f while euclidean objects have $d_f = 1, 2, 3, \ldots$. Mandelbrot was the first to realize that many objects in nature have such a fractal-like shape [58]. He formulated the famous question on: how long is the coast of Britain? Indeed the coast of Britain, as other coast in the world, recursively show the same inlets distribution increasing the magnification of observation. It follows that as you decrease the length scale of the "rule" used to measure the coast you obtain a larger measured length. The paradox has become the paradigm of the fractal geometry. Certainly the paradox of Mandelbrot have a solution in the case of real fractals, since they are limited by a lower and upper cut-off in their fractality [60]. Indeed the description of transport processes using fractal models is applicable at certain length scales and conditions.

2.1.1 Random walks as fractals

Also random walks are fractal object in a statistical sense. To better understand this concept let us consider the simple 2D random walk illustrated in fig. 2.2 (a), which has a unitary step length. The random walk looks statistically self-similar when one regards n consecutive steps as one single superstep r [47] . Each superstep r is a random displacement of the original walker and the Central-Limit Theorem implies that such displacement is gaussian distributed for large n. It follows that the distribution $P_n(r)$ of supersteps lengths is a Gaussian. This holds for any n provided that n is large enough. Since different values of n correspond to different scale of observations the step-length distribution is scale-invariant. This is what generates the self-similarity of a random walk, which is evident in fig. 2.2 (b). At different scale of observation (different values of n) the geometrical pattern outlined by the walkers looks similar.

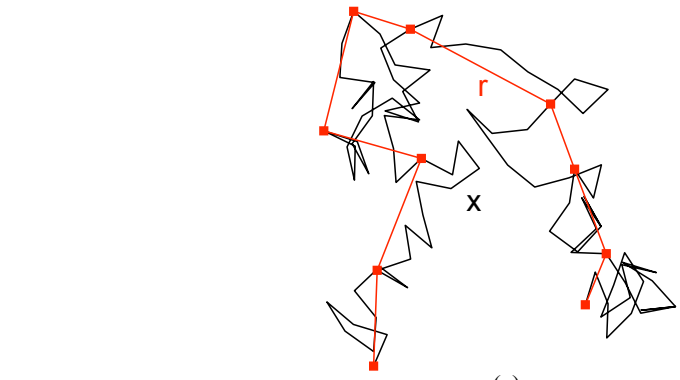

(a)

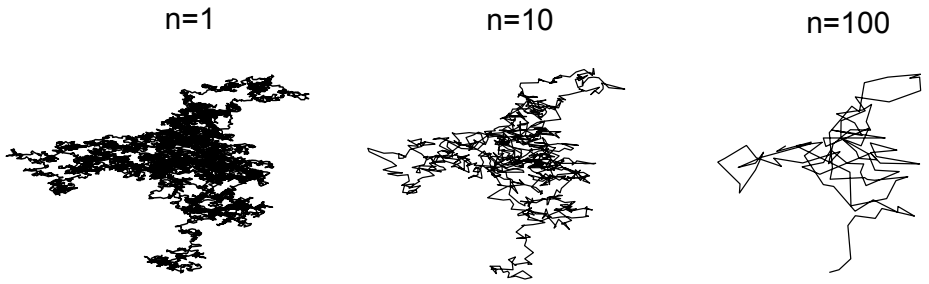

(b)

Figure 2.2 – Self-similarity of a standard random walk with 10000 unitary steps. (a) Definition of the superstep r as the effective random displacement after n small steps. (b) The geometrical pattern outlined by the walker is similar for different values of n, that is for different scale of observation.

Since random walks are fractals they can be also characterized by a fractal dimension in analogy to the definition of eq. 2.3. If the number of visited sites $N(R)$ in the hypersphere of radius R grows as

$$N(R) \propto R^{d_w}, \tag{2.4}$$

the exponent d_w is the fractal dimension of the random walk, or simply the *walk dimension*. Random walks in euclidean space have $d_w = 2$ for any space dimension $d \geq 2$. This is the typical walk dimension of diffusive process like the Brownian motion.

Interestingly if we force the walker to propagate on a disordered but statistically self-similar structures we would still observe a self-similar random walk. Such random walks have fractal dimensions no longer equal to 2 and the diffusion becomes *anomalous*.

2.1.2 Scaling of dynamics on fractals

All the properties of the transport are contained in the propagator $P(\mathbf{r}, t|\mathbf{r}')$, which gives the probability for the walker to be in $\mathbf{r}$ at time t starting from $\mathbf{r}'$, where $\mathbf{r}$ and $\mathbf{r}'$ are points on the fractals [8, 11, 47, 61]. The physical meaning of the propagator depends on the specific transport we deal with. For instance in studies of particles diffusion the propagator is proportional to the density of particles in space. When dealing instead with light transport in disordered media the propagator is proportional to the energy density distribution. Averaging $P(\mathbf{r}, t|\mathbf{r}')$ over the starting position we obtain a translational-invariant quantity

$$P(r, t) = \langle P(\mathbf{r}, t|\mathbf{r}')\rangle. \tag{2.5}$$

depending on $r = |\mathbf{r} - \mathbf{r}'|$.

We have said that random walks on self-similar substrate are self-similar themselves, but what is the effect on the dynamics of transport? The so called scaling hypothesis [47,62–65] assumes that self-similarity dynamically implies the existence of a single time-dependent characteristic length

$$\xi(t) \propto t^{1/d_w} \tag{2.6}$$

capable to continuously rescale the shape of the propagator making it time-independent, where d_w is the random walk dimension.

Because of the dilatation symmetry we expect $P(r, t)$ to be an homogeneous function of its argument. It thus follows the standard scaling of the propagator

$$P(r, t) \propto \xi(t)^{d_f} \widetilde{P}\left(\frac{r}{\xi(t)}\right) \tag{2.7}$$

The exponent d_f is the fractal dimension of the substrate, whose necessity can be derived by imposing the conservation of probability on the fractal substrate [50].

For standard diffusion $d_w = 2$ and the characteristic length is the square root of the mean square displacement $\xi^2(t) = \langle r^2\rangle$. In diffusion processes the propagator is gaussian and its width scales with the square root of time. This is exactly the results we derived in eq. 1.27 solving the diffusion equation.

Anomalous transport regimes are defined by walk dimensions different from 2 and from the consequent anomalous scaling of the propagator. A transport with $d_w > 2$ is called *subdiffusion* since it has a scaling slower than diffusion. Similarly a transport with $d_w < 2$ is named superdiffusion since it has a faster scaling respect to that of diffusion.

2.2 Lévy flights and Lévy walks

Lévy flights are random walks whose step-length distribution $p(x)$ decays as a power-law

$$p(x) \simeq |x|^{-(\alpha+1)} \quad \text{with} \quad 0 < \alpha < 2 \tag{2.8}$$

This slow asymptotic decay is often termed as "heavy tail". By definition they are Markovian stochastic processes, thus with independent steps. The variance of a Lévy flight diverges $\langle x^2 \rangle \to \infty$ since long jumps may occur on all length scales. The Central-Limit Theorem no longer holds and a generalization of it has to be considered. It mainly states that the sum of stochastic variables with diverging variance have as basin of attraction in the family of α-stable distributions [66]. For a Lévy flight the attractor distribution decays with the same power-law tail of the single step distribution in eq. 2.8. Applying the same reasoning as in Section 2.1.1 it follows that Lévy flights are self-similar. In contrast to a standard random walk a Lévy flight create a true statistical fractal with a non integer walk dimension, being $d_w = \alpha$. Figure 2.3 highlights such difference in the self-similarity, which for Lévy flight is characterized by cluster of shorter steps interconnected by long excursion.

Lévy flights are more common in nature than what we might intuitively suppose [57]. Interesting observations regard animal foraging patterns and diseases spreading [67] [68]. Extensive tracking of one dollar bills reveals Lévy statistics [69]. It has also been revealed that Lévy statistics governs the distribution of trades in economical contexts [70].

However transport based on Lévy flights can be unphysical. Indeed each step is performed in a constant time, but since arbitrary lengths are possible for the steps arbitrary velocity are required. Moreover the mean-square displacement of a Lévy flight can diverge in a finite time interval, thus during the observation.

A more realistic model is represented by Lévy walks, in which the walker pays a time cost to perform a step, so that for finite-time observations the mean square displacement is also finite. In the so called *velocity model* [71], the walker travels at a constant velocity v and thus the time t needed for a step is proportional to the step length x. Lévy walks are suitable to investigate the dynamic of superdiffusion, keeping the main properties of Lévy flights.

Thanks to their diverging variance Lévy flights and Lévy walks allow to go beyond diffusion, overcoming the constraint imposed by the Central Limit Theorem. Transport based on Lévy flights and Lévy walk is superdiffusive and in the next sections we will see what are the features of superdiffusion in the framework of the continuos-time random walk approach. We focus on the superdiffusion generated by a Lévy walk.

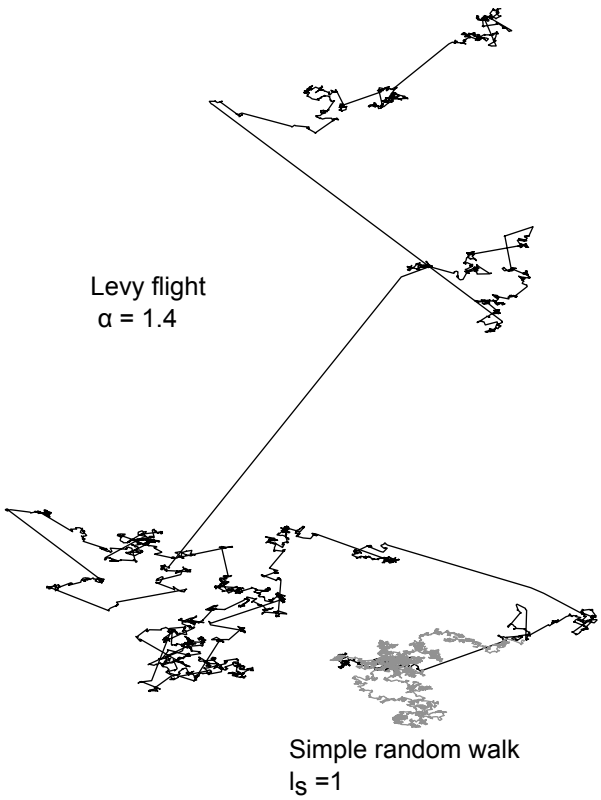

Figure 2.3 – Typical trajectory of a Lévy flight (in black) compared to a diffusive random walk with exponentially distributed steps around l_s (in gray). Both random walks have performed 5000 steps. Lévy flights explores space in a more efficient way thanks to the very long jump which may occur. Both random walks are self-similar but the Lévy flight has a non-integer walk dimension, beeing $d_w = \alpha$.

2.2.1 α-stable distributions

Here we give some insights on the stability property of distributions with a diverging variance, following the tutorial of Davis et al. in [46]. In probability theory "stability" describes random-variables that are invariant under addition. The invariance is intended as equal in distribution. Independent identically distributed random variables x_i $(i = 1, ..., n)$, symmetrically distributed and thus with zero mean, are stable if

$$\sum_{i=1}^{n} x_i \stackrel{d}{=} a_n x_1 \tag{2.9}$$

where $\stackrel{d}{=}$ means equal in distribution. In the 1937 Paul Lévy showed [72] that the only solutions to this problem have

$$a_n = n^{1/\alpha} \tag{2.10}$$

where $\alpha \in (0, 2]$ and a characteristic function for all x having the form

$$p(k) = \langle \exp(ikx) \rangle = \int \exp(ikx) p(x) dx = \exp(-\sigma |x|^{\alpha}) \tag{2.11}$$

where $\sigma \geq 0$ is a natural scale parameter. (Angular brackets designate ensemble- or sample-average).

The characteristic function is the Fourier transform of the probability distribution $P(s)$, which solves the stability problem of eq. 2.9. Such solutions are know as α-stable distributions or also Lévy-stable distributions.

There are only two cases of α-stable distributions with a closed form expression. The first is the well-known Gaussian distribution, which has $\alpha = 2$ and variance $2\sigma^2$

$$p_2(x) = \frac{1}{2\sigma\pi^2} \exp\left[-\left(\frac{x}{2\sigma} \right)^2 \right] \tag{2.12}$$

The other is the Cauchy distribution, which has $\alpha = 1$

$$p_1(x) = \frac{1}{\pi\sigma[1 + \left(\frac{x}{\sigma}\right)]} \tag{2.13}$$

A crucial feature of α-stable distributions is the behavior of q-order moments

$$\langle x^q \rangle = \int x^q p_{\alpha}(x) dx \tag{2.14}$$

which for all real values of q are finite only when

$$\langle x^q \rangle < \infty \quad \text{for} \quad q < \alpha \tag{2.15}$$

thus $\langle x^2 \rangle = \infty$ when $\alpha < 2$.
Although the analytical closed expression is not always available, the tail of α-stable distributions for $0 < \alpha < 2$ has a precise power-law decay

$$p_{\alpha}(x) \sim x^{-(\alpha+1)} \tag{2.16}$$

from which can also be derived the asymptotic behavior of the cumulative distribution

$$p_{\alpha}(x > S) = \int_S^{\infty} p_{\alpha}(x) dx \sim S^{-\alpha} \tag{2.17}$$

Regarding the properties of transport based on α-stable distributions some important features needs to be kept in mind: they have a diverging variance when $\alpha < 2$ and even the mean (absolute) value diverges when $\alpha < 1$; they are stable, thus the attractor of the sum-distribution of α-stable distributions is still an α-stable distribution. This stability is a generalization of the Central-Limit Theorem.

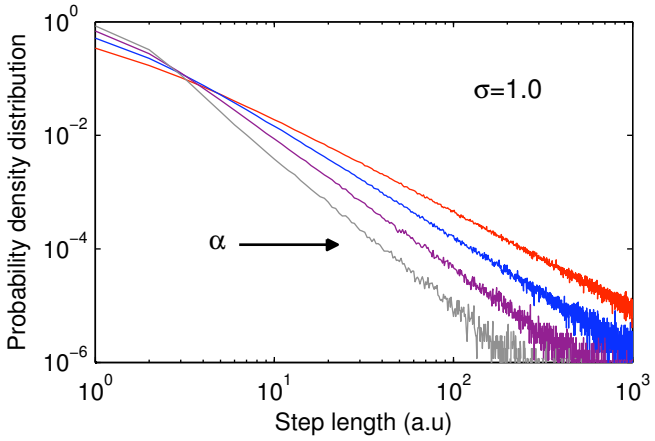

(a)

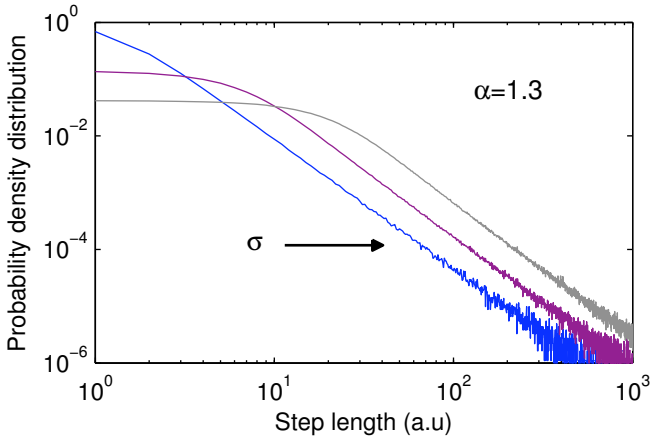

(b)

Figure 2.4 – α-stable distributions obtained by employing a dedicated random number generation algorithm. (a) Log-log plot of distributions with alpha=0.7, 1, 1.3, 1.6 and $\sigma = 1$. The arrow indicates the growing direction of α. (b) Log-log plot of distributions with $\alpha = 1.3$ and $\sigma = 1, 5, 15$. The arrow indicates the growing direction of σ.

Random number generation

Different algorithms are available to generate random numbers distributed according to an α-stable distribution. Some references are [73] [46]. These algorithms generate symmetric distributions for any value of α when $\sigma = 1$. In order to vary the scale parameter σ the number generated by the algorithm have to be multiplied for the desired value of σ. This operation changes the scale parameter of the whole distribution.

In fig. 2.4 we show α-stable distributions generated with the described method. To better highlight the power-law decay of the tail log-log axes

scale is used. We also show the effect of an increasing scale parameter σ. The generation of random number distributed according to α-stable function provides the step-length distribution for Monte Carlo simulations of Lévy flights and Levy walks.

2.2.2 The continuos-time random walk approach

Lévy walks have their framework in the continuos-time random walk (CTRW) approach [28, 71, 74, 75]. In the CTRW the random walk is entirely specified by $\psi(x,t)$, the probability density to move by a distance r in the time t in a single motion event. One possibility is to decouple the probability in a waiting-time distribution and a step-length distribution

$$\psi(x,t) = \psi(t)p(x) \tag{2.18}$$

This scheme usually corresponds to the *jump model* (see fig. 2.5), in which the walker waits until it instantaneously moves to a new site. The probability $\psi(t)$ determines the transport dynamics, which is subdiffusive when the second moment of $\psi(t)$ diverges [75]. The only requirement on $p(x)$ is that its second moment is finite.

In order to derive superdiffusion it is instead necessary to introduce coupled memories. In the *velocity model* (see fig. 2.5) the walker propagates at constant velocity so that the time to perform a step is proportional to the step length. The coupling between the waiting-time and the step-length distribution is thus given by

$$\psi(x,t) = \delta(|x| - vt)p(x) \tag{2.19}$$

where the δ function accounts for the time necessary to perform a step. The velocity can be fixed to $v = 1$ without loss of generality.

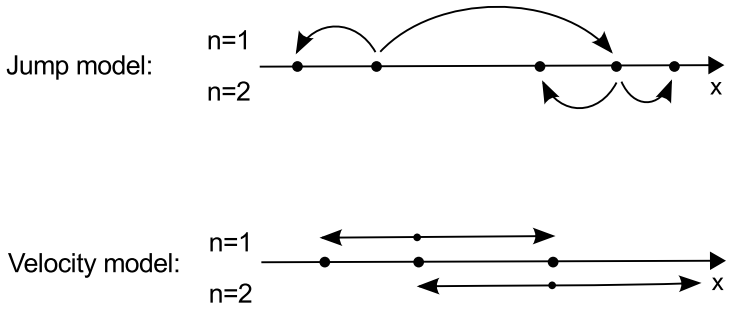

Figure 2.5 – Schematic representation of the jump and of the velocity model. Modified from [71]. $n = 1$ and $n = 2$ denotes two consecutive motion events. In the jump model the walker waits until in moves instantaneously to a new a site. In the velocity model the walker moves at constant velocity to a new site where it choses a new direction at random.

We are interested in the propagator $P(x,t)$ for the velocity model. We now derive a recursive expression for $P(x,t)$ by means of a set of equations

of evolution, following the work in [71] [76]. Since this is a 1D model at each scattering point the walker can only go either forth or back with equal probability, hence they define a set of turning points.
The first important quantity to calculate is the turning point distribution $Q(x,t)$, which is the solution of the following integral equation

$$Q(x,t) = \int_0^L \int_0^t Q(x',t')\psi(x-x',t-t')dx'dt' + \delta(x)\delta(t) \tag{2.20}$$

where L is the size of the interval and t the time of observation. The integral links the current turning point distribution to the previous turning point distribution through the step-length distribution. The $\delta-$function place the source in $x = 0$ at $t = 0$.
Another important quantity is the probability that the walker is located at time t in x while traveling between two turning points, which is given by

$$\Phi(x,t) = \delta(|x| - t) \int_{|x|}^{\infty} P(x')dx' \tag{2.21}$$

We now have all the ingredients to calculate the propagator $P(x,t)$, which gives the probability to find the walker in x at time t

$$P(x,t) = \int_0^L \int_0^t Q(x',t')\Phi(x-x',t-t')dx'dt' \tag{2.22}$$

Equation 2.22 expresses the fact that the particle is either at a turning point ($t = t'$) or it is moving between turning points with probability $\Phi(x,t)$.

On a unbounded interval eq. 2.22 can be simplify by moving to the Fourier ($x \to k$) and to the Laplace ($t \to s$) space since the integration interval L can be pushed to $[-\infty, +\infty]$, similarly the time integration interval to $[0, +\infty]$. In the new domains the propagator have the explicit expression

$$P(k,s) = \frac{\Phi(k,s)}{1-\psi(k,s)}, \tag{2.23}$$

where the use of k and s indicate the Fourier and/or Laplace transformed functions. Such expression allows also to calculate the mean square displacement in the Laplace space by

$$\langle x^2(s) \rangle = -\nabla_k^2 P(k,s)|_{k=0} \tag{2.24}$$

Equations 2.23 and 2.24 are of particular importance since they bring to asymptotic expressions for both the propagator and the mean square displacement in real space. In the next section we will see how superdiffusion emerges applying the derived evolution equations to a Lévy walk.

2.2.3 Superdiffusion

Here we focus on the scaling of the propagator and on the time dependence of the mean square displacement obtained for a Lévy walk. They can be derived by inserting in eq. 2.19 the power-law step-length distribution of eq. 2.8 and by applying eq. 2.23 and eq. 2.24. The asymptotic long-time behavior of the propagator is then calculated in the real space and time domain. The following scaling emerges

$$P(x,t) = \frac{1}{\xi} f\left(\frac{|x|}{\xi}\right) \tag{2.25}$$

with

$$\begin{aligned} &\xi = t && 0 < \alpha < 1 \\ &\xi = t^{1/\alpha} && 1 < \alpha < 2 \\ &\xi = t^{1/2} && \alpha > 2. \end{aligned} \tag{2.26}$$

Three characteristic scaling regimes can be distinguished depending on the considered values of α: the ballistic regime for $0 < \alpha < 1$, the intermediate regime for $1 < \alpha < 2$ and the regular diffusion for $\alpha > 2$.

This behavior is a very interesting since it shows that the CTRW approach gives results consistent with those of scaling theory on fractals discussed in Section 2.1.2. Moreover the CTRW allows to find asymptotic analytical expressions for the function $f(|x|/\xi)$, which can be found in [71] [63]. Using the expressions of the propagator the mean square displacement can be calculated obtaining

$$\langle x^2(t) \rangle \propto \begin{cases} t^2 & 0 < \alpha < 1 \\ t^2/\ln t & \alpha = 1 \\ t^{3-\alpha} & 1 < \alpha < 2 \\ t \ln t & \alpha = 2 \\ t & \alpha > 2 \end{cases} \tag{2.27}$$

The superlinear growing of the mean square displacement for $\alpha < 2$ is one of the fingerprint of superdiffusion. Indeed the few experimental observations of superdiffusive dynamics refer to the mean square displacement of particles. A classic experiment is that carried out by Solomon [77] who reported anomalous diffusion of particles in a turbulent flow. An interesting experimental observation is in [78], and a very recent one in [79]. Indeed the mean square displacement is a suitable observable to be studied in large systems through particle tracking. However, when dealing with light transport in finite-size disordered media the mean square displacement can be inadequate to be observe. Luckily superdifussion is not described only in terms of mean square displacement. Superdiffusion is a dynamic regime characterized by an anomalous scaling of the propagator, and we will see in the next section that this determines an anomalous scaling of other observables, which are perfect to be measured in optical characterization experiments.

2.3 Superdiffusion on finite-size systems

Following the results in [76] we introduce and discuss some important properties of a Lévy walk in a interval $[0, L]$ with absorbing boundaries. The condition of absorbing boundaries implies a situation where the walker disappears when hitting one of the boundaries, hence it cannot come back anymore. We will use Lévy walks for modelling light transport in a finite-size media. The absorbing boundary conditions well represent the situation where light exits the sample at the boundaries. Such boundary conditions becomes even more suitable when real samples are index matched with their environment, since such condition prevent internal reflections. The results will derived are valid in the asymptotic limit, that is for large enough interval so that any effect on transport introduced by the presence of boundaries can be neglected.

We have seen that in unbounded intervals all the equations of evolution can be transformed by using the Laplace and Fourier operators, and that such operation simplifies the convolutions of the equations of evolutions in linear relations. However on a finite-size interval we have a limit on the spatial integral and the Fourier operator cannot be applied. We can only Laplace transform the dependence on time since t can be pushed to infinity.

On a finite interval the equations of evolution in the Laplace domain are

$$Q(x,s) = \int_0^L Q(x',s)\psi(x-x',s)dx + \delta(x-x_0) \tag{2.28}$$

$$P(x,s) = \int_0^L Q(x',s)\Phi(x-x',s)dx' \tag{2.29}$$

with

$$\psi(x,s) = p(x)e^{-s|x|} \tag{2.30}$$

and

$$\Phi(x,s) = e^{-s|x|}\int_{|x|}^{\infty} p(x')dx' \tag{2.31}$$

2.3.1 Eigenfunctions expansion

Equation 2.28 is a Fredholm equation of the second kind with a symmetric kernel. The solution $Q(x,s)$ can be expressed in terms of the eigenfunctions $q_i(x,s)$ and eigenvalues $1/\lambda_i$ [80] of the equation

$$q(x,s) = \lambda\int_0^L \psi(x-x',s)q(x',s)dx' \tag{2.32}$$

When s is real the solution is

$$Q(x,s) = \sum_{i=1}^{\infty}\frac{q_i(x,s)}{\lambda_i(s)-1}\int_0^L q_i(x',s)\delta(x'-x_0)dx' \tag{2.33}$$

In analogy with the diffusion case the eigenfunctions expansion leads to a time dependence which for long times is dominated by a single exponential decay. Indeed inverting the Laplace transform, at long times one obtains

$$Q(x,t) \propto e^{|s_1|t} \tag{2.34}$$

where s_1 is the decay constant of the first eigenfunction. It can be shown that the time dependence of the turning point distribution is directly reflected on the propagator, so that as $t \to \infty$ we have

$$P(x,t) \propto e^{|s_1|t} \tag{2.35}$$

The dependence in eq. 2.35 is rather important since it represents a first step to link the features of the propagator of a Lévy walk to measurable observables in real finite-size systems. Placing the source at $x_0 = 0$ the quantity $P(L,t)$ is the time-resolved transmission probability $T(L,t)$ through the interval $[0, L]$ for a Lévy walk, which thus is expected to decay at long time as a single exponential.

2.3.2 Scaling laws

The scaling of the propagator of eq. 2.25 and eq. 2.26 derived on an unbounded interval also holds on a semi-infinite interval apart from the behavior at the boundary and for that of peculiar quasi-ballistic peak [76].

For a finite-size interval the scaling of the propagator determines the time dependence and the scaling with L of all the observables. A peculiar feature of superdiffusive dynamics can indeed be found in the scaling with the interval size of the first eigenfunction decay constant s_1. An asymptotic analysis of eq. 2.33 [76] reveals that at long times and for large values of L the scaling of s_1 depends on α as

$$s_1 \propto \begin{cases} L^{-1} & 0 < \alpha < 1 \\ L^{-\alpha} & 1 < \alpha < 2 \\ L^{-2} & \alpha > 2 \end{cases} \tag{2.36}$$

This is a very important result since it gives the possibility to investigate superdiffusion without focusing on the mean square displacement. Despite the exponential time decay at long times resembles a diffusive behavior, the scaling of the decay constant of eq. 2.36 is another fingerprint of superdiffusive dynamics. This important result will be used in our experiments by investigating the scaling with L of the time-resolved transmission probability $T(L,t)$.

Another important anomalous scaling law of superdiffusion regards the probability $P_a(L)$ to be absorbed by the boundary, which for large L scales as

$$P_a(l) \propto L^{-\alpha/2} \tag{2.37}$$

with $0 < \alpha < 2$. Equation 2.37 holds both for Lévy walks and Lévy flights since $P_a(l)$ does not depend on time. Equation 2.37 is a generalization of

the Ohm's law of diffusion, indeed it gives the scaling of the probability to be transmitted through an interval of size L. The law of diffusion is retrieved for $\alpha = 2$. Such scaling law has been obtained first by Davis in [81] calculating the transmission probability of solar light through layers of clouds using discrete Lévy flights. Then it has been derived in [82] by using a Lévy flights with a CTRW approach.

CHAPTER 3

Optical gating for ultrafast time-resolved transmission measurements

Studies of the dynamics of light transport through pulsed experiments have been a key approach for the progressing and understanding of light transport in general [5, 83–86]. For example, for diffusive materials, such investigation allows to measure essential transport parameters as the diffusion constant. Many techniques employ picosecond pulses and fast photodiodes as detectors, which however limit the time resolution to some picosecond. Even streak cameras, which have the fastest responce among all electronic-based detectors, are limited in this sense. To go beyond this limit it is necessary to use an ultra-fast femtosecond source and an alternative approach for monitoring the transmission. A consistent part of this work has been devoted to the design and implementation of an optical gating setup, obtaining a femtosecond resolution and an excellent stability (time drift less than 1 fs per hour).

The optical gating (OG) technique is based on the use of a femtosecond pulse to probe optical intensities or field amplitudes evolving on a larger time-scale, exploiting the optical responce of a non-linear crystal. " To measure an event in time, a shorter event is required with which to measure it" , cit. Rick Trebino [87]. Optical gating has been widely used to achevie a sub-picosecond temporal resolution in time-resolved luminescence spectroscopy. A classical reference is that of Shah [88]. One of the first application of OG directed to the time-resolved investigation of transmitted multiple scattered light is that by A.G.Yodh et al. [89]. Other more recent applications involving detection of transmitted diffuse light are [30, 31, 90]. OG have been also employed to measure the time-resolved transmission from periodic and quasi-periodic photonic structures [91] [86].

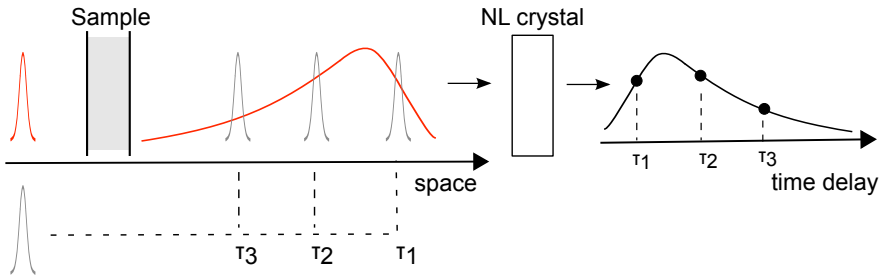

Figure 3.1 – Schematic of the optical gating technique to measure the intensity of transmitted light.

In this chapter we will introduce the basic concepts of optical gating and describe the experimental setup. Along the sections there are many experimental details and considerations which are necessary for the correct functioning of the set up. We also provide hints for the interpretation of the data. In the last part we include test measurements which have led, eventually, to interesting considerations. Finally we show the optical characterization of porous ceramics materials, thus providing additional insights on the potential of the setup.

3.1 Basics of Optical Gating

Optical gating involves the use of two ultrashort pulses, which can have the same frequency (central frequency of the pulse bandwidth) or two different frequencies. We consider the more general case of two pulses centered respectively at ω_1 and ω_2. The OG scheme is skeched in fig. 3.1. The probe pulse at ω_1 is directed on the samples, interects with its structure, and emerges with a streched temporal profile $I_{\omega_1}(t)$. The reference pulse at ω_2 travels undisturbed with its gaussian temporal profile $I_{\omega_2}(t)$. They are overlapped, in space and in time, in an optical non-linear crystal which is able to provide a sum-frequency generation $I_{\omega_1+\omega_2}$. This is a kind of frequency mixing that requires a non-vanishing second-horder susceptibility $\chi^{(2)}$ of the crystal [92, 93]. Sum-frequency generation is also known as upconversion.

We are interested in measuring the intensity temporal profile of the sum-frequency, which is given by the convolution

$$I_{\omega_1+\omega_2}(\tau) \propto \int_0^\infty I_{\omega_1}(t) I_{\omega_2}(t-\tau) dt \tag{3.1}$$

where τ is the time delay between the mixing components, set from an arbitrary reference time. Measuring the stationary signal $I_{\omega_1+\omega_2}(\tau)$ for different delays τ it is possible to reconstruct "frame by frame" the time profile of the sum-frequency. From this feature comes the name Optical Gating, which referes to the gate function of the reference pulse, which works as a temporal window of observation. The resolution depends on the pulse width and on the scanning delay time τ. The smaller is the delay τ the better

is the temporal resolution of the measurement. For this porpouse it is extremely advantagious to work with laser pulses since ultrashort temporal delay can be easily provided by reasonable spatial displacement of some microns, which ca be obtained by using a good mechanical traslation stage, e.g. a displacement in air of 1μm corresponds to a delay of 3 fs.

By measuring the sum-frequency evolution in time it is possible to retrieve $I_{\omega_1}(t)$ by performing the deconvolution of the measured profile from the reference $I_{\omega_2}(t)$. However the deconvolution requires a good knowlwdge of $I_{\omega_2}(t)$. It becomes much simpler when $I_{\omega_1}(t)$ is wider than the reference pulse $I_{\omega_2}(t)$ (as it is in all the measurements presented here). The pulse can indeed be approximated by a δ-function in eq. 3.1 resulting in the following simpler expression

$$I_{\omega_1+\omega_2}(\tau) \propto I_{\omega_2}(0) I_{\omega_1}(\tau). \tag{3.2}$$

In this case the temporal profile of the sum-frequency directly gives the time-evolution of the investigated signal. Moreover eq. 3.2 shows that the intesity of the sum-frequency, hence the signal-to-noise ratio, can be increased by transfering energy from both the probe and the reference pulse.

3.1.1 Phasematching conditions

Upconversion in efficient only if phase-matching conditions are satisfied, as the one required by momentum conservation

$$\vec{k}_{\omega_1} + \vec{k}_{\omega_2} = \vec{k}_{\omega_1+\omega_2} \tag{3.3}$$

where the $\vec{k}_i$ are the wave vectors of the mixing beams. Condition (3.3) has a simple expression for a collinear mixing geometry

$$\frac{n_{\omega_1}}{\lambda_1} + \frac{n_{\omega_2}}{\lambda_2} = \frac{n_{\omega_1+\omega_2}}{\lambda_{1+2}} \tag{3.4}$$

where n_i is the refractive index of the crystal at the frequency ω_i and λ_i are the vacum wavelength($\lambda_{1+2} = \lambda_1\lambda_2/\lambda_1 + \lambda_2$). In general it is not possible to satisfy the condition (3.4) in isotropic crystals, but it becomes possible considering birefringent (anisotropic) crystals, since n_i depends on the incident beams direction and on their polarization. In an uniaxial birefrangent crystal, of optic axis $\hat{z}$, with ordinary (O) index n_o and extraordinary (E) index n_e, phase matching can be obtained if one or more of the beams propagate as extraordinary. The matching is found by tuning the angle between the optics axis $\hat{z}$ and the incident beams direction, as shown in fig. 3.2. Negative uniaxial crystals ($n_e > n_o$) only admit sum-frequency signal with E polarization, i.e $O + O \rightarrow E$ and $O + E \rightarrow E$. Similarly, in positive uniaxial crystals ($n_o > n_e$) phasematching is possible only for O polarized sum-frequency beams, i.e. $E + O \rightarrow O$ and $E + E \rightarrow O$. When the incident beams have parallel polarizations (both O or both E), the interaction is termed type I; if they are polarized orthogonal, it is type II.

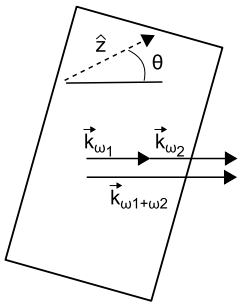

Figure 3.2 – Phase matching condition for the upconversion on the nonlinear crystal. In this configuration incident beams are collinear.

A conversion efficiency η is defined by looking at the generated power as in [94]

$$P_{\omega_1+\omega_2} = \eta P_{\omega_1} P_{\omega_2}. \tag{3.5}$$

One of the crucial parameter on which η depends is the phase mismatch

$$\Delta k = ||\vec{k}_{\omega_1+\omega_2} - \vec{k}_{\omega_1} - \vec{k}_{\omega_2}|| \tag{3.6}$$

The efficiency η falls off with incrising Δk as in

$$\eta(\Delta k) = \eta(0)\frac{\sin^2(L\Delta k)}{(L\Delta k)^2} \tag{3.7}$$

where L is the thickness of the nonlinear crystal. The dependence of the efficiency in eq. 3.7 is general and can be applied to different situations. For example, in a collinear mixing geometry, after having optimized the efficiency as required by eq. 3.4, relation (3.7) shows how the efficiency drops down in upconverting different wavelengths from λ_{1+2} . The same is valid for conversion of non collinear incident wavevector.

The conversion efficiency η depends on phasematching as well as on other parameters, especially working with laser pulses. Its optimization thus becomes a custom operation for each experimental geometry. See for example [95].

3.2 Experimental setup

The implementation of the optical gating technique for the ultra-fast detection of multiple scattered light has required the following basic building blocks: a laser source producing pulses with a temporal width shorter than the time-scale of the investigated dynamics, optical components for light propagation control, a non-linear crystal to generate the sum-frequency, a light detection apparatus with a wide dynamic range and a very good filtering of the environmental noise. The structure of the experimental setup is shown in fig. 3.3.

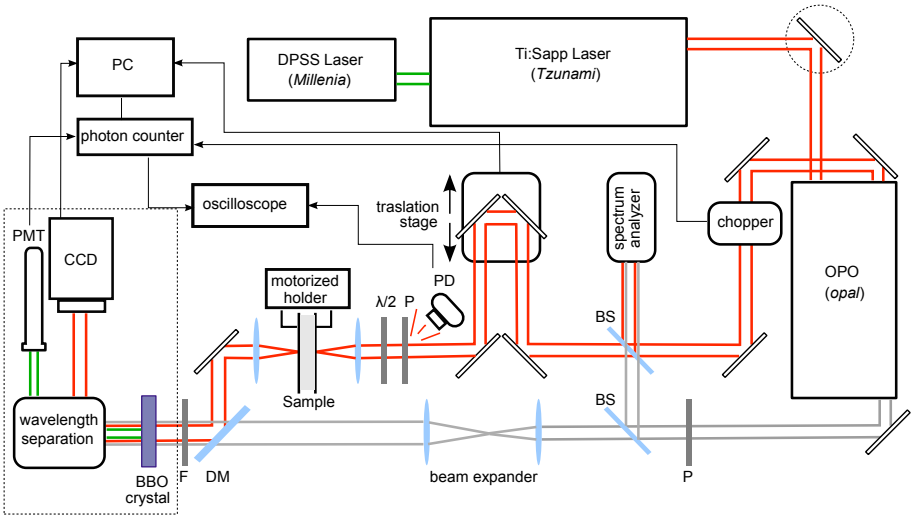

Figure 3.3 – Schematic of of the experimental setup: BS, beam splitter; P, polarizator; $\lambda/2$, half wave plate; DM, dicroic mirror; F, filter; PD, photodiode; PMT, photo multiplier tube. Dot contours indicate covering boxes.

3.2.1 Ultrashort pulses generation

The first laser in the setup is a *Millenia* from Spectra Physics, a DPSS (Diode-Pumped-Solid-State) CW laser emitting light at 532 nm (green) with a power of 8.61 W, which is used to pump a *Tzunami* laser from Spectra Physics. The Tzunami is a Ti:Sapphire mode-locked laser generating pulses of 130 fs at 810 nm with a repetition rate of 82 MHz (red beam in fig. 3.3). The spectral bandwidth of the pulses is 8 nm, which is constantly monitored by the spectrum analyzer. Such features correspond to good alignment conditions, providing an average output power of 1.70 W. The folded geomentry of the cavity allows in principle to tune the pulse wavelength by about 100 nm around the central frequency of 810 nm, but we have not changed the wavelength in the experiments.

Pulses from Tzunami are directed into an Optical Parametric Oscillator, *Opal* from Spectra Physics, to convert part of the energy into a train of pulses with central wavelength 1540 nm (gray beam in fig. 3.3). They have the same temporal width and repetition rate of the generating pulses, with a spectral bandwidth of 25 nm. The wavelength conversion is obtained by a nonlinear sum-frequency process on an LBO crystal, identical to the one introduced in Section 3.1. However this conversion is time-reversed compared to that in Section 3.1 and the phase-matching is reached through a temperature tuning of the crystal refractive indices. Opal has a wide tunability in the converted signal, ranging from 1400 to 1600 nm. In our configuration the wavelengths generated out of the 810 nm pulse train are $\lambda_{signal} = 1540$ nm and $\lambda_{idler} = 1700$ nm, plus a non converted residual harmonic at 810 nm. The power of the residual harmonic, which is directed on the sample, is 280 mW, while pulses at 1540 nm are used as the reference pulses in the optical

gating process.

3.2.2 Mixing the pulses

The setup is characterized by two optical lines, as shown in fig. 3.3. The probe line at 810 nm (in red), which is directed on the sample, and the reference line at 1540 nm (in gray). On the probe line we find in sequence: a beam splitter sending part of the light on the spectrum analyzer; the translation stage, which is computer controlled and allows tuning of the time delay between the transmitted signal and the reference pulse; a polarizer and an half-waveplate used to define the injection linear polarization; the sample, which is fixed on an holder mounted on two coupled computer controlled translation stages which allow to move the sample along the plane orthogonal to the beam; a first lens for focusing the light on the sample and a second lens for collecting the transmitted light and imaging it on the nonlinear crystal; a dicroic mirror for the overlap with the reference pulse; a nonlinear BBO (*beta* barium borate) crystal for the frequency mixing. On the reference line we find in sequence: a linear polarizer; a beam splitter sending part of the light on the spectrum analyzer; a couple of lenses for expanding the beam in order to fill the BBO surface; the dicroic mirror to allow the overlap with the light transmitted from the sample;

In principle the translation stage could have been positioned also on the reference line, since what matters is the relative delay between the probe and reference pulse. The couple of lenses on the probe beam have been selected depending on the effective collection area we wanted to achieve. We have implemented two different configuration of optics, one for measuring the on-axis transmission an one for measuring the total transmission. The tuning of the collection area is performed by tweaking the magnification of the transmitted profile image obtained with the collecting lens. The image in created on the BBO plane and only the portion of light falling within the BBO surface is converted, and then measured. Looking at fig. 3.4 the choice of the focal length f of L2 has to be related to the sample-lens distance d and the lens-BBO distance p, since the magnification is given by $M = p/d$. For the positioning of L2 it is also necessary to take into account the desired collection angle.

The BBO crystal is mounted on a holder which allows to vary its orientation in space with two degrees of freedom, θ and φ, in order to find the phase-matching configuration, see also fig. 3.4.

3.2.3 Sum-frequency detection

The BBO converts part of the incoming energy into the sum-frequency at 531 nm, which is the green line in fig. 3.3 and fig. 3.4 . The element placed before the BBO is a high-pass filter blocking the on-axis green light coming from the environment. The detection apparatus is indeed very sensitive to the on-axis green light and this filter assures that we are measuring only the

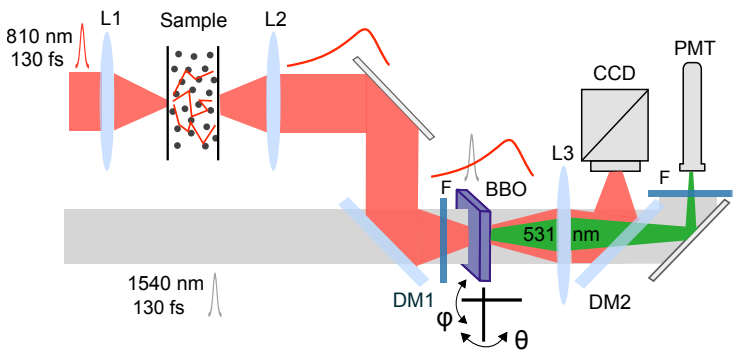

Figure 3.4 – Detailed schematics of the light injection, collection and conversion components in the experimental setup.

on-axis green light generated by the BBO. To block the off-axis environment green light we protect the detection components with a black shielding box. Since the unconverted light crosses the BBO in line with the sum-frequency we need to select the green. We first remove the 810 nm light by using the dicroic mirror DM2 (see fig. 3.4), which deviates this wavelength on the CCD camera. A band-pass filter placed before the photomultiplier tube ensures a cleaner green signal. The sum-frequency at 531 nm is detected by a photomultiplier tube, which has a wide dynamic range of seven orders of magnitude. Lens L3 of fig. 3.4 is positioned so as to image the different wavelength on both the CCD and on the PMT. Its working wavelength is 810 nm since the aberrations induced on the image of the PMT does not affect the PMT response. For the background noise suppression the photomultiplier response (signal) is sent to a Gated Integrator Photon Counter. Simultaneously the signal is chopped by chopping the probe beam. Th chopper is set on a 20 Hz angular frequency so as to define a step signal with a period of 50 ms, whose two values are A =signal+background and B =background. The gated integrator defines two temporal windows of width $T_w \leq 25$ ms where A and B are read separately. The returned signal is $A - B$, which is background suppressed. The chopper provides the trigger signal for the synchronization of the acquisition temporal windows with the periodic signal from the photomultiplier. The gated integrator thus generates a sequence of windows A and B with the same period of the signal, which is usually out-of-phase with the signal. The gated integrator allows the tuning of the phase of the periodic acquisition windows independently. Thus we send their periodic time evolution on the oscilloscope together with a real-time detection of the chopped light, which is monitored by means of a photodiode collecting the light scattered from the polarizer.By monitoring simultaneously all three signals we can perfectly fit one acquisition window in the detection semi-period of A and the other acquisition window in the semi-period of B.

3.2.4 Determination of the absolute time-zero

What we want to measure is the distribution of optical time-of-flights, hence the distribution of times necessary for the light to travel throughout the sample. Consequently the zero of time must coincide with the time at which the probe pulse touches the first sample surface. This is crucial for example to correctly extract information from the light transmitted at earlier times. Indeed the rising time of the transmission is strictly related to the sample thickness. One of the reason is that it can still contain a ballistic contribution. A wrong set of the time-zero, which for example delays the zero, could show some light crossing the sample in a period of time smaller than the ballistic crossing time. On the contrary anticipating the zero could result an affective arrival time characteristic of a more scattering material. A correct set of the time-zero is crucial when using fitting function as the solution of the diffusion equation in a slab. Such model indeed considers the source placed on the front surface of the slab at time zero.

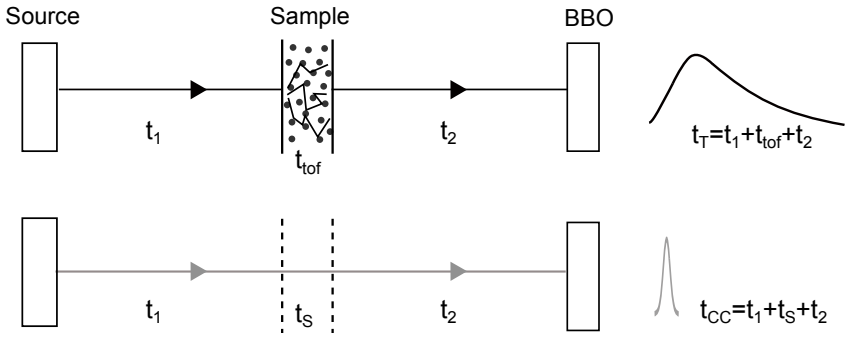

Figure 3.5 – Schematic of the total time delay accumulated by the measured transmission (black line) and the cross correlation (gray line) before reaching the BBO crystal.

The reference measurement is the cross correlation of the pulse, which is obtained by removing the sample and scanning the sum-frequency signal by moving the translation stage, see fig. 3.5. The cross correlation measurement obtained in the first stage consists in the pulse intensity distribution as a function of the translation stage position. The sample is then placed on the probe line and the transmission is scanned in the same range of positions, see fig. 3.5. In fig. 3.6(a) we show the typical result of such procedure. The first thing to do is to multiply times two the position values of the translation stage. Indeed each displacement step of the translation stage increases or decreases the path-length of the probe pulse of twice the size of the step. We can then convert path lengths in time by dividing the position values by the velocity of light in air c. The obtained time axis is shown in fig. 3.6(b).

The reported times are relative to an arbitrary reference time which does not have a precise physical meaning, but is the same for both signals. What matters is the difference between the reported times. However such difference does not directly give the time-of-flight. Let us call t_T the time of

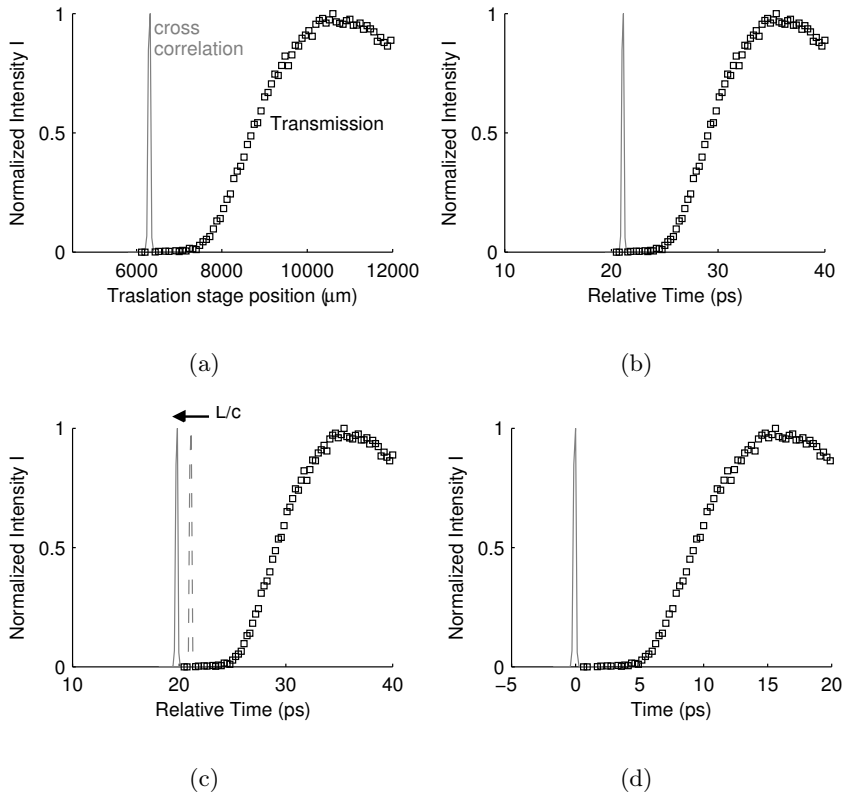

Figure 3.6 – Important steps to correctly set the time-zero for a time-of-flight distribution measured with our setup. (a) Rough measurements of the cross correlation (scan of the probe pulse without sample) and of the transmission as a function of the translation stage position. (b) The spatial delay induced by the translation stage is converted in a common relative time delay. (c) The cross correlation is shifted back of the time necessary for the probe pulse to cross the sample. (d) Time-shift of both measurements to set as time-zero the time position of the shifted cross-correlation.

detection of the transmitted light the t_{cc} the time of detection of the cross correlation. As shown in fig. 3.5 the times t_T include the travel time t_1 to go from the source to the sample surface, the time-of-flight t_{tof} inside the sample and the time t_2 to travel from the sample rear surface to the BBO. Similarly t_{cc} includes t_1 and t_2 plus the time t_s necessary to travel a distance in free space equal to the sample thickness. It follows then that $t_T - t_{cc} = t_{tof} - t_s$ and thus that the true time-zero is not t_{cc} but $t_0 = t_{cc} - t_s$. In fig. 3.6(c) we show how the cross correlation is shifted back by $t_s = Lc$, where L is the sample thickness, to be placed at time t_0. It is now possible to shift the time axis to place the cross correlation at $t_0 = 0$, so that each point of the transmission curve corresponds to a time-of-flight value, as shown in fig. 3.6(d).

3.2.5 Influence of phasematching on the measured up-conversion

Here we discuss more in details the influence of eq. 3.7 on the up-conversion of multiple scattered light. In particular we refer to the conversion obtained using the optics configuration of fig. 3.4. One of the main features of multiple scatted light is that the direction of of k-vectors is completely random. Assuming for instance that the collection angle of the imaging lens is so wide to image on the BBO all k-vectors of the transmitted profile, how many of them are up-converted ? Equation 3.7 states that the conversion efficiency is narrow around the direction of phase-matching. In the employed alignment procedure we have optimized the phase-matching using collimated parallel beams. It was done without the sample and removing the focusing lens and collecting lens. A good phase-matching was usually obtained for the BBO orientation angles $\theta = 18°$ and $\varphi = 160°$ as well as for $\theta = 17°$ and $\varphi = 172°$. Such choice implies an efficient conversion only in the forward direction, thus for k-vectors parallel to the optical axis, see fig. 3.7. The angle of efficient conversion is roughly $\delta \approx 6°$. This estimation has been obtained by converting the image of the focalized source, which can be considered a point source, and by looking at the angle of aperture of the converted light. Despite the

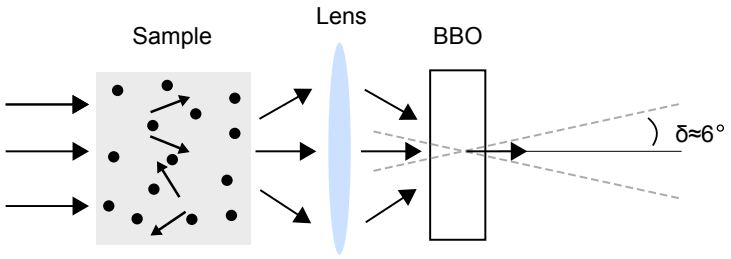

Figure 3.7 – In our setup configuration the phase matching condition, required by the nonlinear conversion on the BBO, limits the range of directions for converted k-vectors to a narrow solid angle around the optical axis.

the non-linear conversion performs a narrow filtering of k-vectors that is not a real problem for our measurements. Indeed multiple scattering quickly randomizes k-vectors directions distributing them uniformly over the whole solid angle. This means that the converted part of k-vectors are a good representation of the temporal behavior of the entire transmission. As we will see in the next section what becomes crucial for a correct interpretation of the measurements is the collection area rather than the effective collected k-vectors.

3.3 Dependence on the collection area: the diffusive case

As a consequence of multiple scattering the light injected on the surface of a disordered slab laterally spreads and the exit area on the rear transmission surface is larger than the injection one. This defines a transmission profile. In a homogeneous disordered samples, where light spreads following the laws of diffusion, the profile has a gaussian-like energy density distribution. This is evident in the radial dependence of the time-resolved transmission of eq. 1.45. The energy density distribution in steady state can be calculated by integrating eq. 1.45 over time [25]. The width of a diffusive transmission profile scales linearly with the thickness of the sample. It is interesting that its dependence on the transport mean free path l_t is much weaker than the dependence on the thickness L, which dominates.

When performing transmission experiments it is thus imperative to control the collection area on the rear surface of the sample. In fig. 3.8 we show the time-resolved transmission predicted by diffusion theory for an increasing collection area. The curves have been obtained with a numerical integration over the radial distance ρ of eq. 1.45. The intensity is normalized in order to underline the behavior of the tails. Collecting light from an area smaller than the whole profile definitely affects the slope of the tail. We compare the curve with the total transmission model in eq. 1.47 observing that the limit of total-transmission is fully reached only when the collection area radius R is twice the sample thickness. The calculation of fig. 3.8 have been obtained for $L = 50\mu$m and $l_t = 1\mu$m, with a velocity of light in the medium $v = c/1.5$. However the limit of $R = 2L$ is valid for any situation since the profile grows linearly with L.

In fig. 3.8 we also show the dependence of the slope of the tail (in semilog scale) on the collection area and on time. We see that in order to observe the same slope of a total transmission measurement, thus the same decay constant, it is necessary to wait very long times. However, for an on-axis collection ($R = 0$) the slope does not reach that of the total transmission even after of eight order of magnitude of decay.

The considerations exposed become relevant for a measure of the diffusion constant obtained by measuring the long-time decay constant, see eq. 1.49. If the collection area is not large enough the measured value of the diffusion constant can be erroneous.

3.4 On-axis transmission configuration

In order to measure only the on-axis transmission we have imaged on the BBO surface the very central area of the transmitted profile with a diameter of 30 μm. The necessary big magnification is obtained by imaging with two coupled lenses, since the constraint on the sample-BBO distance (imposed by the beam-overlapping configuration) did not allow to use only one

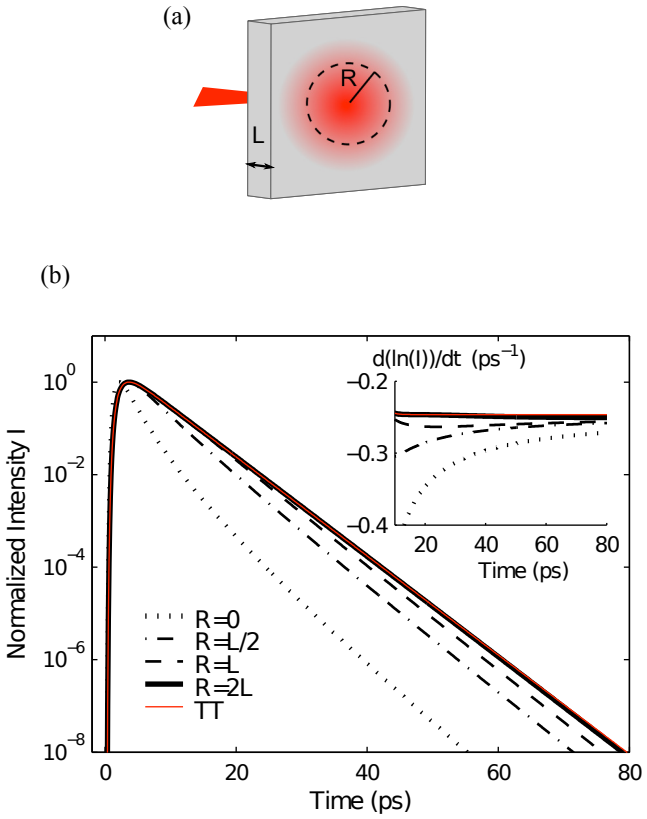

Figure 3.8 – Dependence of the time-resolved transmission on the collection area as predicted by diffusion theory. (a) Sketch of the transmission profile and definition of a collection area with radius R. (b) Time resolved transmission as a function of the collection area size as predicted by diffusion theory. The radius R influences the decay rate of the transmission. The equivalence with the total time-resolved transmission is reached for R=2L. In the inset we show the dependence of the slope of the curve (in semilog scale) at long times. Except that for the on-axis collection the total-transmission decay rate can be reached, but at very long times

lens. The lens arrangement is showed in fig. 3.9. In this particular configuration we have injected light on the sample with an aspheric lens L1 of NA=0.65 and $f1$=1.5 mm to obtain a tight focal spot of few microns. The first collecting lens $L2_1$ is also an aspheric lens of NA=0.65 and focal length $f2_1$=1.5 mm placed at distance $f2_1$ from the sample rear surface. The second lens $L2_2$ is a doublet with a long focal length $f2_2$=30 mm placed at a distance $f2_2$ from the BBO. The distance between the coupled lenses was of about 100 mm. In order to test the setup performance we have carried out measurements on a set of samples whose light transport properties can be well described by diffusion theory. The first test measurements have been performed on a sample of TiO_2 nanoparticles homogeneously dispersed in a polymer matrix. The sample is prepared in a slab geometry of thickness

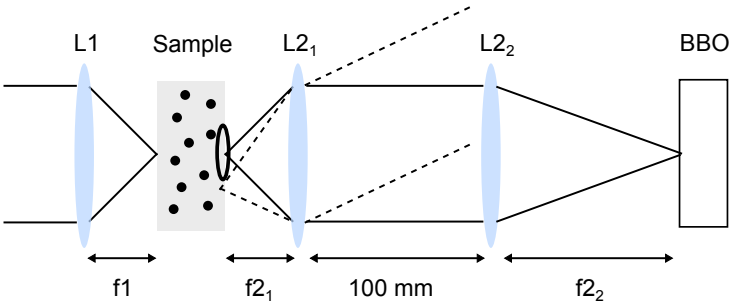

Figure 3.9 – Configuration of the lenses for the on-axis measurements. Light is tightly focused with L1. For the collection and imaging of transmitted light we employed to coupled lenses. $L2_1$ expands the image so that at the position of $L2_2$ only light coming from the desired central area is accepted by the second lens. The obtained magnification is of about 100×.

392 μm. More details on the preparation method of such kind of samples can be found in Chapter 6. Here it is important to say that considering the nanoparticles density, cross section and anisotropy coefficient, the expected transport mean free path is l_t=10μm. In fig. 3.10 we show the measurements with the fit obtained using eq. 1.45 with $\rho = 0$, which corresponds to an on-axis transmission model. The returned best-fit scattering mean free path is l_t=10.63±0.06μm. In fig. 3.10 we show both the linear plot and the semilog plot in order to hightlight the non-exponential tail of the on-axis transmission. Both kinds of plots will be used along the thesis. Such measurement have been a test for the correct functioning of the setup.

3.5 Total transmission configuration

We have also configured the setup to measure the total time-resolved transmission by injecting light with a focused source and by converting on the BBO the whole transmitted profile. This kind of measurement is more challenging with respect to the on-axis one since the up-conversion needs to be uniform for the whole image of the transmitted profile. For example it requires a very good alignment of the probe and of the reference beam on the BBO, an appropriate choice of the imaging lens magnification and tuning of the reference beam width. We did not employ the more handy reciprocal configuration that will be discussed in Section 3.6 since the main purpose of the total transmission measurements was to investigate light transport in strongly heterogeneous disordered media. Indeed in the configuration (b) of fig. 3.13 an heterogeneous disorder would imply an heterogeneous distribution of the generated point sources, both on the surface and in depth. Such feature could invalidate the equivalence with configuration (a).

We have used the scheme in fig. 3.4. Light is focused with a doublet lens of focal length f1=25 mm resulting in a focal spot of about 20 μm. The transmitted profile is collected and imaged on the BBO through a biconvex

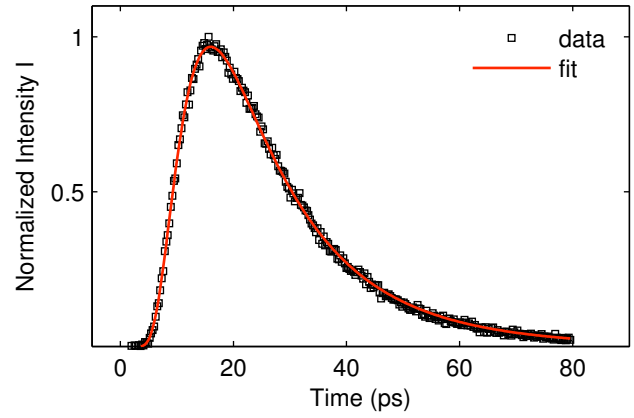

(a)

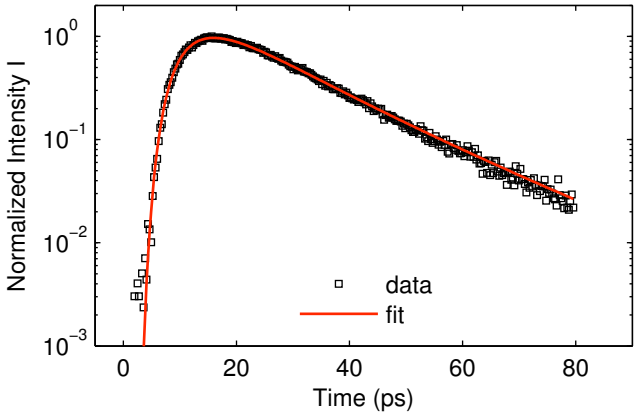

(b)

Figure 3.10 – On-axis time-resolved transmission measurement through a slab of diffusive material. The red line is the fit obtained with the on-axis transmission model of diffusion theory. The obtained best fist scattering mean free path is in good agreement with the value expected from sample preparation. (a)Plot in linear scale. (b)Plot in semilog scale to highlight the feature of the tail.

lens with focal length f2=75 mm positioned 180 mm from the BBO. Such choice has been the best trade-off to satisfy also the constraints of the setup design. The obtained magnification allows to completely fit the profile image on the BBO surface. The size of the profile image is monitored by re-imaging it on the CCD through a biconvex lens with focal length f3=100 mm. The imaged area of the sample surface has a diameter of 3 mm and the whole transmitted profile falls down this area. The reference beam covers the BBO surface with its central part in order to overlap the profile image with an homogeneous energy density.

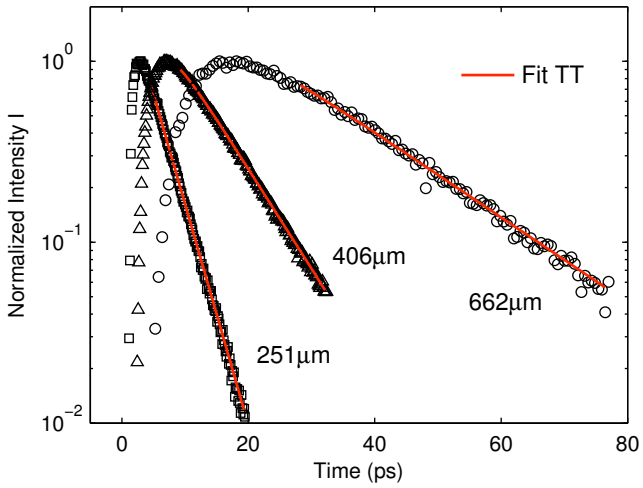

Figure 3.11 – Total time-resolved transmission of 3 homogeneous disordered samples with thickness respectively of 251μm, 406μm and 662μm. All samples are prepared with the same concentration of scatterers. The measurements have been obtained by injecting light with a focused beam and collecting light from a large area on the rear surface of the sample. The late time transmission can be described by the diffusive total-transmission model for all the measured thickness, giving the same transport mean free path for all samples. This is a proof of the good performance of the setup in such configuration. The time-range of each measurement is limited by the presence of reflections generated by the glass slides embedding the samples.

We have performed the test measurements on the same kind of samples used for the on-axis configuration test measurements, which are slabs of TiO_2 nanoparticles homogeneously dispersed in a polymer matrix. These test measurements are related to the work presented in Chapter 4. The main purpose has been to verify that the tail of the transmission at long times can be well described by diffusion theory in a specific sample thickness range. In fig. 3.11 we show the measurements performed on three different samples with thickness ranging between 251-652 μm. They are prepared with the same concentration of nanoparticles thereby having the same transport mean free path. A fit of the tail performed by using the total transmission model of eq. 1.47 returns for all the samples $l_t = 42.0 \pm 0.5$ μm. This observation is a good proof for the reliability of the setup.

The impossibility to fit the early-time part of the measurement has been object of further investigation. Such interest has generated the work presented in Chapter 6.

3.6 Evidence of reciprocity for diffused light

We have experimentally verified the possibility to measure the total transmission of a diffusive slab with an on-axis collection by injecting light with a collimated beam. Such possibility is hypothesized for example in [25] regarding the applicability of the total transmission model to light propagation in a diffusive slab. We have performed the measurement on the same sample used for the characterization of fig. 3.10. In fig. 3.12 we show the measurement obtained by injecting light with a collimated beam and the corresponding fit obtained by using the diffusive total transmission model (see eq. 1.47). The fit returns a transport mean free path l_t=10.30 $\pm$ 0.31μm. We show together the transmission obtained by injecting light with a focused source. This corresponding fit is obtained by using the on-axis transmission model which returns l_t=10.63$\pm$0.06μm. Both collection models works very well returning comparable values of the transport mean free path. The comparison in fig. 3.12 highlights the dramatic effect that the change in the source type has on the time-resolved transmission. We have already discussed how the

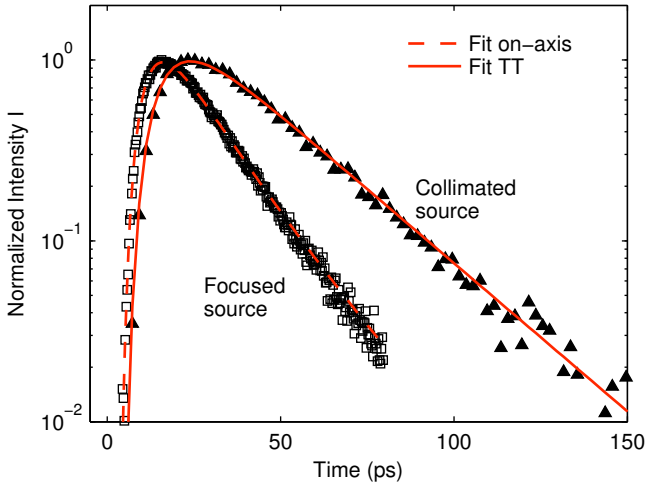

Figure 3.12 – On-axis transmission measured by injecting light with a focused and collimated source on the same sample. The measurement obtained with the collimated source is successfully fitted with a total transmission model. This is allowed by the validity of reciprocity for diffused light.

time-resolved transmission represents the optical time-of-flight distribution. In particular in a total transmission measurement it gives the distribution of time-of-flight from one single point on one side of the sample to any other point the opposite side of the sample. In the configuration (a) of fig. 3.13 such distribution is measured by fixing the starting point of light and measuring the time-of-flight in correspondence of all the other points on the opposite surface. Instead in the configuration (b) of fig. 3.13 the arrival point is fixed and the time-of-fligh distribution is measured by changing the

starting point of light. Indeed a plane wave on the sample surface creates a uniform distribution of point sources.

Such equivalence has his root in the the reciprocity relation, which is a manifestation of the symmetry of scattering processes with respect of an inversion of time. Reciprocity allows to interchange the source and the detector in an experiment obtaining the same result. A more detailed discussion on the reciprocity relation can be found, among others, in [13] [96]. Looking at fig. 3.13 we can see how one configuration becomes equivalent to the other by reversing the direction of light propagation, which is equivalent to an inversion of time. However, as pointed out in [96], reciprocity and time-reversal symmetry are not the same. The condition for time-reversal invariance is equivalent to both energy conservation and reciprocity, therefore a scattering system may be reciprocal without being conservative.

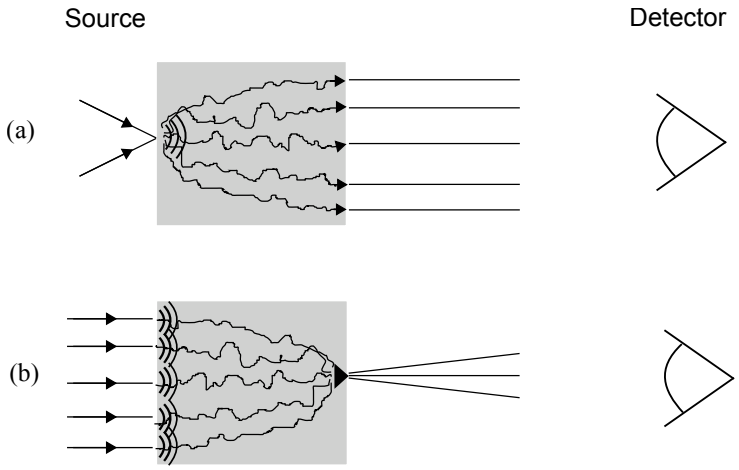

Figure 3.13 – Sketch of the equivalence of the total optical random paths (from one point to the opposite surface) acquired in a standard total transmission configuration (a) and in the employed configuration (b). One configuration becomes equivalent to the other by reversing the direction of light propagation.

3.7 Measurements on porous ceramics

We have characterized the optical properties of porous ceramics material by employing the on-axis transmission configuration. This work is part of a collaboration with the Lund University (Sweden) and the Institute for Ceramic Materials SWEREA IVF in Mölndal (Sweden). The collaboration has investigated the possibility of pore-size assessment by measurements of the oxygen absorption line broadening caused by wall collisions of gas confined in the porous materials. Our contribution has investigated the effect of an increasing porosity on the optical transport mean free path. This is an interesting issue since scattering properties of porous materials, vary strongly with the microstructure (and wavelength) [97].

Samples are nanoporous zirconia ceramics which present high refractive index (n=2.14) and very low absorption in the near-infrared region. Below we also report some details on their preparation method and the porosity measurement performed by mercury intrusion at SWEREA IVF. The text in this section is largely taken from the article we wrote on this topic [3].

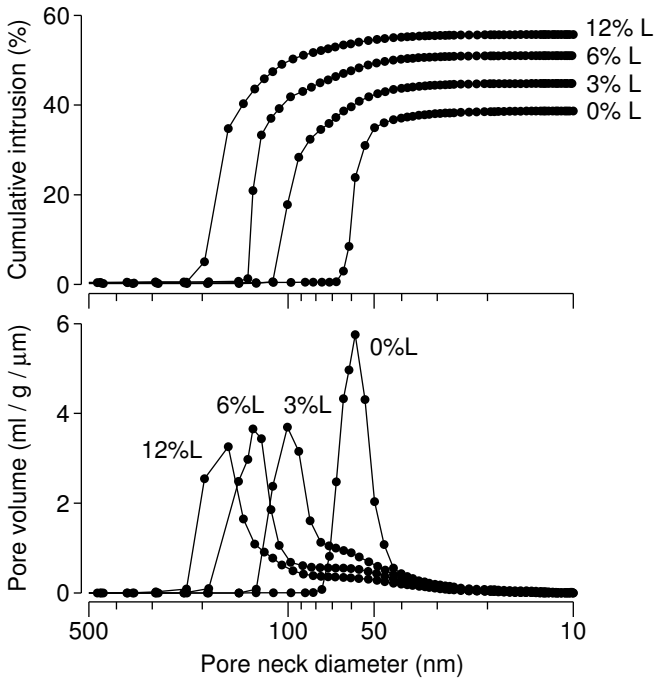

Figure 3.14 – Mercury intrusion porosimetry of nanoporous zirconia.The pore size of the zirconia material was fine-tuned by adding latex particles as spacers later to be burned away (not being a part of the final material). Cumulative intrusion curves show how smaller and smaller pores are filled as higher mercury pressures are applied (note reverse direction of scale, pressure increase to the right). At high pressures, intrusion comes to a halt and the final level gives the material porosity. Clearly, both porosity and pore size increase as the used concentration of spacers increase. The bottom graph shows the pore size distribution (the derivative of cumulative intrusion). Without latex particles (0% L), the mean pore neck size is 54 nm and the porosity is 38.7%. Having added 12% latex particles (12% L), the mean pore neck has grown to 131 nm, and the porosity to 55.7%. Note also that addition of spacers broadens the pore size distribution. In particular, a small fraction of the pore volume remains constituted by pores of the size characteristic of the material sintered using a pure zirconia powder (curves in the bottom graph exhibits a tail stretching towards smaller pore diameters). Picture and text from [3].

		Pore neck diameter (nm)	
	Porosity, ϕ (%)	Mean	Median
0% L	38.7	54	57
3% L	44.8	80	92
6% L	51.0	104	126
12% L	55.7	131	164

Table 3.1 – Summary of pore structure of the zirconia materials as measured by mercury intrusion porosimetry. The samples are denoted according to the amount of latex spacer particles used during sintering (0, 3, 6 and 12% L). Table from [3]

3.7.1 The nanoporous zirconia ceramics

The investigated nanoporous zirconia materials are sintered ceramics. An aqueous suspension with a 50vol% solids loading of ZrO_2 (TZ3YSE, Tosoh, Japan) and 0.3wt% of dispersant (Dolapix PC 75, Zschimmer-Schwarz, Germany) was prepared by ball milling with milling media of zirconia. A latex emulsion (LDM 7651S, Celanese, Sweden) with solid content of 50vol% and a particle size of 150 nm was added as binder. Suspensions with 0, 3, 6 and 12 wt% of binder were slip cast on porous plaster moulds. When the porous mould absorbs water from the suspension, the particle density close to the mould surface increases until particle-particle contacts are formed. During this consolidation process, a cast material (powder compact) is formed particle by particle. Due to the electro-steric stabilisation of the particles, homogenous particle packing and high density can be obtained.

When using a binder consisting of particles, the suspension will still have the same solids loading but the ceramic particles will be diluted. During the casting process, where the so called green body is formed (i.e., the unsintered ceramic item), the binder particles will occupy some space in between the ceramic particles. This will increase both the porosity and pore size in the cast material (if only the ceramic material is considered). This also means that the casting process can be used to prepare ceramic powder compacts with different porosity and pore size distributions without any changes of the raw material or the sintering process.

The cast green bodies were allowed to dry at room temperature before sintering in air at 900°C for two hours in a SiC furnace (Entech, Sweden). During this process, organic additives (including the latex material) are burned out and a zirconia ceramic without additives is obtained. The density measurements were performed by the Archimedes method and the pore size distribution was studied by mercury intrusion (Micromeritics, USA). The results of the mercury intrusion porosimetry is shown in fig. 3.14, and key characteristics of the pore structure are summarized in Tab. 3.1.

3.7.2 Optical properties

For dense heterogenous media, such as the ceramics studied here, the link between pore structure and optical properties is complex and not well understood. The bright white appearance of our ceramics clearly indicate strong multiple scattering and relatively weak absorption. Zirconia is known to have very low absorption in the near infrared region [98, 99], and absorption coefficients smaller than 0.01 cm^{-1} have been reported for nanoporous tetragonal zirconia ceramics of the type studied here [97]. The scattering properties of porous materials, on the other hand, vary strongly with microstructure (and wavelength) [97, 100]. For the experiments in focus here, macroscopic light transport is the key aspect, and the strong scattering ensures that this process follows diffusion theory.

The delay line of our set up limits the time range to 300 ps, so to capture a substantial part of the diffusion dynamics, measurements were performed on samples polished down to a thickness of 500 μm. The transport mean free path was determined by fitting standard slab geometry diffusion theory [25] to the measured photon time-of-flight distribution. In this procedure, the absorption coefficient was assumed to be zero, and the effective refractive index was approximated using a volume average of the two components (ZrO2 with $n = 2.14$, pores with $n = 1$). The results are shown in fig. 3.15. The materials are indeed strongly scattering, having transport mean free paths ℓ_{tr} around 1 μm. Note, for example, that no light appears before 50 ps, which roughly corresponds to a 10 mm pathlength, or 20 times the sample thickness.

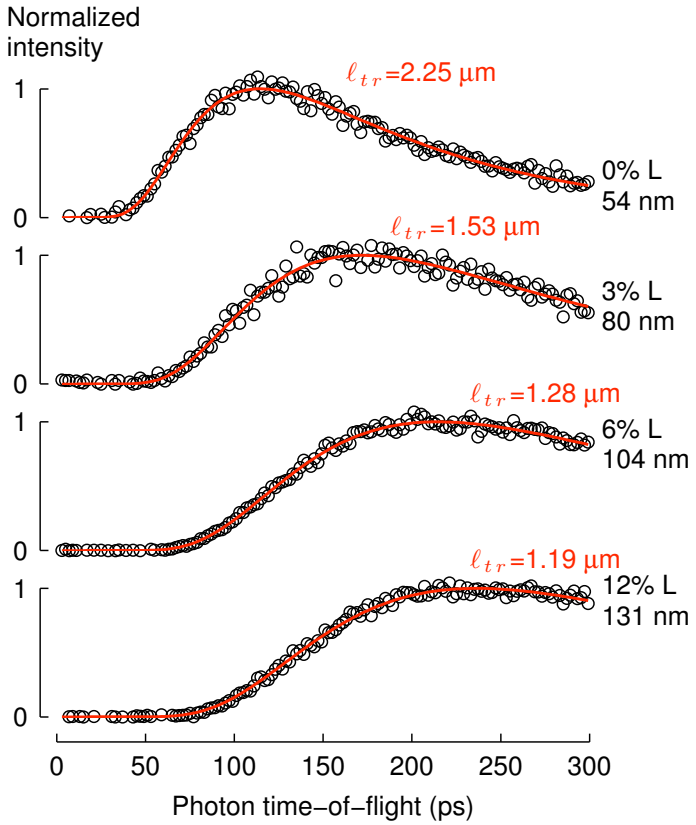

Figure 3.15 – Time-of-flight distributions for light transmitted through 500 μm thick slabs of the zirconia materials. The increase in pore size caused by the addition of more and more latex spacer particles is clearly accompanied by a significant increase in scattering. The time-of-flight distributions are shifted to longer times, and diffusion modeling (red solid lines) reveals a significant reduction in transport mean free path ℓ_{tr} (fitted vales stated in graph). A time-of-flight of 300 ps, being the longest time probed, correspond to a path of about 6 cm. Picture and text from [3]

CHAPTER 4

Superdiffusive dynamics for light

In this chapter we focus the interest on Lévy glasses, optical disordered material characterized by a fractal-like heterogeneity. In Lévy glasses light scattering regions are separated by spherical heterogeneities, whose diameters are distributed according to a power-law. Lévy glasses give the opportunity to investigate in-lab the basic laws of transport of complex fractal-like systems, like the cloudy atmosphere [81] or the internet network [55, 56].

The heterogeneity of Lévy glasses creates a critical broadening of the optical step-length distribution, causing the divergence of the steps variance on the length scale of the system. Such disorder topology can drive the transport to be anomalous, in particular superdiffusive [2, 57, 101–108].

When Lévy glasses have been introduced by Barthelemy et al. [1] they showed evidence of superdiffusion of light by means of steady state optical characterizations. However superdiffusion is a dynamical process and static characterizations do not rigorously prove anomalous transport. A less elusive observation needs to probe the scaling features of the propagator in a dynamic regime.

Here we experimentally investigate the dynamics of light transport in Lévy Glasses by means of ultrafast time-resolved transmission measurements. In particular we probe the pulse response of samples with different thickness. By applying scaling arguments we retrieve information on the shape and on the scaling of the propagator.

4.1 Lévy glasses

Lévy glasses are prepared by dispersing TiO_2 nanoparticles in a monomer host and by including glass microspheres with a size-dependent distribution. Nanoparticles act as very good light scatterers due to their high refractive index ($n = 2.4$). Glass microspheres are instead index-matched with the monomer ($n_0 = 1.52$) and do not scatter light. Their only purpose is to act as spacers and mold the distribution of scatterers in space. This method for engineering the disorder was introduced recently [1] [101] and provides very good control of the disorder heterogeneity. The basic steps of the preparation procedure are shown in fig. 4.1.

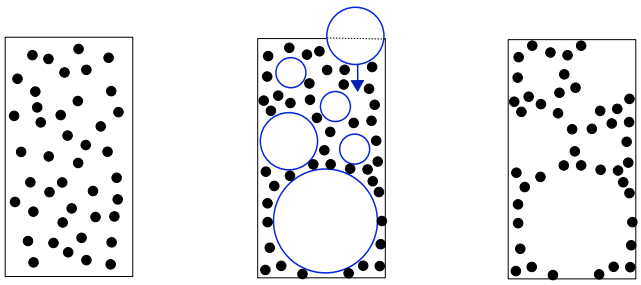

Figure 4.1 – Sketch of the technique employed to mold the scatterers (black circles) in space. The refractive index of the microsphere matches that of the hosting monomer so that light doest not scatter on the spheres surface.

In Lévy glasses we use 18 different spheres diameters categories in the range 5-400 μm. The number of spheres N_i for each diameter category ϕ_i is distributed according to the power-law

$$N_i = C(\beta)\phi_i^{-(\beta+1)}. \tag{4.1}$$

The exponent β determines the degree of heterogeneity of the sample and can be arbitrary tuned. The smaller β is the higher is the probability of finding large spheres, thus large region of space free of scatterers. The constant $C(\beta)$ depends on the total number of spheres in the samples.

The power-law spheres distribution creates a fractal-like heterogeneity in the disorder over two order of magnitude. Indeed the probability distribution to find a void of size ϕ decays as the power-law $P(\phi) \propto \phi^{-(\beta+1)}$, which is a scale invariant function. The fractality of the heterogeneity is intended in a statistical sense, see Section 2.1. It defines a characteristic self-similarity in the structure, which is well captured in the sequence of images of fig. 4.2. For this reasons we refer to β as to a fractal parameter.

In Lévy glasses light scatters only in the region filled with nanoparticles while propagate undisturbed through a sphere. The length of the free step inside the sphere depends on the diameter of the sphere and on the direction of propagation. It follows that the global step-legth distribution is heavily affected by the spheres distribution and will be likely characterized by a "heavy tail".

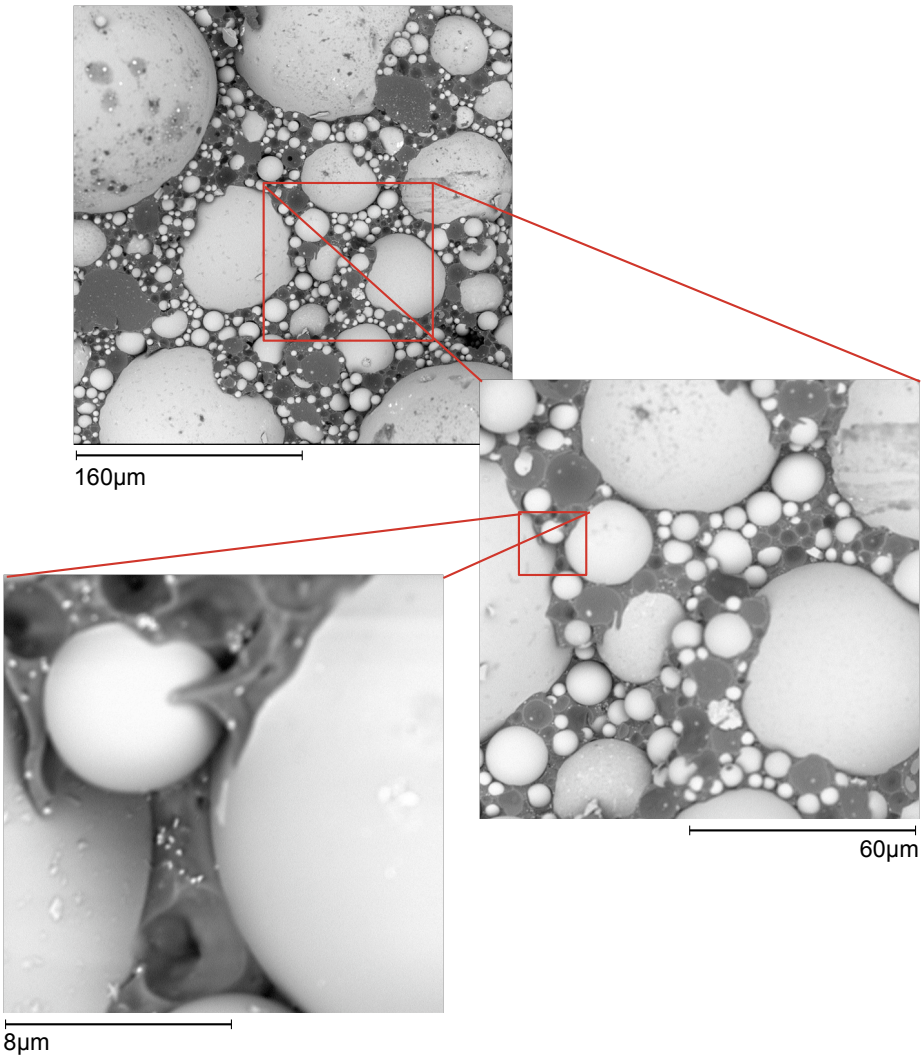

Figure 4.2 – Sequence of images of the surface of a Lévy glass obtained with a scanning electron microscope (SEM), with respectively increased magnification. Microspheres are in light gray while the polymer is dark gray. Unlike optical wavelengths, for which the two media are indistinguishable beeing index matched, electrons scattering can clearly discern between them. Such images well capture the sample self-similarity of Lévy glasses until the length scale of the smallest components emerges. In the last close-up the TiO_2 nanoparticles are clearly visible as white dots.

A broad step-length distribution implies a diverging variance, which is the hypothesis for superdiffusion. That's why Lévy glasses are the optimal substrates to establish a superdiffusive transport of light. In fig. 4.3 we sketch some random trajectories of light in a sample assuming one scattering event between spheres, which resemble the trajectories of a Lévy walk. In addition to steps of few microns also much larger steps of hundreds of microns are allowed.

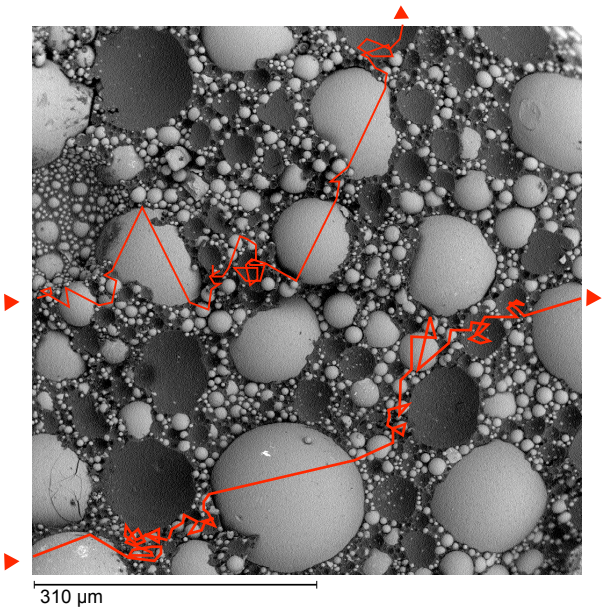

Figure 4.3 – SEM image of the surface of Lévy glass. Red lines sketch light trajectories during propagation in the samples. Each sphere (light gray) represents a free-propagation region since scatterers are distributed only in the polymer (dark gray).

4.1.1 Samples preparation

Titanium dioxide nanoparticles belongs to the Tioxide R-XL series sold by Huntsman, which have an average diameter of 280 nm and are coated with an inorganic layer (silica, aluminia) to prevent clustering. We calculated an average refractive index $n = 2.4$ considering the refractive index of titanium dioxide for both light polarization directions. The monomer is the Norlan 65 acrylate optical adhesive from Thorlabs whose refractive index is $n_0 = 1.52$. Glass microspheres are Soda Lime glass microspheres from Duke Standards whose refractive index is $n_s = 1.5$. We have used the following diameter categories expressed in microns: 5, 8, 10, 15, 20, 30 ,40 ,50, 70, 100, 120, 140, 170, 200, 230, 280, 330, 400.

The desired spheres number distribution of eq. 4.1 is obtained by selecting the weight W_i of each diameter category as

$$W_i = \rho_s V_i C(\beta) \phi_i^{-(\beta+1)}, \tag{4.2}$$

where $\rho_s = 2.5$ mg/mm^3 is the specific weight of Soda Lime glass and $V_i = 4\pi(\phi_i/2)^3/3$ is the volume of the single sphere of diameter ϕ_i. For $\beta = 2.0$ the scaling exponent of the spheres number is opposite to the scaling exponent of the spheres volume so that the dependence of W_i on ϕ_i disappears. We have set $W_i(\beta = 2.0) = 15$ mg. In such case the constant $C(\beta)$ can be expresses as $C(\beta = 2.0) = 6W_i(\beta = 2.0)/\pi\rho$. For other values of β the corresponding $C(\beta)$ is obtained by imposing that the total weight of spheres is kept constant, thus equal to the $\beta = 2.0$ case.

Nanoparticles are first homogeneously dispersed in the monomer by means of steering (10 minutes) and sonication (1 hour) at 50°, a temperature at which the monomer is still fluid and does not polymerize yet. We did not use additional solvent to facilitate the dispersion of the particle since after some trials using dichloromethane (DCM) solvent some solvent residuals were still present in the final sample. Glass microspheres are separately weighted and added to the homogeneous dispersion of nanoparticles. The spheres clustering, which takes place is particular for some sphere diameters, is reduced by manual grinding. The mixture of monomer is homogenized by manually mixing it for about one minute at 50-70 C°.

Samples are manufactered in a slab geometry by squeezing the mixture between two microscope glass slides untill the the sample thickness matches the largest sphere diameter, see fig. 4.4. In order to obtain samples with a different thicknesses L, all the spheres categories with a diameter larger than L are removed. Since the monomer is necessary to host both the nanoparticles and the microspheres its volume has to be enough to embed completely all the components of the mixture. It implies that the amount of monomer has to grow with the sample thickess. In the prepared samples the amount of monomer is proportional to the total volume of spheres. We have then set the amount of nanoparticles proportional to the amount of monomer in order to keep fixed the nanoparticles density between spheres. A Lévy glass with maximum spheres diameters of 230 μm contanins 42 mg of monomer and 5 mg of titanium dioxide powder. Such preparation method keeps fixed the spheres filling fraction and the nanoparticles concentration over the entire volume for all samples, setting them respectively to $ff_{\text{spheres}} = 71\%$ and $ff_{TiO_2} = 1\%$.

For each category the distribution of the sphere diameters are distributed around the mean value $\overline{\phi}_i$, which is the official diameter provided by the seller. Thereby in each set there are microspheres with a diameter bigger than $\overline{\phi}_i$. The biggest spheres determine the thickness of the sample, which can deviate from the mean value $\overline{\phi}_i$ also of 10% . In order to measure the thickness of the sample first we measure the thickness of the microscope slides and then the thickness of the prepared sample at the end of the fabrication process. Since the thickness cannot be uniform over the sample plane we mark the characterized area of the sample surface in order to perform the optical characterization on that part. Thickness measurement are performed by means of a digital micrometer from Mitutoyo (Japan). In order to obtain a detailed map of the thickness homogeneity the arms of the micrometer have a spherical tip in order to minimize the surface of contact during the measurement. The accuracy of the instrument is of $\pm 3\mu$m.

The final stage of the preparation procedure is the sample exposure to UV radiation in order to polymerize the monomer. Polymerization makes the monomer solid, thereby it "freezes" the element positions in the slab geometry. Thanks to the low amount of monomer and the low density of scatterers the structure becomes solid after 10 minutes of irradiation for each side. Polymerization causes a permanent adhesion of the microscope slides

on the sample surface. As shown in fig. 4.4 the microscope slides are index matched with the polymer. Choosing glass slides with the same refractive index of the sample gives an index matching condition at the boundaries, see fig. 4.4. The nanoparticles contenent gives a negligible contribution to the effective refractive index of a sample which remains of 1.5.

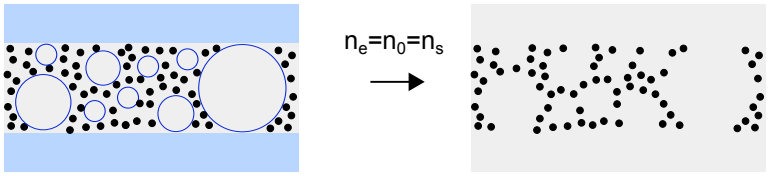

Figure 4.4 – Lévy glasses are prepared in a slab geometry matching the slab thickness with biggest sphere diameter. The sample is embedded between two microscope slides (n_e) index matched with the polymer (n_0) and spheres (n_s).

4.1.2 The chord-length model

A first approach to derive the step-length distribution for a random walk in a Lévy glass is by applying the chord-length model. Such model assumes a single scattering event between spheres, thus neglecting any sphere multicrossing and any small steps between spheres. Mainly in this model the spheres filling fraction is supposed to be close to unity. In this view the length of a single step always corresponds to the length ζ of a chord in the crossed sphere. It follows that the step-length distribution is equivalent to the distribution $P(\zeta)$ of sphere chord-length in the sample.

An analytical expression for the chord-length distribution can be found in eq. 5.10 in Chapter 5. In general the distribution $P(\zeta)$ presents a "saw-toot" behavior due to the triangular shape of the chord-length distribution for a single sphere.

The chord-length model has been applied in [101] to approximate the step-length distribution in Lévy glasses with a well defined spacing between diameter categories. In particular they have considered an exponential or polynomial spacing. In such case the tail of the step-length distribution decays with a rather defined power law

$$P(\zeta) \propto \frac{1}{\zeta^{\alpha+1}}, \tag{4.3}$$

and the exponent α is simply related to the exponent β of eq. 4.1 and eq. 4.2 as [101]

$$\alpha = \begin{cases} \beta - 1 - 1/s & \text{(polynomial spacing)} \\ \beta - 1 & \text{(exponential spacing)} \end{cases} . \tag{4.4}$$

The experimental diameter spacing does not follow exactly an exponential or a polynomial function, since the sphere sizes mainly depends on the commercial availability. It can be arguable to state if the obtained spacing is closer

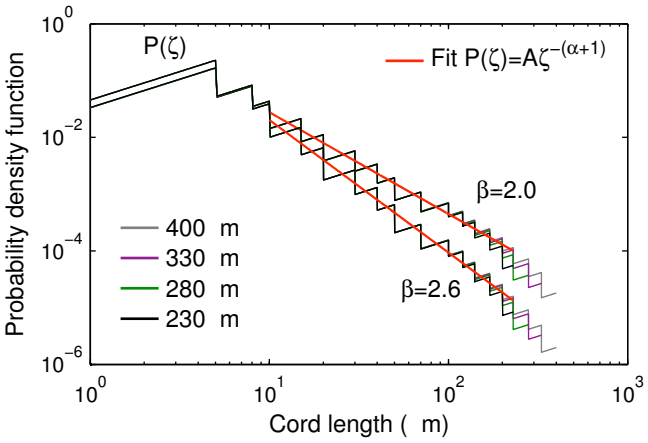

(a)

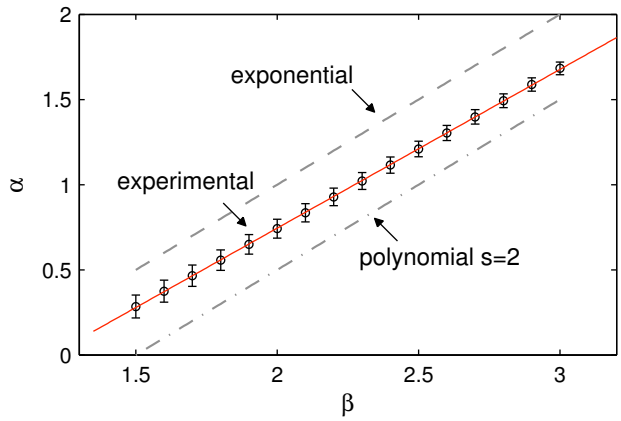

(b)

Figure 4.5 – Application of the chord-length model to infer the step-length distribution of light inside a real Lévy glass sample. (a) Chord-length distributions calculated considering the experimental spacing of diameter categories, for two values of β. (b) Our analysis shows that the relation $\alpha(\beta)$ in real Lévy glasses deviates from the theory formulated for ideal exponential or polynomial sampling.

to either an exponential or a polynomial. This point has been also rised in [108]. Here we have directly applied the chord-length model to the experimental situation and analyzed the obtained distribution of chord length. In fig. 4.5(a) we show the real sample distribution $P(\zeta)$ for two values of β and for different thickness of the sample.

The distributions do not decay as a single power law. Moreover removing the largest spheres category there is an effect on the very final part of the distribution tail since some chord lengths are removed. To extract an effective power-law behavior like that in eq. 4.3 we have performed a fit with

a linear function of $\log(P(\zeta))$ in function of $\log(\zeta)$. In particular the fit is performed in the central part of the tail over three order of magnitude, where the distribution is less affected by the truncation. The best-fit angular coefficient gives the exponent α of eq. 4.3. Compared to a power-law fit in linear scale the employed fitting method gives to all the points of the tail the same weight regardless of the much smaller absolute value of some of them. We have performed the fit for the four sample thicknesses selecting the mean of the fitted exponents as best estimation and the semi-interval of variation as the corresponding error. We have carried out the investigation for different values of β and calculated the associated α. The analysis leads the following empirical linear relation between the two exponents

$$\alpha = \ (0.932 \pm 0.004)\beta + (1.12 \pm 0.01) \quad \text{(experimental spacing)}. \tag{4.5}$$

As we show in fig. 4.5(b) such relation lays in the middle between the exponential and polynomial spacing case. This means that, given the same degree of approximation, the experimental spacing can be approximated by both an exponential and a polynomial function. It is interesting to show how the α derived using eq. 4.5 for samples with $\beta = 2.0$ and $\beta = 2.6$ are respectively $\alpha = 0.7$ and $\alpha = 1.3$ and that the value we obtain assuming an exponential spacing are instead $\alpha = 1.0$ and $\alpha = 1.6$. These values are particularly useful for the experimental results presented in the next sections.

4.2 Observation of anomalous scaling of light dynamics

We have investigated the dynamics of light transport in Lévy glasses by means of ultrafast time-resolved transmission measurements, which is used to determine the optical time-of-flight distribution. We have employed the optical gating setup presented in Chapter 3 in the total-transmission configuration. We have thus injected ultrashort pulses of 130 fs at 810 nm on the sample surface and monitored the time-evolution of the transmission. Thanks to the available femtosecond resolution we could observe both the transient and stationary regimes of transmission.

Together with Lévy glasses we have investigated the pulse response of reference samples characterized by homogeneous disorder. These samples are prepared with the same volume concentration of scatterers by substituting the glass spheres of Lévy glasses with the same volume of polymer. The only difference between Lévy glasses and reference samples is in the spatial distribution of scatterers. The same kind of sample has been used for the work presented in Chapter 6 and more details on the preparation method can be found in Section 6.4.2.

4.2.1 Pulse response of a Lévy glass

In fig. 4.6(a) we show a sequence of measurements performed on a Lévy Glass with β=2.0 and thickness L=434μm for different pulse injection points. We see the strong dependence of the early-time transmission upon the source position. This signature is missing when measuring reference samples. In fig. 4.6(b) we show the averaged curve obtained on a set of 40 different source positions, for both the Lévy glass and the reference sample. The aim of this plot is to better highlight the peculiar shape of the Lévy Glass transmission.

Early-time fluctuations are somehow expected, given the strong heterogeneity of the sample. However they are of particular importance since they provide evidence of light which can quickly couples to the exit surface thanks to very long steps. Moreover, there are some positions located over the entrance surface where the probability to be transmitted is enhanced. The maximum value in the early-time transmission is achieved injecting light in correspondence of one of the biggest sphere. A more accurate statistical investigation of these fluctuations would require measuring on thousands of injection spots. The underlying distribution of early-time peak values would certainly give structural information on the sample. This will be object for further investigations. In this work we focus on the transmission at long times, which has a stable, position-independent, behavior.

Long-time transmitted light has travelled a long path to reach the sample boundary, experiencing many scattering events and probing plenty of different disorder configurations. For example the first light after the smoothing of the fluctuations have travelled a distance five times longer than the sample thickness.

The long-time transmission is a single decaying exponential of lifetime τ. At this moment the transport has reached ergoticity since the decay rate is constant and the injection-point dependence disappears. In particular the lifetime τ gives the average time needed by light to probe a generic region of size L. This is coherent with the observation that the transition to the ergotic regime is completed after a period of time comparable to τ.

Thanks to the simultaneous and clear observation of low-order scattered light and very high-order scattered light fig. 4.6 unveils the transition to ergoticity, which is usually hidden in homogeneous disordered media.

4.2.2 Scaling of the lifetime

The light of the tail in fig. 4.6 has significantly interacted with the sample, completely probing its topology. Hence the tail represents an important fingerprint of the transport. Despite an exponential tail characterizes also a diffusive time-resolved transmission, it does not imply that what we observe is diffusion. Indeed the exponential decay can be seen as a natural consequence of the eingenmodes decomposition on a finite-size system. What matters is the scaling of the tail since it reflects the scaling of the propagator.

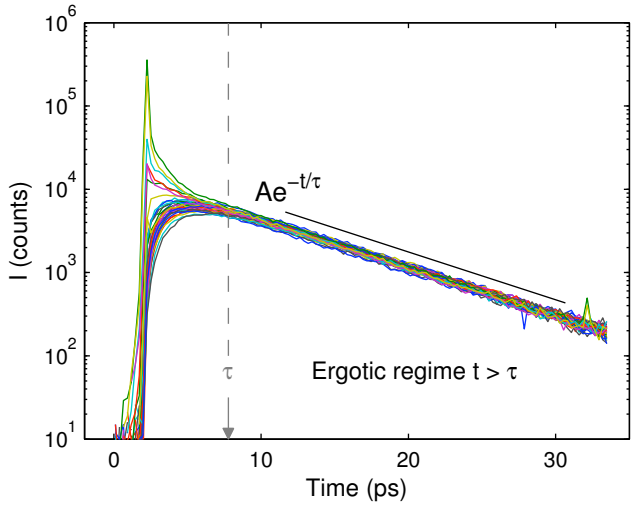

(a)

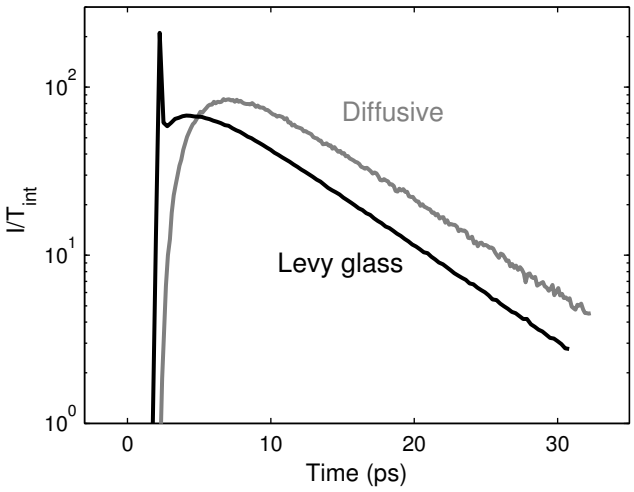

(b)

Figure 4.6 – Pulse response of a Lévy glass with β=2.0 and L=434μm. The y-axis is in log-scale. (a) Each curve corresponds to a different pulse injection point on the sample surface. Early-time transmission strongly depends on the injection point position. On contrary the late-time transmission is an exponential decay with a single characteristic lifetime (b) Pulse response averaged over 40 different source positions compared to the averaged pulsed response of a reference diffusive sample with thickness L=406μm. To correctly compare the intensity of transmission the measured counts have been normalized to the integration time T_{int}. The picture highlights the difference in the shape of the two responce. The late-time lifetime of the two samples are similar but they are not directly comparable since the Lévy glass is thicker than the reference samples.

We have performed a scaling investigation by measuring the time-resolved transmission on samples with different thickness, focusing on the long-time decay. We have investigated two sets of samples, with β=2.0 and β=2.6, with thickness spanning between 230-450 μm. All the measurements resemble the features of fig. 4.6, decaying exponentially with a typical lifetime τ.

Regardless of the type of transport dynamic we expect τ to scale according to the following law

$$\tau = \frac{L^{d'_w}}{B}, \tag{4.6}$$

where d'_w is the fractal dimension of the underlying random walk and B is a constant with dimensions $[\mathrm{m}^{d'_w}/\mathrm{s}]$.

The walk dimension d'_w determines the scaling of the time-dependent characteristic length $\xi(t) \propto t^{d'_w}$ which rescales the propagator (see Section 2.1.2). For standard diffusion $d'_w = 2$ while for superdiffusion $1 < d'_w < 2$. The use of the prime symbol will be clear later on.

We have measured τ for each sample by fitting the tail of the single point measurement with the exponential function $A\exp(-t/\tau)$ with A and τ free parameters. From the obtained set of best-fit τ values we have selected the mean value as best estimation of the lifetime and the standard deviation of the mean as the associated error. The lifetime is always very stable under source position averaging. In order to get a small statistical error, 20-30 measuring points are enough.

In fig. 4.7 we show the thickness dependence of τ for the samples with β=2.0. We plot together the fit of the points obtained using eq. 4.6, which returns the scaling exponent d'_w=1.1±0.2. Applying the same procedure to the samples with β=2.6 we measure d'_w=1.3±0.2. This is a remarkable observation since both values of d'_w are significantly smaller than two. Moreover the scaling exponent is sensitive to the fractal parameter β, thus to the degree of heterogeneity of disorder. We could not extend the investigation to a wider range of thickneses since the preparation of thicker samples is challenging. On the other hand a characterization on smaller samples would have implied too weak scattering.

To reinforce the observation and test the proper functioning of the experimental setup we have investigated reference samples featuring the same range of thickness. In fig. 4.7 we show the thickness dependence of the lifetime for this sample set, to directly compare it with the scaling of Lévy glasses. We plot together the expected lifetime predicted by diffusion theory, which have been calculated using

$$\tau_{\mathrm{diff}} = \frac{(L + 2z_e)^2}{\pi^2 D}, \tag{4.7}$$

where D is the diffusion constant and z_e the extrapolation length. We have used the expressions $D = v_e l_t/3$ with $v_e = c/n$ and n=1.52, then $z_e = 2l_t/3$ and l_t=42μm. The transport mean free path l_t has been measured indepen-

dently by comparing the measured transmission with Monte Carlo simulations. As we can see from fig. 4.7 reference measurements are in good agreement with diffusion theory, but deviates from the scaling of Lévy glasses. This definitely confirms the presence of anomalous transport dynamics in our samples. The measurement of l_t for the reference samples is part of the work presented in Chapter 6 and can be found in Section 6.2.

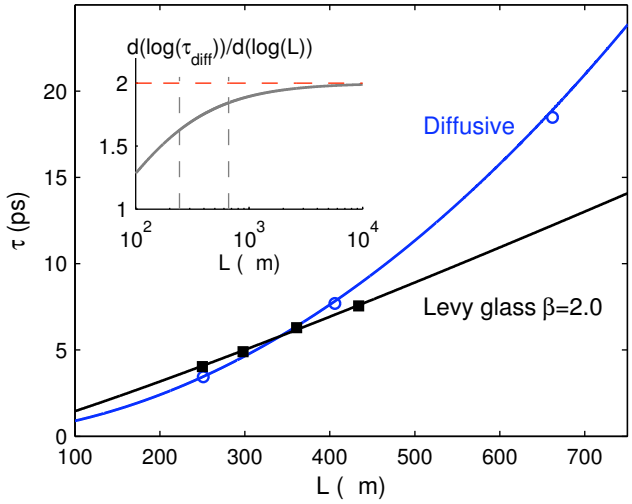

Figure 4.7 – Measured scaling of the lifetimes for the Lévy glasses with β=2 and for reference samples. Error bars are smaller than the marker size. Reference samples lifetimes correctly follow diffusion theory (blue line). The scaling observed for of Lévy glasses is instead anomalous. The fit of the data (black line) gives a walk dimension d'_w which is significantly smaller than two. (Inset) Converges to the asymptotic value d_w of the diffusive pre-asymptotic walk dimension d'_w as predicted by diffusion theory.

4.2.3 Comparison with a Lévy walk

The scaling observed for Lévy glasses, $d'_w < 2$, is predicted for a Lévy walk. However the correspondent theory [76] is developed considering a bounded system in the asymptotic limit. So we now are on the intriguing point regarding the possibility to model the observed anomalous scaling in terms of a Lévy walk and thus of superdiffusive dynamcs. We need to understand if the measured scaling exponent d'_w have already reached the asymptotic value d_w. This is the reason why we adopted the prime symbol for the measured exponents, since they can still be pre-asymptotic walk dimensions.

Important evidences comes from the scaling of the reference samples. For homogeneous disorder samples the asymptotic limit corresponds to the condition $L \gg l_t$, which is not satisfied in our thickness range. Indeed a fit of the experimental data with eq. 4.6 returns $d'_w = 1.8 \pm 0.3$, which is clearly a pre-asymptotic value. To retrieve the asymptotic walk dimension $d_w = 2$ in our thickness range, it becomes crucial to introduce an extrapolation

length, as shown in eq. 4.7. For diffusive finite systems the extrapolation length z_e is proportional to l_t [33]. The correction on the thickness value it provides allows extending to finite-size systems the zero boundary conditions used to solve the diffusion equation, which are implicit in the quadratic scaling of eq. 4.6. This is known as the extrapolated boundary condition, where the energy density is set to zero at extrapolated boundaries located at distant z_e from the physical boundaries. This is valid for any L, hence for diffusive media the asymptotic limit corresponds to thicknesses for which the distance z_e is negligible. In the inset of fig. 4.7 we show the convergence to the asymptotic limit value of the diffusive pre-asymtotic walk dimension $d'_w = d(\log(\tau_{\text{diff}}))/dL$ as a function of the sample physical thickness L. As we see the asymptotic value is reached at very large thickness. The average of the calculated pre-asymptotic values, within our thickness range, gives indeed the d'_w measured on reference samples.

We might expect that also for Lévy Glasses the measured d'_w is still a pre-asymptotic walk dimension. In this scenario we cannot model the observed anomalous scaling with a pure Lévy walk. For this purpose we need to derive a first approximate method to retrieve the asymptotic value d_w.

4.3 Thickness correction to retrieve the asymptotic limit scaling

In a scaling analysis the asymptotic limit is reached when all the effects on the scaling procedure of the characteristic lengths of the transport are negligible, except for the effect of the investigated characteristic length. When this regime is not reached the measured walk dimension deviates from the asymptotic value. Reference samples clearly show such effects. In this case the characteristic length influencing the scaling is the transport mean free l_t. However we have shown that the correction provided by the extrapolation length z_e allows to retrieve the asymptotic walk dimension in a pre-asymptotic thickness range

To define the pre-asymptotic regime for Lévy glasses it would be necessary to identify the characteristic lengths of the transport and test their effect on the scaling. Due to the complexity of the disorder topology this is a rather complex issue to tackle. For example the transport in Lévy glasses is deeply non-local and there is not a typical step length analogous to l_t .

However, as we show in eq. 5.6 in Chapter 5, the fixed volume concentration of scatterers characterizing Lévy glasses makes the mean step $\langle l \rangle$ constant for all sample thicknesses. It follows that $\langle l \rangle$ is a characteristic length for all samples, even if it is not a good estimator of the broad step-length distribution. In particular the mean step $\langle l \rangle$ of a generic heterogenous scatterers distribution equals the mean step of the homogeneous counterpart, e.g. a sample with the same number of scatterers homogeneously distributed. Since we know the transport mean free path of the reference samples, which are the homogeneous counterpart of Lévy glasses,

we have $\langle l \rangle = l_t = 42\mu$m for all samples thickness and β values.

We propose a first approximation for the superdiffusive extrapolation length, capable to retrieve the asymptotic walk dimension for finite-size Lévy glasses. On the basis of the previous result such extrapolation length is equal to the diffusive one $z_e = 2/3\langle l \rangle = 2/3 l_t$.

We have applied the above procedure for measuring the walk dimension adding this correction to the thickness of Lévy glasses, thus scaling as a function of the effective thicknesses $L_{\text{eff}} = L + 2z_e$. In Table 4.1 are reported the obtained walk dimensions. As we see the observation of superdiffusion is not invalidate, although there is a variation of the value. Still within the approximation the measured d_w are the dimensions of a Lévy walk for light.

Samples set	d'_w	d_w
Lévy Glasses β=2.0	1.1±0.2	1.3±0.2
Lévy Glasses β=2.6	1.3±0.2	1.5±0.2
Diffusive samples	1.8±0.3	2.0±0.1

Table 4.1 – Measured pre-asymptotic and asymptotic walk dimensions for all samples sets. Errors have a statistical confidence of 95%.

4.3.1 Data collapse

In fig. 4.8(a) we show the whole time-resolved transmission for the set of Lévy Glasses with $\beta = 2.0$, averaged over the source positions. Our purpose now is to use the measured walk dimensions for an axes rescaling. We use the asymptotic d_w and the effective thicknesses L_{eff}. We rescale the time axis as $t \to t/L^{d_w}$. To retrieve the rescaling of the intensity axis we employ an energy conservation argument. In the asymptotic limit the total transmission of a Lévy walk scales with the thickness as $T \propto L^{-d_w/2}$ for $1 < d_w < 2$, which is a generalization of the Ohm's law for light [81, 82]. Imposing that the integral over time of the measurements scales following such dependence, we retrieve a rescaling for the intensity axis $I \to IL^{3/2d_w}$. This rescaling procedure can be merged in the following scaling form

$$I(t, L) \propto L^{-\frac{3}{2}d_w} \tilde{I}\left(\frac{t}{L^{d_w}}\right), \tag{4.8}$$

where $\tilde{I}$ is a single unknown master curve. This technique is commonly used in the scaling theory to derive information on the scaling exponent of the propagator [107]. Inserting the typical walk dimension of the transport in eq. 4.8 all the different curves of 4.8(a) are expected to collapse on the master curve $\tilde{I}$. In fig. 4.8(b) we show the obtained data collapse. This good result is a clear signature of the anomalous scaling of the propagator in Lévy glasses. We obtain a similar good collapse also for the Lévy glasses with $\beta = 2.6$, using the corresponding asymptotic walk dimension. In fig. 4.9 we show the collapse obtained for the reference samples, which, as expected, is optimal for $d_w = 2$.

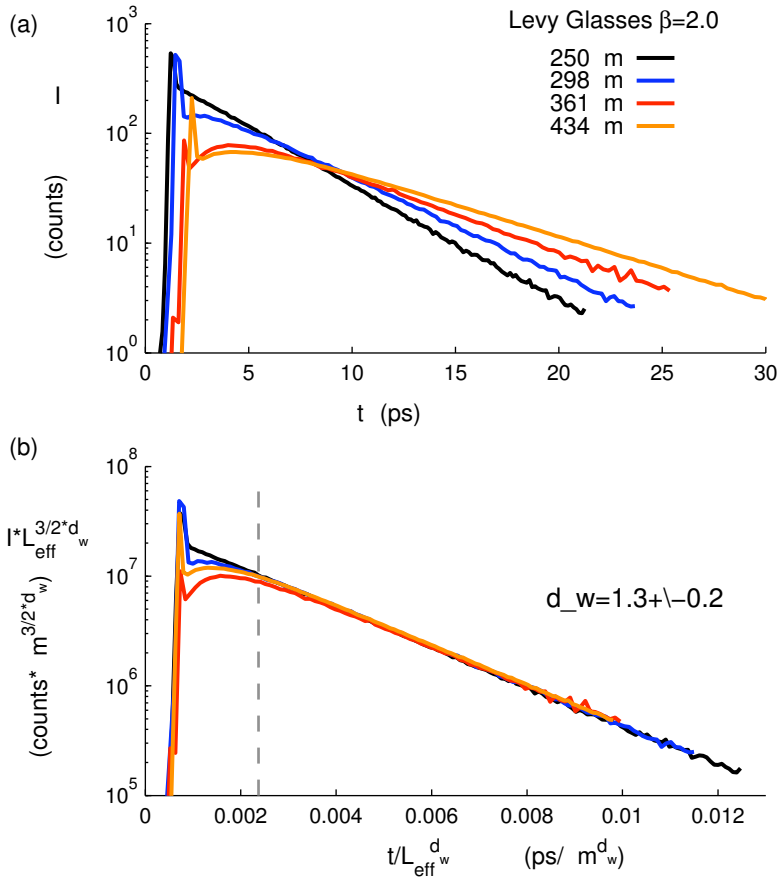

Figure 4.8 – Data collapse of the time-resolved tails for Lévy Glasses with $\beta = 2.0$. (a) Unscaled measurements for four sample thickness averaged over 20-30 points; (b) Scaled measurements using the effective sample thickness and the asymptotic walk dimension d_w. The dashed line define the beginning of the ergotic transmission regime, which is statstically relevant. This explains why the collapse quality drops at early times

We see how for Lévy glasses the quality of the data collapse drops at early times, but this is expected since only the light of the tail is statistically relevant. The intensity rescaling is fairly good also using the pre-asymptotic walk dimension and the physical samples thickness. This suggests that the scaling hypothesis can be extended to pre-asymptotic conditions.

4.4 Complexity of transport

The observation of anomalous transport we have presented so far is independent from any model used to describe the physical process. We have considered an ensemble of scattering nanoparticles randomly distributed and probed the transport regime of light for different degree of disorder het-

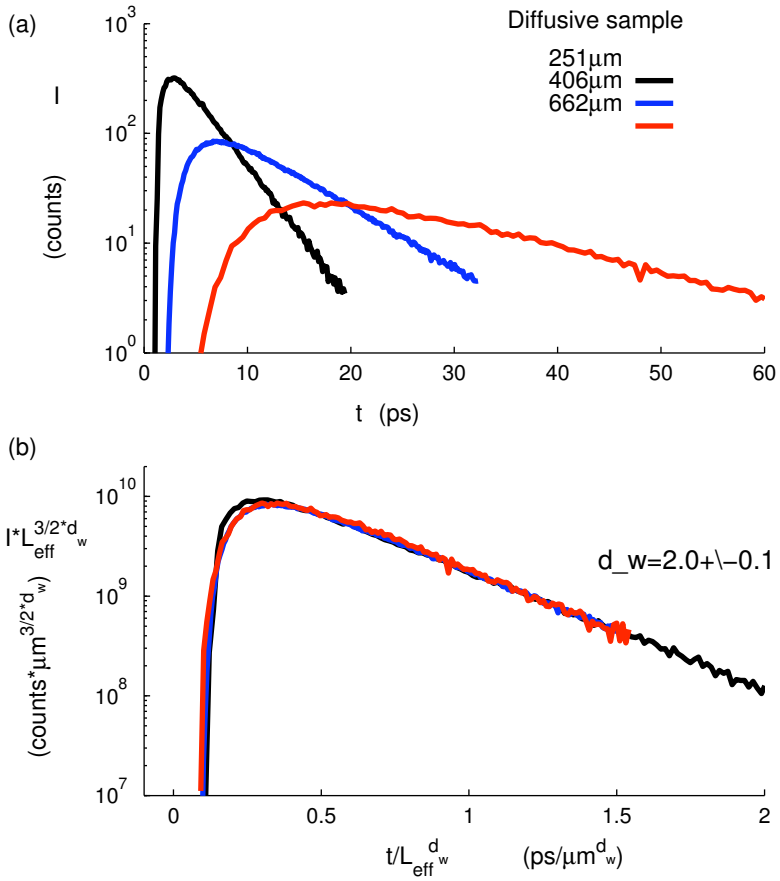

Figure 4.9 – Data collapse for reference diffusive samples. (a) Unscaled measurements for three sample thickness averaged ; (b) Scaled measurements using the effective sample thickness and the asymptotic walk dimension d_w.

erogeneity. For an homogeneous distribution of scatteres the transport is diffusive. Instead, distributing the scatterers with a fractal-like heterogeneity has a drastic effect on transport, which becomes superdiffusive. Dynamic signatures of superdiffusive dynamics as the ones showed in this work have never been observed before.

The step further would be a better understanding of the stochastic process underlying the transport. Although we perfectly know all the components of a Lévy glass, deriving the step-length distribution for light in a sample is a complicate issue. The first attempt is to apply the chord-length model, as we have done in Section 4.1.2. The values of α obtained from eq. 4.5 are not far from the measured walk dimensions. In particular for $\beta = 2.0$ the chord-length model gives $\alpha = 0.7$. According to [76] and [71] the corresponding walk dimension should be $d_w = 1$. This prediction is summarized in eq. 2.26 and eq. 2.36. On the other hand the Generalized Ohm's

law predicts that for $\alpha < 1$ the scaling exponent of the intensity axis must be smaller than one. However the good collapse of the experimental curves suggests that we can satisfy both the scaling laws, for time and intensity, using one exponent. Moreover to accept that these samples have $\alpha = 0.7$ we should prefer the pre-asymptotic d'_w to the asymptotic d_w, since the former is closer to the expected values.

We have discussed this inconsistency to make the reader aware of the limits of the chord-length model. It is important to stress that this model does not consider the following point:

- the steps performed inside the spheres are only a portion of the total steps. A real Lévy glass has a spheres filling fraction of 71%, thus the embedding diffusive medium is 29% of the entire sample. The steps performed between the spheres needs to be taken into account;

- after each sphere crossing the probability to directly pass into another spheres is not negligible. Multicrossing can play an important role if the transport mean free path l'_t between spheres is bigger than the average interspheres distance;

The value of the transport mean free path between the spheres plays a prominent role in deciding the abundance of the interspheres steps and of multicrossing. Its measurement is crucial for adopting more realistic model to describe the transport. Our experiment provides an indirect measure of l'_t. Indeed the amount of nanoparticles dispersed in the scattering medium of Lévy glasses is equal to the amount used for the reference samples. The polymer is instead 29% of the polymer used for the reference samples. Assuming that the scatterers are still homogeneously distributed among the spheres at such increased density we can calculate $l'_t = 0.29 l_t = 0.29 * 42 = 12.18 \mu$m.

Another aspect to consider is that the disorder in a Lévy glass is *quenched*, that is "frozen". A quenched environment can generate anti-correlation effects, such as multicrossing of the same sphere. The role of quenching in a Lévy glass-like systems has been investigated in 2D in [103] [108]. Insights on the role played in the transport by the above mentioned effects can be found in Chapter 5.

CHAPTER 5

Light transport in heterogeneous disordered media

The complexity of transport in Lévy glasses has motivated an analytical and numerical investigation on the effects determined by a generic heterogeneity in the scatterers distribution. We have focused the interest on important characteristics such as diffusion constants, average step lengths, crossing statistics and void spacings, which we show, can be analytically predicted. The theory is validated using Monte Carlo simulations of light transport in heterogeneous systems in the form of random sphere packings. We also investigate the differences between unbounded and bounded systems, discussing the role of step correlations.

Besides the general relevance on the obtained results for the optics of heterogeneous systems, this work provides important insights on the transport statistics in Lévy glass-like systems. In particular we present transport simulations in 3D sphere packings, bounded and unbounded, where the diameters of spheres are power-law distributed. We also introduce a quasi-annealed model in alternative to computational expensive sphere packings. Such model mimics the fractal-like heterogeneity of a Lévy glass by using coupled step-length probability disitributions.

The material of this chapter is based on the work published in [2].

5.1 Holey random walks

Let us start to consider the general case of a random walk in a composite media consisting of arbitrarily shaped non-scattering regions embedded in a turbid medium (a holey system), the void filling fraction being ϕ (cf. fig. 5.1).

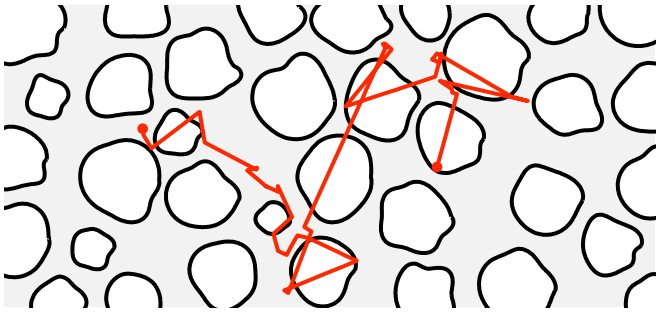

Figure 5.1 – A holey random walk. Random walkers change direction randomly in time, but only when traveling in the turbid medium found in between the non-scattering regions (holes). Transport is governed by the resulting step length distribution and step correlations in a complex manner. From ref. [2]

We will assume that isotropic scatterers are randomly distributed in the turbid medium, meaning that the distance between isotropic scattering events is exponentially distributed with a scattering mean free path ℓ_s. The scattering mean free path is related to single scattering properties via

$$\ell_s = \frac{1}{n\sigma_s} \tag{5.1}$$

where n denotes the number density of scatterers and σ_s the scattering cross section. In general, the random step length S between two subsequent scattering events in the composite heterogeneous medium consists of two parts: a length $S_{\text{turbid}} \in \text{Exp}(\ell_s)$ inside the turbid inter-void medium, and a length S_{void} inside non-scattering void(s):

$$S = S_{\text{turbid}} + S_{\text{void}}. \tag{5.2}$$

Here, it should be noted that S_{turbid} and S_{void} are not independent random variables. On the contrary, they are positively correlated: a long step in the turbid medium is more likely to be accompanied by one or several crossings of non-scattering regions.

Equilibrium considerations

Assuming that the density of states is homogenous (which in optics corresponds to a constant refractive index), random walkers at equilibrium should sample the two constituents according to their respective volume fraction.

We then expect that a fraction ϕ of the average step is located to voids, i.e.

$$E[S_{\text{void}}] = \phi E[S] \tag{5.3}$$
$$E[S_{\text{turbid}}] = (1-\phi)E[S] \tag{5.4}$$

In terms of expectations values, we have

$$E[S] = E[S_{\text{void}}] + E[S_{\text{turbid}}], \tag{5.5}$$

and using that we per definition also know that $E[S_{\text{turbid}}] = \ell_s$, we reach $E[S] = \phi E[S] + \ell_s$ and conclude that

$$E[S] = \frac{\ell_s}{1-\phi} = \ell_h \tag{5.6}$$

This important result that tells us two things: the mean step length is independent of the shape and size distribution of the non-scattering regions, and it equals the homogenized scattering mean free path ℓ_h that would govern a system where the scatterers were randomly distributed over the full volume instead of only a volume fraction $1-\phi$ (n going from n_0 to $n_0(1-\phi)$ in eq. 5.1). $E[S]$ is thus dependent only on ϕ, not on the sizes of the voids. This means that the mean step will only grow with an increase of ϕ, and not with the inclusion of larger and larger voids.

Although the mean step is a very important quantity, transport properties are determined by the step length distribution as a whole. In particular, when steps can be considered independent, the diffusion constant that governs the macroscopic spreading of random walkers is determined by the ratio of the first two moments of the step distribution (when finite). We have derived the dependence of the diffusion constant on the step distribution moments in Section 1.4.1(eq. 1.36). We also underlined that the common expression for the diffusion constant $D = \frac{1}{3}v\ell_t$ follows as consequence of a exponential step-length distribution.

For a general holey system, with heterogeneous distribution of scatterers, steps are not exponential distributed and the simple formula $D = \frac{1}{3}v\ell_t$ does not hold. Interestingly, we have already shown that the mean step length, $E[S]$, of the holey system is independent of the scatterer distribution. The second moment, $E[S^2]$, will on the other hand depend on the particular heterogeneity and scatterer density in a complex manner.

5.1.1 Sphere packings as holey systems

As indicated above, transport in a general holey system is complicated. Beside the issue of step length distribution, step correlations may be important and must not be forgotten. To gain insight on this complicated matter we will turn to systems where the non-scattering part of the system have the form of a polydispersive random sphere packing. In this and the following section, we will present an analytical theory of transport in such systems.

In subsequent sections, this theory will be compared to Monte Carlo simulations of random walks in sphere packing realizations.

Let r_i $(i = 1, \ldots, M)$ denote the different radii of the involved spheres, and n_i their respective number density. A random walker traveling in this system will scatter randomly in time, but only when being outside of the non-scattering regions. When being scattered, the chance of crossing at least one sphere in the coming step depends on the probability that the next step is longer than the distance to the next sphere surface (along the new walker direction). This distance can be seen as a random variable, and is here denoted Δ_{ps} (ps as in point-sphere). If a sphere is crossed, the probability to cross also a second sphere before being scattered now depends on the sphere-sphere spacing along the direction of the walker. Also this distance is a random variable, and we denote it Δ_{ss} (ss as in sphere-sphere). The actual step length distribution will be determined by the distributions of these random variables (of course, in combination with the inter-sphere scattering mean free path ℓ_s). Figure 5.2 illustrates the definition of these two essential distance variables.

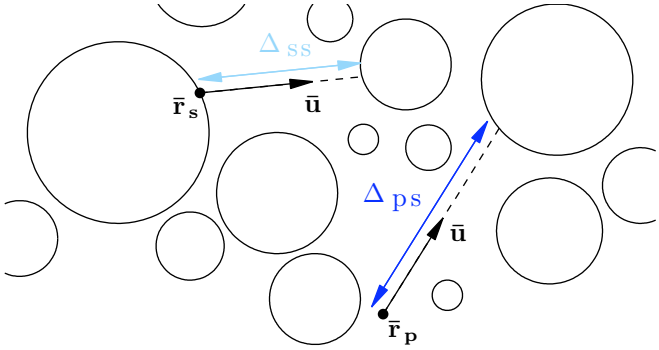

Figure 5.2 – From a random walk perspective, two central characteristics of the sphere packing are the distribution of (i) the distance from a random point $\bar{\mathbf{r}}_\mathbf{p}$ (scattering event) along a random direction $\bar{\mathbf{u}}$ to a sphere surface, $\Delta_{\text{ps}}(\bar{\mathbf{r}}_\mathbf{p}, \bar{\mathbf{u}})$, and (ii) distance to the next sphere along a random direction when leaving a sphere at a random point $\bar{\mathbf{r}}_\mathbf{s}$, $\Delta_{\text{ss}}(\bar{\mathbf{r}}_\mathbf{s}, \bar{\mathbf{u}})$. Their distributions can be assessed via statistical analysis of sphere packings. Later, we show that the mean value of Δ_{ss}, as experienced by the random walker, can be analytically predicted. From ref. [2]

The average spacing between spheres Δ_{ss}, as experienced by the random walker, can be analytically calculated from the filling fraction and the sphere distribution. If we consider a random line drawn through the sphere packing, it is evident that a fraction $1 - \phi$ of it will be drawn through the intersphere medium. Letting $E[\zeta]$ denote the average length of the individual chords through the spheres, we have that

$$\frac{E[\Delta_{\text{ss}}]}{E[\Delta_{\text{ss}}] + E[\zeta]} = 1 - \phi \tag{5.7}$$

and, similarly to Olson et al. [109], conclude that

$$E[\Delta_{\mathrm{ss}}] = \frac{1-\phi}{\phi} E[\zeta]. \tag{5.8}$$

The average chord length $E[\zeta]$ can, in turn, be calculated from the sphere distribution. Let p_i denote the probability that a random chord is made in a sphere of radius r_i. Intuitively, this probability should be proportional to the total surface area of the sphere category, i.e.

$$p_i = \frac{A_i}{\sum_j A_j} = \frac{n_i \times r_i^2}{\sum_j n_j \times r_j^2} \tag{5.9}$$

In fact, this view is equivalent to the equilibrium argument adhered to in this article: the total path made through the different sphere categories should equal their fraction of the total volume. Assuming an isotropic flux of random walkers close to the sphere surfaces (see discussion in [110]), the length of a chord through a sphere of radius r_i follows a triangular probability density function $f_i(x) = x/(2r_i^2)$ in $0 \leq x \leq 2r_i$. The average chord being $\ell_i = 4r_i/3$ and the mean square chord being $2r_i^2$. The probability density function of a random chord ζ in the polydispersive packing, $f_\zeta(x)$, is a weighted sum of the individual chord distributions f_i:

$$f_\zeta(x) = \sum_i p_i \times f_i(x) = \sum_{i:2r_i>x} p_i \times \frac{x}{2r_i^2}. \tag{5.10}$$

The mean overall chord then becomes

$$E[\zeta] = \sum p_i \ell_i = \sum p_i \times \frac{4r_i}{3}, \tag{5.11}$$

and its mean square

$$E[\zeta^2] = \sum p_i \times 2r_i^2. \tag{5.12}$$

5.1.2 The exponential spacing model

From statistical analysis of random sphere packings, we generally find that $E[\Delta_{\mathrm{ps}}] \approx E[\Delta_{\mathrm{ss}}]$ and that distributions have near-exponential decay. We therefore propose a model in which the actual (complicated) distributions of Δ_{ps} and Δ_{ss} are modeled with a *single* exponentially distributed random spacing Δ with mean spacing $\bar{\Delta}$, i.e. $\Delta \in \mathrm{Exp}(\bar{\Delta})$. In fact, it has been shown that spacing between random objects is, to a very good approximation, exponential at low filling fractions [109]. At higher filling fractions, spacing distributions are no longer be perfectly exponential, but rather a complicated function of the exact structure [109,111,112]. But also in such cases, we will show that the errors due to the use of a simple exponential spacing model can be reasonably small.

Within the exponential spacing model, the probability that an exponentially distributed step $S_{\text{turbid}} \in \text{Exp}(s)$ will not take the random walker to a sphere is

$$P_0 = P(S_{\text{turbid}} < \Delta) = \frac{\bar{\Delta}}{\bar{\Delta} + \ell_s}. \tag{5.13}$$

Given the memoryless property of the Poisson process that governs scattering events, the number of crossings naturally follows a geometric distribution. This means that the probability to cross n spheres in between two scattering events is

$$P_n = (1 - P_0)^n P_0. \tag{5.14}$$

The average number of sphere crossings per step N is, within this model,

$$E[N] = \sum n \times P_n = \frac{1 - P_0}{P_0} = \frac{\ell_s}{\bar{\Delta}}. \tag{5.15}$$

In order to fulfill the equilibrium condition, $\bar{\Delta}$ must be chosen so that the average step samples the medium according to volume fractions. Assuming that the number of sphere crossings and involved chord lengths are independent, we should have that

$$\frac{E[N]E[\zeta]}{E[N]E[\zeta] + \ell_s} = \phi. \tag{5.16}$$

Using eq. 5.15, we then reach the conclusion that

$$\bar{\Delta} = E[\Delta_{\text{ss}}] = \frac{1 - \phi}{\phi} E[\zeta]. \tag{5.17}$$

The exponential spacing model we have now outlined allows us to the estimate step length distribution. In particular, we can use it to estimate the mean squared step $E[S^2]$. Again, we will assume that, for each step, the involved chord lengths are independent of the number of sphere crossings. By splitting the outcome of S^2 into the number of crossings and summing the conditional expectations we find that

$$\begin{aligned} E[S^2] &= E[S^2_{\text{turbid}}] + E[S^2_{\text{void}}] + 2E[S_{\text{turbid}} S_{\text{void}}] \\ &= 2\ell_s^2 \\ &\quad + \sum_{n=0}^{\infty} P_n \times (nE[\zeta^2] + n(n-1)E[\zeta]^2) \\ &\quad + 2\sum_{i=0}^{\infty} P_n \times nE[\zeta] \times (n+1)\frac{\bar{\Delta}\ell_s}{\bar{\Delta} + \ell_s} \\ &= 2\ell_h^2 + \phi\ell_h \times \frac{E[\zeta^2]}{E[\zeta]}. \end{aligned} \tag{5.18}$$

5.1.3 The diffusion constant for holey system

Assuming that step correlations are negligible, and remembering that $E[S] = \ell_h$, the expression for $E[S^2]$ given above (eq. 5.18) allows us to write a closed form expression for the diffusion constant that governs macroscopic transport. Introducing the homogenized diffusion constant

$$D_h = \frac{1}{3} v \ell_h, \tag{5.19}$$

and the "chord-domain" diffusion constant (the diffusion constant for a random walk with steps purely following the chord step distribution)

$$D_\zeta = \frac{1}{6} v \times \frac{E[\zeta^2]}{E[\zeta]}, \tag{5.20}$$

we reach, via eq. 1.36, the surprisingly simple relation

$$D = D_h + \phi D_\zeta. \tag{5.21}$$

Interestingly, the diffusion constant of the heterogeneous system is given by the homogenized diffusion constant plus a term which is independent of the inter-void scattering mean free path ℓ_s. Note also that, as expected, the expression reduces to the homogenized diffusion constant as ϕ approaches zero.

5.2 Monte Carlo simulations of transport in quenched disorder

To illustrate the validity and importance of the theory presented in earlier sections, this section will compare it with Monte Carlo (MC) simulations of transport in quenched random sphere packings. We use the term *quenched* to emphasize that the random walk is done in the quenched (frozen) heterogeneity of a random sphere packing, and not in fully annealed disorder model. The sphere packings used in our simulations are created by random sequential addition of spheres [113] in descending order of size. Moreover, they are created to have periodic boundary conditions, i.e. so that the complete (cubic) sphere packing can act as a unit cell that can be stacked in all directions. As illustrated in fig. 5.3, random walks are performed so that when crossing a boundary of the unit cell, the random walk can be continue on the opposite side of the same unit cell (while keeping track of unit cell coordinates). The use of periodic boundary conditions in this manner allows us to use realistic sizes of sphere packings, and still being able to track walkers for long times and average dynamics over local disorder realization in an efficient way. Still, the size of the unit cell is made large enough to render effects of periodicity negligible (sizes of utilized sphere packings are carefully stated). We base our investigations on equilibrium starting conditions, i.e. allowing walkers to start randomly over the whole unit cell (including the

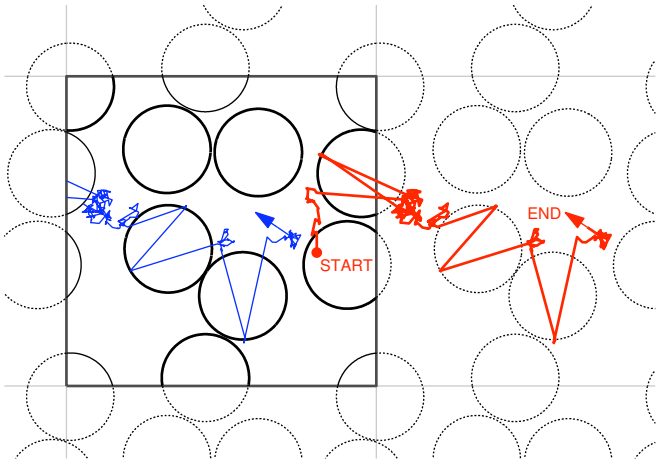

Figure 5.3 – 2D illustration of unbounded holey random walks based on a sphere packings with periodic boundary conditions. When a walker leaves the sphere packing unit cell (marked square), the walk continues on the opposite side of the same sphere packing. The path of interest (red) is reconstructed by keeping track of boundary crossings, but path outside the unit cell is in reality a path inside the one and only unit cell (blue path). The use of periodic boundary conditions in this manner enables the use of realistically sized sphere packings, efficient averaging over disorder realization by allowing walkers to start also close to the sphere packing boundaries, and long-time tracking of spreading. At the same time, the size of the unit cell is made large enough to make effects of periodicity negligible. From ref. [2]

interior of the non-scattering regions). For step statistics, only full steps between scattering events are considered. To be on the optical time scale, walkers are set to travel at the speed of $v = 200$ μm/ps (corresponding to a refractive index of 1.5).

5.2.1 A strongly polydisperse sphere packing

Consider a polydispersive sphere packing, i.e. a situation where the non-scattering regions vary in size. We will study the limiting case of a system with fractal heterogeneity (over two orders of magnitude) and a high sphere filling fraction. More specifically, our sphere packing is based on $M = 18$ sphere categories where the radii r_i are exponentially sampled from $r_{\min} = 2.5$ μm up to $r_{\max} = 200$ μm, i.e.

$$r_i = r_{\min} \times \exp\left(\log\left(\frac{r_{\max}}{r_{\min}}\right) \times \frac{i-1}{M-1}\right). \tag{5.22}$$

The number density of the spheres is set proportional to $1/r_i^3$ (i.e. the different sphere categories all occupy the same volume fraction), and the filling fraction of the system as a whole is $\phi = 0.7005$ (9507676 spheres in a cube with a side of about 2 mm).

Figure 5.4 highlights the success of the exponential spacing model also for such a complex heterogeneous system. In particular, this means that we have good quantitative knowledge on the step length distribution (including the sphere crossing statistics).

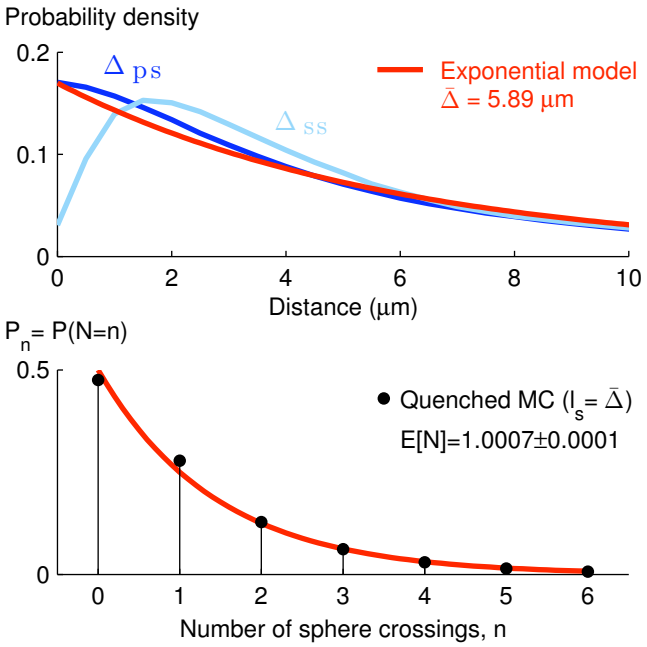

Figure 5.4 – The theoretical predictions of the exponential spacing model is in good agreement with both quenched simulations and statistical analysis of a strongly polydispersive sphere packing. The success is here illustrated for the case of a fractal sphere packing with $M = 18$ radius categories ranging from $r_{\min} = 2.5$ μm to $r_{\max} = 200$ μm (9507676 spheres in a cube with a side of about 2 mm, $\phi = 0.7005$). As shown in the top graph, the analytically predicted mean spacing of $\bar{\Delta} = 5.89$ μm is in good agreement with spacing distributions obtained via statistical analysis of the sphere packing ($E[\Delta_{\text{ps}}] \approx E[\Delta_{\text{ss}}] \approx 6$ μm). The bottom graph highlights that the crossing probabilities P_n predicted by the exponential spacing model (eq. 5.14) agree almost perfectly with simulations running at $\ell_s = \bar{\Delta}$. In particular, setting $\ell_s = \bar{\Delta}$ (as done in this simulation) clearly renders $E[N] = 1$. The mean and mean squared steps are also in good agreement with theory. Theory predicts $E[S] = \ell_h = 19.669$ μm and $E[S^2] = 1776.7$ μm^2, and simulations gave 19.679 ± 0.004 μm and 1692 ± 1 μm^2, respectively (mean ± standard error). That the observed mean squared step is a few percent lower than the theoretical prediction is consistent with the fact that the exponential model slightly overestimates the number of higher order multi-crossings ($n \geq 3$). This, in turn, can be understood by looking in the upper graph and noting that the sphere-sphere spacing distance often will be underestimated by the exponential spacing model. From ref. [2]

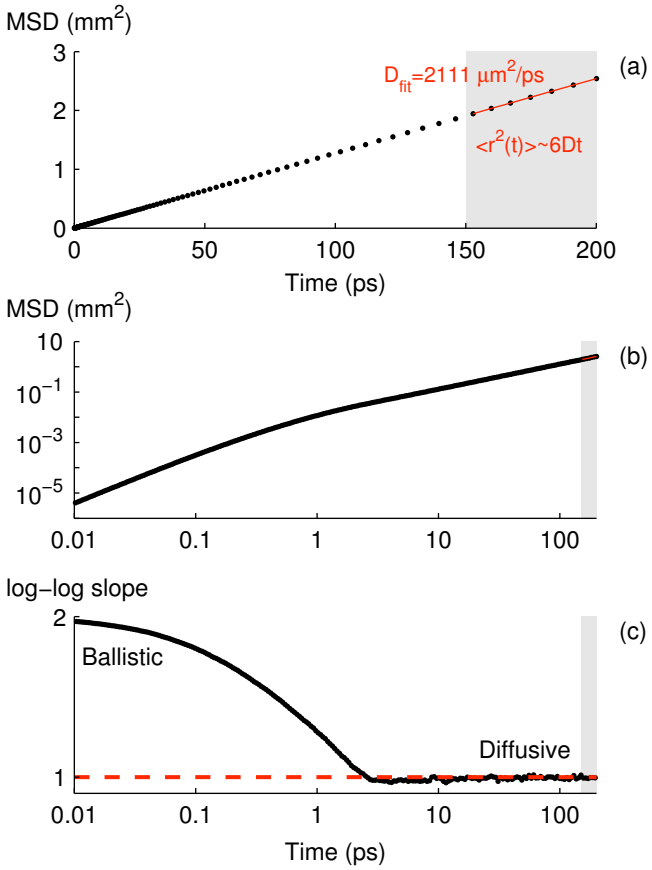

Figure 5.5 – Transport dynamics for a holey system based on a fractal sphere packing (sphere radii ranging from 2.5 μm to 200 μm, each category occupying about 4% of the volume, the overall sphere filling fraction being $\phi = 0.7005$). Here, the walker crosses on average one sphere in-between scattering events ($\ell_s = \bar{\Delta} = 5.89$ μm). The exact $E[S^2]$ as obtained from simulations would, if steps were independent, result in a diffusion constant of 2866 μm^2/ps (step data presented in fig. 5.4, but note that exponential spacing model in this particular case overestimates the $E[S^2]/E[S]$ ratio by about 5%). In contrast, a linear fit over the temporal range indicated in gray in part (a) gives $D = 2111 \pm 7$ μm^2/ps (mean ± standard error of the mean, as obtained from five simulation repetitions with 10^5 random walkers each). That the observed D is about 25% lower is clear evidence that step correlations play an important role. From ref. [2]

Using $\ell_s = \bar{\Delta}$ as a first test case, fig. 5.5 shows the onset of diffusion and the asymptotic diffusion constant. Interestingly, the asymptotic diffusion constant is in this case about 25% lower than what we would have if steps were independent. With decreasing scattering strength, the importance of step correlations steadily decrease, and the diffusion constant becomes in good agreement with our analytical expression $D = D_h + \phi D_\zeta$. This behavior is illustrated in fig. 5.6, which shows simulations for ℓ_s being 1 to 8 times $\bar{\Delta}$. In this context, we want to emphasize that step correlations *per se* do

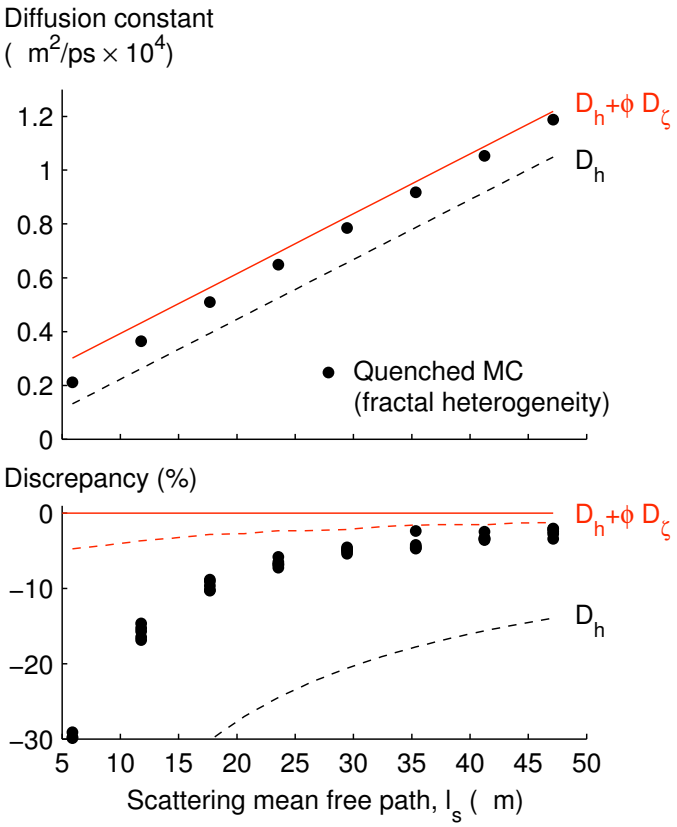

Figure 5.6 – Also for strongly polydispersive systems, our probabilitisic theory is successful. The role of step correlations is, however, a complicated matter. In our particular fractal system, where 400 µm diameter spheres are the largest non-scattering regions, the role of correlation becomes small when ℓ_s is a few times larger than the mean void spacing $\bar{\Delta}$. At $\ell_s = 4\bar{\Delta} \approx 24$ µm, the asymptotic D obtained from MSD evolution is then only 4% lower than what the step statistics from quenched simulations tells us. The mean step $E[S] = \ell_h$ is then about 80 µm, a length which apparently is large enough to render step anti-correlation related to crossing of large spheres relatively small. Here, it should be noted that the exponential spacing model overestimates $E[S^2]$ by a few percent (cf. discussion in fig. 5.4). The exact diffusion constant we would see if steps were independent can be estimated from the steps statistics of simulations (via eq. 1.36 in Section 1.4.1), and is in this graph indicated by the dashed red line. Although the errors caused by our model ($D_h + \phi D_\zeta$) is only a few percent, it is still important to realize that step correlation are negligible when the actual diffusion constants (solid dots) meet the dashed line. From ref. [2]

not affect the applicability of the exponential spacing model and the accuracy of the related $E[S^2]$ estimation (eq. 5.18). Instead, they only affect the validity of the assumption of independent steps that leads to $D = D_h + \phi D_\zeta$ (eq. 5.21).

5.3 Finite size fractal sphere packings: ideal Lévy glasses

So far, we have investigated unbounded holey systems. In practice, one often deals with finite size system where transport can be even more complicated to understand. For homogenous media it is, for example, well known that the transport in slabs deviates from diffusion when sample thickness L is less than about 10 times the transport mean free path [40, 84, 114]. For heterogeneous systems, additional complications arise when the sizes of non-scattering regions are on the order of the sample size. Here we aim at discussing the relation between transport in unbounded media, as treated in previous previously, and transport in finite size media. We will show that the theory of diffusion constants is not directly applicable to bounded systems when the size of heterogeneities is on the order of system dimensions.

This issue of bounded heterogeneous systems is particularly relevant to the ongoing discussion on anomalous transport in Lévy Glass [1,101–103,105, 107,108]. A detailed introduction to Lévy glasses can be found in Chapter 4. Lévy Glasses are turbid materials with strong (fractal) spatial heterogeneity in the density of scatterers. The heterogeneity is engineered and controlled by the embedding non-scattering regions that follow a power law size distribution into a turbid medium. In an ideal Lévy glasses the non-scattering regions are constituted by glass spheres of sizes exponentially sampled from some smallest radius $r_{\min}$ to an upper radius $r_{\max}$. Assuming one sphere crossing per step and a negligible contribution from the inter-sphere media, setting the number density of spheres $n \sim r^{-(\alpha+2)}$ should produce a step length distribution that fall off as $\ell^{-(\alpha+1)}$ [101]. On scales on the order of the maximal sphere size, as in slabs of thickness $L = 2r_{\max}$, the transport is then believed to be close to that of a Lévy walk. Although the probabilistic theory presented here represents a significant contribution to the topic of Lévy Glass design, this falls outside the main focus of this article. A view on this specific but important matter is, nonetheless, given in Section 5.4. Here, we will instead stick to the more general question of the relation between transport in unbounded and bounded media.

The system studied in the previous section is, in fact, an unbounded Lévy Glass with $\alpha = 1$. Its composition closely resembles the Lévy Glass systems that have been studied experimentally [1,102] and simulation-wise [108]. Our study has shown that step correlations play an important role for transport in the unbounded systems, and that the resulting diffusion constant for the system was about 2111 $\mu m^2/ps$. Looking back at fig. 5.5 and the evolution of the mean square displacement (MSD), it appears that the onset of diffusion occurs surprisingly early. The MSD starts to grow approximately linear with time already after 2 ps. At this time, the MSD is about 0.027 mm^2, meaning that the average walker displacement is (roughly) on the order of 150 μm. From this, it may be tempting to conclude that transport is diffusive after some 150 μm, and that the transmission through a Lévy Glass of thickness

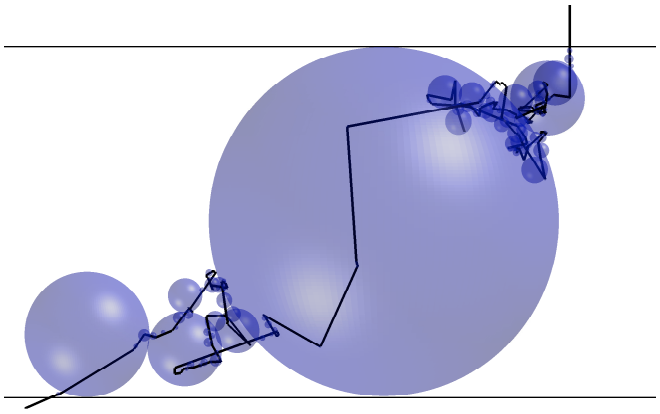

Figure 5.7 – 2D projection of a simulated trajectory through a 3D Lévy Glass slab. In this case, the random walker crossed one of the largest spheres. To obtained average transmission properties, walkers are injected randomly on top of the slab (the slab consists of 9507676 spheres, the thickness being $L = 2r_{\max} + \epsilon = 402$ µm, $\phi = 0.7005$). Analysis of the sphere packing reveals that the exponential spacing model applies equally well as in the unbounded case, and that $\ell_s = \bar{\Delta} = 5.89$ µm indeed renders $E[N]$ very close to one. From ref. [2]

$L = 2r_{\max} = 400$ µm indeed will be diffusive. In fact, Groth et al. [108] have claimed that transport through Lévy Glass follows regular diffusion. To check whether the above reasoning is adequate or not, and to investigate the claim of Groth et al., we have performed simulations of the transport through a bounded version of this sphere packing.

Figure 5.7 illustrates our simulations of transport through bounded systems. Our conclusion from these simulations is that transport through Lévy Glass cannot be described by diffusion. Along with a significant amount of ballistic and quasi-ballistic transmission, we observe major deviations from diffusion theory also in mean transmission time and long-time decay constant (lifetime). Diffusion theory of light transport is well established, and in the diffusive regime it is, for example, well known [85] that the mean transmission time $\bar{t}_D$ follows

$$\bar{t}_D = \frac{(L + 2z_e)^2}{6D}, \tag{5.23}$$

and that the decay time constant τ_D is given by

$$\tau_D = \frac{(L + 2z_e)^2}{\pi^2 D}. \tag{5.24}$$

In the above formulas, L denotes slab thickness, and $z_e = \frac{2}{3}\ell_t$ the so called extrapolation length. If transport through the slab is diffusive with $D = 2111$ µm^2/ps, macroscopic transport should be identical to a random walk of independent and exponential distributed steps with average length $\ell_t =$

$3D/v \approx 31.7$ µm. We would thus expected a mean transmission time of about $\bar{t}_D = 15.6$ ps and a decay constant of about $\tau_D = 9.5$ ps. In contrast, as shown in fig. 5.8, quenched simulations result in a mean transmission time of 17.4 ps and decay constant of 12.5 ps. In fact, the observed combination of $\bar{t}$ and τ is in fact not consistent with any diffusion constant. Furthermore, the significant amount of ballistic and quasi-ballistic light alone indicates that diffusion cannot well capture the transport. We therefore conclude that transport in Lévy Glass is not governed by diffusion. Instead, we found that the dynamics is well reproduced by, what we call, a quasi-annealed simulation in which we mimic the step distribution but effectively remove step anti-correlations. In this straight-forward simulation, being a numerical correspondent to our probabilistic theory, steps are generated on the basis of the exponential spacing model under the requirement that when the walker is about to a make a chord, this chord cannot be longer than the distance to the slab boundary. The step length is thus position and direction dependent, but step correlations are heavily suppressed.

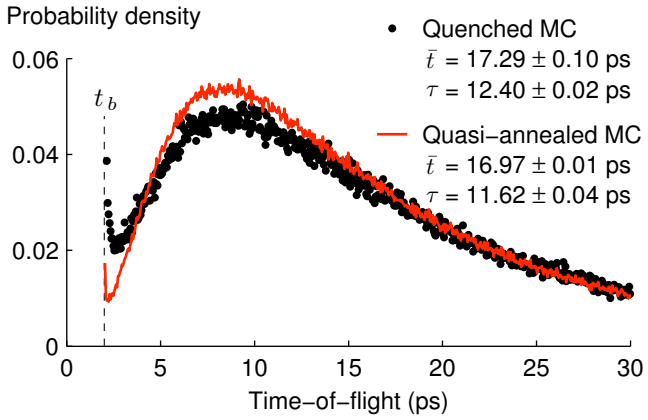

Figure 5.8 – Transmission dynamics for a Lévy Glass, i.e. a bounded fractal sphere packing (slab thickness $L = 402$ µm, maximal sphere diameter 400 µm). Important characteristics such as mean transmission time $\bar{t}$ and decay constant τ show that the dynamics is not consistent with diffusion (see main text). This conclusion is also supported by the significant amount of quasi-ballistic transmission (truly ballistic component at $t_b = L/v$ is not part of the shown distribution). The dynamics is instead well reproduced by a quasi-annealed simulation based on the exponential spacing model. This mutual agreement indicates that step correlations play a less important role here than in the unbounded case. Statistics are based on 3 and 10 repetitions of 10^6 walkers for the quenched and quasi-annealed simulations, respectively (mean times and decay constant are stated in the graph as the mean ± standard error). The transmission were in both cases about 12%, while the the ballistic fraction of the transmission was 0.6% and 0.15% (higher in the quenched case). From ref. [2]

5.3.1 The quasi-annealed model

The proposed quasi-annealed random walk aims at mimicking the step length distribution of the quenched system while removing step correlations related to the quenched disorder. After random walker initiation, and after each scattering event, a random step $S_{\text{turbid}} \in \text{Exp}(\ell_s)$ to be travelled through the turbid component is generated. The length of this step is first compared to the distance to the boundary, Δ_b, along the current direction of propagation. If $S_{\text{turbid}} > \Delta_b$, the walker leaves the sample and a transmission or reflection time is registered. If, on the other hand, $S_{\text{turbid}} < \Delta_b$, S_{turbid} is instead compared to a randomly generated exponential distributed distance to the "closest virtual sphere", $\Delta_s \in \text{Exp}(\bar{\Delta})$ (cf. the exponential spacing model described in Section 5.1.2). If $S_{\text{turbid}} < \Delta_s$, scattering will take place, and the procedure will start over when a new direction and a new step S_{turbid} have been generated. If $S_{\text{turbid}} > \Delta_s$, the walker will cross a non-scattering region, after which the remaining part of the step $S_{\text{turbid}} - \Delta_s$ will be used as the new step forward (to be compared with the updated Δ_b and a new sphere spacing). The length travelled through the void (a random chord ζ) is generated based on the distribution of chords predicted by equilibrium considerations, i.e. the density function given in eq. 5.10. The related cumulative distribution functions (CDF) is

$$F_\zeta(x) = P(\zeta \leq x) = 1 - P(\zeta > x) \tag{5.25}$$

$$= 1 - \sum_{i:2r_i>x} \int_x^{2r_i} p_i \times \frac{x}{2r_i^2}\, dx \tag{5.26}$$

$$= 1 - \sum_{i:2r_i>x} p_i \times \left(1 - \frac{x^2}{4r_i^2}\right) \tag{5.27}$$

$$= 1 - \sum_{i:2r_i>x} p_i + \sum_{i:2r_i>x} p_i \times \frac{x^2}{4r_i^2}. \tag{5.28}$$

Solving $y = F_\zeta(x)$, we find

$$x = F_\zeta^{-1}(y) = \sqrt{\frac{y - 1 + \sum\limits_{i:F(2r_i)>y} p_i}{\sum\limits_{i:F(2r_i)>y} \frac{p_i}{4r_i^2}}}. \tag{5.29}$$

We use this inverse CDF to generate the random chord length ζ, setting

$$\zeta = F_\zeta^{-1}(U), \tag{5.30}$$

where U is a random variable uniformly distributed in $[0, 1]$. Note that a generated chord is only accepted if it is smaller than the current distance to the boundary. If a generated chord is larger than the distance to the boundary it is discarded, and the generation is remade. This means that

long steps to some extent are under-represented compared to the equilibrium consideration that lies behind the chord length distribution. At this stage, it cannot be ruled out that this has some impact on quantities such as mean transit time and decay rate (lifetime). The role of step correlations in transport through quenched disorder certainly deserves further attention in the future.

5.4 Lévy glass design

When Lévy Glass were introduced by Barthelemy et al. [1], the scatterer concentration was selected aiming at achieving, on average, one scattering event between sphere crossings (i.e. $E[N] = 1$, where N states the number of sphere crossings in a step). The design principle was not elaborated in more detail, and exactly how filling fraction and scattering strength affect crossings statistics was not known. The inter-sphere transport mean free path was in fact chosen to match the smallest sphere diameter, i.e. $\ell_t = 2r_{\min} = 5$ µm. The probabilistic theory presented in this work allows a selection of the scattering strength that more strictly fulfills the ideal Lévy Glass design criteria. From eq. 5.15, we see that $E[N] = 1$ is reached when $\ell_s = \bar{\Delta}$. As can be seen in fig. 5.4, this result is confirmed by our simulations. In this respect (using eq. 5.17 to express $\bar{\Delta}$), the ideal scattering strength is therefore

$$\ell_s^{\text{ideal}} = \bar{\Delta} = \frac{1-\phi}{\phi} \times E[\zeta]. \tag{5.31}$$

Returning to the experimental work in Ref. [1], the filling fraction, as can be calculated from recipe given in the supplemental information, was about 67%. Via calculation of the mean chord, we find that the ideal ℓ_s for the samples used to investigate transmission scaling ranges from 9.5 µm ($L =$ 550 µm, $L = 2r_{\max}$ being the Lévy Glass slab thickness) to 4.2 µm ($L =$ 50 µm). Although the utilized scattering strength clearly is on the right order of magnitude, setting $\ell_s = 2r_{\min}$ is not universally ideal. That the ideal ℓ_s varies with Lévy Glass thickness is related to the fact that thicker samples include the use of larger spheres that fill space more efficiently than smaller ones. If the filling fraction ϕ is kept constant, the average sphere spacing will therefore increase with thickness. It is thus important to realize that studies of a series of Lévy Glass with varying $L = 2r_i$ but with constant ϕ and ℓ_s comes with an inherent mismatch with the ideal Lévy Glass design principle. The implication this finding has on the design of scaling experiments remains to be elaborated. For completeness, it should also be noted that scattering is not fully isotropic in the discussed experiments. The titania nanoparticles used gives a anisotropy factor of $g \approx 0.6$, meaning that $\ell_s = (1-g)\ell_t \neq \ell_t$. This is an additional aspect that should be considered in the future.

In a more recent experimental paper, Burresi et al. [102] reported on weak localization of light (coherent backscattering) in Lévy glass. There, samples

had a filling fraction of about 70% and were manufactured using spheres of sizes from $r_{\min} = 2.5$ μm up to $r_{\max} = 115$ μm ($L \approx 230$ μm). Our theory shows that the ideal ℓ_s is around 6.3 μm and 3.8 μm for the studied $\alpha = 1$ and $\alpha = 1.5$ samples, respectively. In the article, reference experiments where scatterers were dispersed homogeneously rendered $\ell_t = 19$ μm, indicating that the inter-sphere scattering strength was $l_t = 19/(1 - \phi) = 5.7$ μm. The experiments done were thus in close agreement with the ideal design principle (again, disregarding that scattering was anisotropic with $g = 0.6$).

Finally, a recent paper by Groth, Akhmerov and Beenakker [108] investigated transmission scaling in Lévy Glasses via simulations of random walks in sphere packings. There, simulations are stated to run with $\ell_s = r_{\min}/2$ and it is said that this choice was made to ensure that "there is, on average, one scattering event between leaving and entering a sphere" (i.e. to ensure $E[N = 1]$). Given the findings of our present work, we believe that this level of scattering is too strong to render $E[N] = 1$ (at least for relevant filling fractions). Above, we reported that experimental Lévy Glass systems have had a filling fraction of about 70%, and that the ideal scattering mean free path always is significantly larger than the radius of the smallest sphere. Assuming that Groth et al. are not studying very different systems, we believe that using $\ell_s = r_{\min}/2$ brings them far from the ideal situation where $E[N] = 1$. However, since utilized filling fractions were not stated, we cannot be fully quantitative. Nonetheless, it is important to note that while setting ℓ_s very small will take us close to the desired $\ell^{-(\alpha+1)}$ power law decay in the step length distribution (multi crossing getting increasing unlikely, i.e. $P(N > 1)$ negligible), such a procedure will induce strong step correlations that affect transport.

CHAPTER 6

Breakdown of similarity relation in disordered thin slabs

It is known, that in optically thin disordered samples, i.e. with a thickness which is few times the transport mean free path, diffusion breaks down at earlier times. Indeed, along this work, we have faced the impossibility to employ diffusion theory to describe the early-time light transmitted from homogeneous disordered samples. This is a consequence of the approximations on which diffusion theory relies. Usually, many of the limits of diffusion theory can be overcame by employing radiative transfer theory, or equivalently, Monte Carlo simulations. However we observed that simulations performed assuming isotropic scattering were not able to completely describe the early-time transmission. We realized, that thanks to the very good stability and temporal resolution of our time-resolved setup (see Chapter 3), our measurements were sensitive to the single scattering anisotropy. In general this possibility is prevented by the *similarity relation* for diffusive transport [115].

The similarity relation states that it should be difficult to infer information on g and on ℓ_s from a multiply scattered light, where ℓ_s is the scattering mean free path and g the anisotropy factor. The macroscopic light transport is essentially governed by $\ell_t = \ell_s/(1-g)$. As a consequence measurements of microscopic properties have been made by studying light transport close to a source or transport through small samples (see, e.g., [116] and references therein).

The possibility to resolve the ambiguity related to the similarity relation by looking at early time-of-flights (TOF) was discussed already in the classic paper of Patterson, Chance and Wilson [5]. In addition, there are several contributions on how g impacts the validity of the diffusion approximation [14, 24, 115, 117], illustrating the intimate link between break in similarity

and diffusion breakdown. Breakdown of diffusion theory has mostly been considered as a complication. In fact, it is often recommended to exclude early times from analysis, partly due to diffusion theory breakdown, partly due to experimental uncertainties in timing [118].

In this chapter we show that it is possible to go beyond that perspective, and that all the mentioned complications can represent an opportunity to infer single scattering properties from multiply scattered light.

Part of this chapter is also published in [4].

6.1 The similarity relation

In radiative transfer, transport is modeled using an absorption coefficient μ_a, a scattering coefficient μ_s and a scattering phase function. The famous transport equation follows from energy conservation [13, 20]. The derivation is phenomenological, reducing the complex wave propagation to a Poissonian random walk with exponentially distributed steps between scattering events, with correlations in directionality given by the phase function (cf. [13] for the relation between Maxwell's equations and radiative transfer). The average step between scattering events is the scattering mean free path, $\ell_s = 1/\mu_s$. On a macroscopic scale (i.e., after many scattering events), the transport equation reduces to a diffusion equation. Assuming homogenous random distribution and orientation of scatterers, the diffusion constant is

$$D = \frac{1}{3} \times \frac{\ell_s}{1-g} \times v_E \tag{6.1}$$

where g is the average cosine of the scattering angle, and v_E the energy velocity [119, 120]. Here we have reached the similarity relation mentioned earlier – as long as the quantity $\ell_t = \ell_s/(1-g)$ is conserved, macroscopic transport is similar. It is thus possible to map a diffusive process onto a random walk of exponentially distributed, isotropic and independent steps of average length ℓ_t. The similarity has also been exploited to, e.g., relax the knowledge required on g (and phase function) when using Monte Carlo simulations (MC) to evaluate time-resolved diffuse spectroscopy [24, 121–125].

6.2 Breakdown of diffusion and of similarity

We have already discussed in Section 1.4.1 that diffusion arise as a consequence of the Central-Limit Theorem (CLT). However in order to converge to diffusion the multiple scattering process needs to reach high order scattering events. Thereby the medium needs to be considerably thicker than the transport mean free path. This is the cause of diffusion breakdown at early time in optically thin slabs. In such condition, indeed, early time light does not undergo enough scattering events to converge to diffusion. For example

Alfano et al. observed that early time light is diffusive when $L/\ell_t > 10$, where L is the thickness of the turbid slab [114].

In fig. 6.1 we show the total time-resolved transmission from a diffusive slab of thickness 406μm and transport mean free path 42μm. The transport mean free path has been evaluated through a fit with diffusion theory at late time, where diffusion holds (see Section 3.5). Due to diffusion breakdown the rising of the curve cannot be fitted by diffusion theory, while the late time transmission is well described by diffusion theory. A better modeling of the data is obtained by using MC simulations, since they directly solve the radiative transfer equation without the approximations assumed by diffusion theory.

The simulation reported in fig. 6.1 has been performed assuming isotropic scattering and steps exponentially distributed around $\ell_t = 42\mu$m. This method of accounting for the anisotropy of the scattering inherently assumes the similarity of transport. At late time the simulation perfectly match the data, confirming the value of the transport mean free path. At early times instead even simulations deviates from the data. This is a clear evidence that in such scattering regime the anisotropy of the scatterers (present in the investigated sample) individually plays a role. Since the anisotropy g cannot be incorporated in ℓ_t the similarity relation breaks down. We will show that this breakdown can be exploit to retrieve precise information on the g-factor, simultaneously measuring the scattering mean free path. We do it using on-axis time-of-flight measurement, where the effect of the anisotropy at early time is more pronounced.

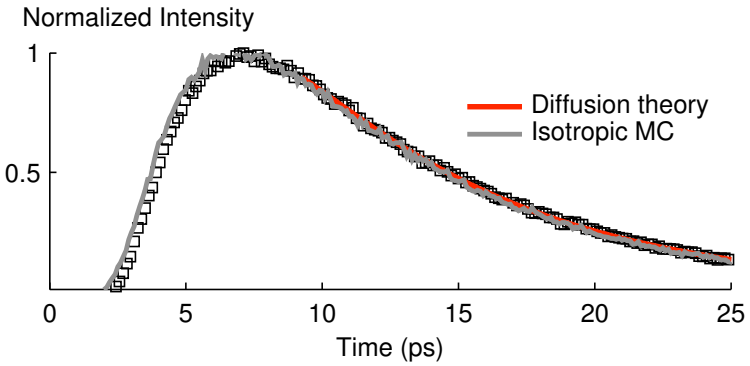

Figure 6.1 – Breakdown of diffusion and breakdown of similarity relation are observable by means of time-of-fligh distribution measurement on optically thin slabs.

6.3 Accelerated Monte Carlo

Many mathematical or numerical techniques have been developed to reduce the time cost of a Monte Carlo (MC) simulation for applications related to

transport [43]. However the key to even faster simulations lie in the move from serial to parallel computing. Considering the basic MC routine described in Section 1.6, it is obvious that the particles does not interact with each other, nor do they change the medium in which they travel, i.e. the traces of individual particles are independent. This independence implies that the particles may be traced in parallel as opposed to serially or simultaneously. Early parallelization of MC code was done using clusters of computers connected over a network [126, 127]. Even if the benefit of such an effort is significant, the effort to write such highly specialized code can be put to better use by writing code for an architecture designed for parallel computations.

In recent years, GPUs have evolved from highly specialized hard-ware to a general purpose parallel computation unit [128, 129]. In [42] GPUs were, for the first time, used to accelerate MC simulations of light propagation in turbid media, resulting in a 1000× speedup over the conventional CPU-based approach. In CPUs, a steady flow of instructions and data must be maintained in order for the processor to be used optimally. This is achieved using caching, branch prediction etc. In GPUs the silicon, and power, is used to achieve high raw computational power and high bandwidth for parallel operations, resulting in significantly higher computational performance as long as all operations can be done in an organized and parallel manner. This is the case for simple radiative transport problems. For more advanced problems, such recording the internal spatial distribution of absorbed energy as done by MCML, utilizing the parallel nature of the GPU becomes more tricky.

In general the features of modern GPUs allow complex simulation problems to be solved several orders of magnitude faster on GPUs compared to modern CPUs. The benefits of using GPU-accelerated Monte Carlo, combined with the very rapid development of new and significantly improved GPUs, suggest that GPU MC will become a standard method in radiative transport MC problems. Since [42] several authors have made contributions to the field and several codes and tools have been made publicly available e.g. [130, 131].

6.4 Simultaneous retrevial of g and D

Accounting for scattering anisotropy in MC simulations is customary done by employing the Henyey-Greestein (HG) phase function [132], which have been introduced to approximate a Mie scattering response. It may be regarded as an approximative average of a polydisperse ensemble of Mie-scatterers where the lobes, caused by interference effects, are cancelled out. The HG phase scattering phase function is

$$p(\cos\theta) = \frac{1}{4\pi}\frac{1-g^2}{(1+g^2-2g\cos\theta)^{3/2}} \tag{6.2}$$

6.4.1 Infering g from time-of-flights distributions

We start with a theoretical view on the possibility to infer g from TOF distributions. Although analytical solutions to the radiative transfer equation are becoming available [21], we will rely on Monte Carlo simulations (MC), see Chapter 1, in particular Section 1.6. As introduced in Section 6.3 by using graphical processing units (GPUs) to parallelize computations [42], simulations are done rapidly. A simulation involving injection of 10^8 random walkers injected into a slab of thickness $L = 8\ell_t$, as done here, takes on the order of 1 s on a modern GPU. Our simulations were conducted on a GPU using the code in [42] modified for a slab geometry (normal incidence). We set absorption to zero and, as customary, used the HG phase function. We start by considering the case of an internal refractive index of n_i=1.5 and an external of n_e=1. The influence of g on TOF distributions for total transmission is shown in Fig. 6.2. The dependence on g is evident, but it is also clear that dynamics fall under similarity at longer times. Systems with strong forward scattering ($g \geq 0.7$) exhibit similar dynamics also for early times, meaning that the similarity relation breaks down when moving towards isotropic scattering (this in agreement with earlier works, cf. [14, 24]). In this case $L/\ell_t = 8$, so diffusion theory can be expected to rather well describe the long-time behavior [40]. The time-integrated transmission was very close to 27.0% for all values of g , in good agreement with the prediction of diffusion theory, $T_D = (\ell_t + z_e)/(L + 2z_e) = 26.6\%$ (z_e being the extrapolation length [25]). Similarly, in terms of the ballistic time t_b, the decay time constant τ varied from $5.70\,t_b$ ($g = 0.9$) to $5.78\,t_b$ ($g = 0.0$), which is in fair agreement with diffusion theory, $\tau_D = (L + 2z_e)^2/(\pi^2 D) = 6.26\,t_b$.

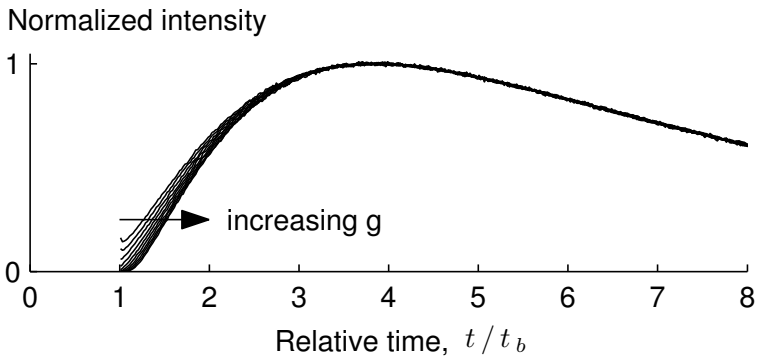

Figure 6.2 – Simulated time-resolved total transmission for a turbid slab with $L/\ell_t = 8$ for $g = 0.0, 0.1, ..., 0.9$ (n_i=1.5, n_e=1). Clearly, even deep into the multiple scattering regime, early dynamics can exhibit a significant dependence on g. This similarity breaking is clear evidence of diffusion breakdown. That a larger g (more forward scattering) reduce that amount of early light is related to that the unscattered intensity decays with depth z as $\exp(-z/\ell_s)$, and that having g approach one while keeping ℓ_t fixed is accompanied by a reduction of ℓ_s.

6.4.2 Sample preparation

We have studied the time-resolved transmission of light through a 252 μm thick turbid slab, prepared by dispersing 1 vol% of TiO_2 nano-particles in a monomer. Titanium dioxide nanoparticles belongs to the Tioxide R-XL series sold by Huntsman, which have an average diameter of 280 nm and are coated with an inorganic layer (silica, aluminia) to prevent clustering. We calculated an average refractive index $n = 2.4$ considering the refractive index of titanium dioxide for both light polarization directions. Mie calculations show that g is around 0.6. The monomer is the Norlan 65 acrylate optical adhesive from Thorlabs whose refractive index is $n = 1.52$. Nanoparticles are first homogeneously dispersed in the monomer by means of steering (10 minutes) and sonication (1 hour) at 50°, a temperature at which the monomer is fluid but does not polymerize. We did not use additional solvent to facilitate the dispersion since after some trials using dichloromethane (DCM) solvent residuals were still present in the final sample realization. The obtained diffusive paste is rather fluid at this stage. To host the paste we have prepared an hosting cell sticking together two microscope slides (thickness ≈1 mm) and inserting between them glass microspheres functioning as spacers. The thickness of the slides is measured separately before the cell preparation. The glue used for sticking is the same optical adhesive used to embed the nanoparticles. We have inserted the diffusive paste in the cell by infiltration, putting a small drop of paste on the cell border through a pipet and waiting that the paste was "sucked" by the cell for capillarity. In the last stage the filled cell is exposed to UV light to polymerize the monomer. Since the sample is diffusive 30 minutes of exposure are necessary to complete the polymerization. The thickness of the diffusive part is obtained measuring the thickness of the cell and subtracting the thickness of the single slides measured previously.

Since the volume percentage of nanoparticles is small their presence does not alter significantly the refractive index of the polymer. Moreover the refractive index of the glass slides matches that of the polymer. In turn this preparation technique creates an index matched condition at the sample boundaries. The achieved condition is sketched in fig. 6.3.

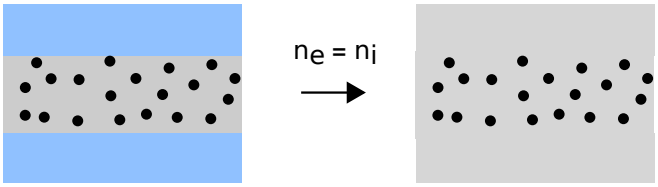

Figure 6.3 – Sample configuration, the diffusive medium is embedded between two microscope slides (in blu). The refractive index of the slides matches the effective refractive index of the medium so that optically the medium is index matched at the border

6.4.3 Experiments and simulations results

In order to measure the time-of-flight (TOF) distribution we have injected on the sample ultrashort pulses at 810 nm and collected the on-axis transmitted light. We have obtained time-resolved measurement by employing a non-linera optical gating technique. The setup used for the investigation is described in Chapter 3. A sketch describing the configuration of the optical elements used to inject and collect light is in fig. 3.4.

Evaluation of obtained experimental data against a database of MC simulations for different values of ℓ_t and g (using only walkers transmitted in the central 30 µm spot, in order to match experiment, but for simplicity assuming normal light incidence and full angular collection) reveals an optimal match for $g = 0.6$ and $\ell_t = 39$ µm (i.e., $\ell_s = 15.6$ µm). Fig. 6.4 shows the experimentally recorded TOF distribution along with simulations for different values of g for $\ell_t = 39$ µm, as well as the result of least squares matching.

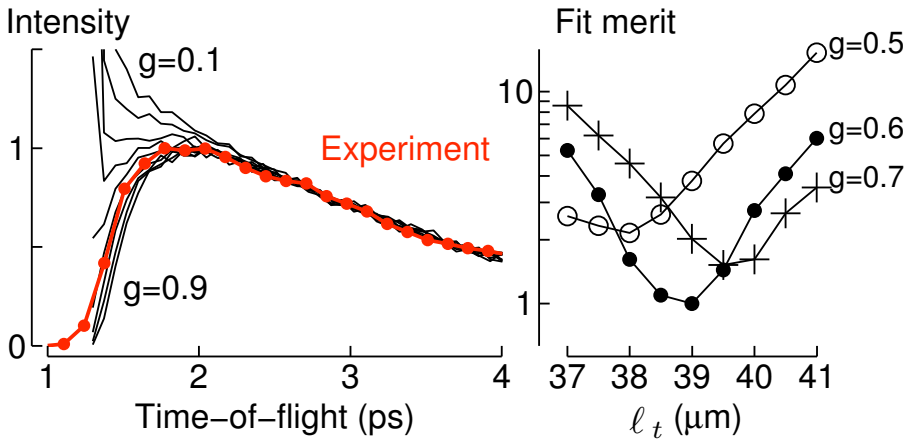

Figure 6.4 – Evaluation of experimental data based on MC. The left graph shows simulations for ℓ_t=39 µm and different g (0.1 to 0.9) and compares it with the experimental data. Experimental data is normalized to overlap with MC at late times where differences due to g are negligible. The right graph shows obtained fit merits (normalized to best fit) for the three best-matching g, revealing that the best least-squares fit is obtained for g=0.6 and ℓ_t=39 µm. Fitted ℓ_t agree well with measurements on thicker slabs of the same material, and fitted g is in good agreement with Mie calculations.

Fit merits indicate that the precision is better than ±0.1 for g, and ±1 µm for ℓ_t. The marked difference in g-dependence between Fig. 6.2 and Fig. 6.4 is related to the fact that the former considers total transmission, while the latter concerns detection of light from a small area around the optical axis. Throwing away a large part of the diffuse transmission naturally results in a different balance between the ballistic and quasi-ballistic component and the multiply scattered part. Note also that L/ℓ_t is about 6.5, so established rules of thumb [40] imply that diffusion theory should

fail to describe even late time behavior. However, the late-time decay of the total transmission obtained from MC (τ=3.6 $\pm$ 0.1 ps) is in good agreement with the predictions of diffusion theory (τ_D=3.60 ps). The reason behind this agreement is that the validity of diffusion theory decreases with the refractive index contrast [40], and we are now studying the forgiving case $n_i = n_e$.

Bibliography

[1] Pierre Barthelemy, Jacopo Bertolotti, and Diederik S. Wiersma. A Lévy flight for light. *Nature*, 453(7194):495–498, 2008.

[2] T. Svensson, K. Vynck, M. Grisi, R. Savo, M. Burresi, and D. S. Wiersma. Holey random walks: optics of heterogeneous turbid composites. *arXiv [cond-mat.dis-nn]*, 1211:1211.1954, 2012.

[3] T. Svensson, E. Adolfsson, M. Burresi, R. Savo, C. Xu, D. Wiersma, and S. Svanberg. Pore size assessment based on wall collision broadening of spectral lines of confined gas: experiments on strongly scattering nanoporous ceramics with fine-tuned pore sizes. *Appl. Phys. B*, pages 1–8, 2012.

[4] Tomas Svensson, Romolo Savo, Erik Alerstam, Kevin Vynck, Matteo Burresi, and Diederik S. Wiersma. Exploiting breakdown of the similarity relation for diffuse light transport: simultaneous retrieval of scattering anisotropy and diffusion constant. *arXiv [physics.optics]*, 1211:1211.6690, 2012.

[5] M.S. Patterson, B. Chance, and B.C. Wilson. Time resolved reflectance and transmittance for the noninvasive measurement of tissue optical-properties. *Appl. Opt.*, 28(12):2331–2336, June 1989.

[6] John David Jackson. *Classical Electrodynamics Third Edition*. Wiley, 3 edition, August 1998.

[7] M. I. Mishchenko. Maxwell's equations, radiative transfer, and coherent backscattering: A general perspective. *Journal of Quantitative Spectroscopy and Radiative Transfer*, 101(3):540–555, 2006.

[8] É. Akkermans and G. Montambaux. *Mesoscopic physics of electrons and photons*. Cambridge University Press, 2007.

[9] H. C. van de Hulst. *Light scattering by small particles*. Dover publications, 1981.

[10] C.F. Bohren and D.R. Huffman. *Absorption and scattering of light by small particles*. Wiley, 1983.

[11] A. Ishimaru. *Wave Propagation and Scattering in Random Media*. IEEE Press Series on Electromagnetic Wave Theory. IEEE Press, 1999.

[12] A. Ishimaru. *Wave propagation and scattering in random media*. Academic Press, 1978.

[13] Michael I. Mishchenko, Larry D. Travis, and Andrew A. Lacis. *Multiple scattering of light by particles: radiative transfer and coherent backscattering*. Cambridge University Press, 2006.

[14] E. Alerstam. *Optical spectroscopy of turbid media: time-domain measurements and accelerated Monte Carlo modelling*. PhD thesis, Lund University, 2011.

[15] C. F. Bohren. *Clouds in a glass of beer: simple experiments in atmospheric physics*. Wiley New York, 1987.

[16] Pierre-Etienne Wolf and Georg Maret. Weak localization and coherent backscattering of photons in disordered media. *Physical Review Letters*, 55(24):2696, December 1985.

[17] Meint P. Van Albada and Ad Lagendijk. Observation of weak localization of light in a random medium. *Physical Review Letters*, 55(24):2692, December 1985.

[18] M. H. Eddowes, T. N. Mills, and D. T. Delpy. Monte carlo simulations of coherent backscatter for identification of the optical coefficients of biological tissues in vivo. *Applied Optics*, 34(13):2261–2267, May 1995.

[19] Ad Lagendijk, Bart van Tiggelen, and Diederik S. Wiersma. Fifty years of anderson localization. *Physics Today*, 62(8):24–29, 2009.

[20] Ashley J. Welch and Martin J. C. Gemert. *Optical-Thermal Response of Laser-Irradiated Tissue*. Springer, 2010.

[21] André Liemert and Alwin Kienle. Analytical solution of the radiative transfer equation for infinite-space fluence. *Phys. Rev. A*, 83(1):015804, January 2011.

[22] André Liemert and Alwin Kienle. Analytical green's function of the radiative transfer radiance for the infinite medium. *Phys. Rev. E*, 83(3):036605–, March 2011.

[23] L. Wang and S.L. Jacques. *Monte Carlo modeling of light transport in multi-layered tissues in standard C*, 1998.

[24] A. Kienle and M.S. Patterson. Determination of the optical properties of turbid media from a single Monte Carlo simulation. *Phys. Med. Biol.*, 41(10):2221–2227, October 1996.

[25] D. Contini, F. Martelli, and G. Zaccanti. Photon migration through a turbid slab described by a model based on diffusion approximation: I. Theory. *Appl. Opt.*, 36(19):4587–4599, July 1997.

[26] T. Durduran, A.G. Yodh, B. Chance, and D.A. Boas. Does the photon-diffusion coefficient depend on absorption? *J. Opt. Soc. Am. A*, 14(12):3358–3365, December 1997.

[27] F. Reif. *Fundamentals of statistical and thermal physics*, volume 11. McGraw-Hill New York, 1965.

[28] L. Vlahos, H. Isliker, Y. Kominis, and K. Hizanidis. Normal and anomalous diffusion: A tutorial. *arXiv preprint arXiv:0805.0419*, 2008.

[29] B. V. Gnedenko and A. N. Kolmogorov. *Limit Distribution for sums of independent random variables.* Addison-Wesley Publishing Company, 1968.

[30] D. S. Wiersma, A. Muzzi, M. Colocci, and R. Righini. Time-resolved anisotropic multiple light scattering in nematic liquid crystals. *Physical review letters*, 83(21):4321–4324, 1999.

[31] D. S. Wiersma, A. Muzzi, M. Colocci, and R. Righini. Time-resolved experiments on light diffusion in anisotropic random media. *Physical Review E*, 62(5):6681, 2000.

[32] E. Alerstam and T. Svensson. Observation of anisotropic diffusion of light in compacted granular porous materials. *Physical Review E*, 85(4):040301, 2012.

[33] J. X. Zhu, D. J. Pine, and D. A. Weitz. Internal reflection of diffusive light in random media. *Physical Review A*, 44(6):3948, 1991.

[34] Ad Lagendijk, Rob Vreeker, and Pedro De Vries. Influence of internal reflection on diffusive transport in strongly scattering media. *Physics Letters A*, 136(1-2):81–88, March 1989.

[35] M. Born and E. Wolf. *Principles of optics: electromagnetic theory of propagation, interference and diffraction of light.* Cambridge university press, 1999.

[36] F. Martelli, S.D. Bianco, A. Ismaelli, and G. Zaccanti. *Light Propagation Through Biological Tissue and Other Diffusive Media: Theory, Solutions, and Software.* SPIE Press, 2009.

[37] S. R. Arridge, M. Cope, and DT Delpy. The theoretical basis for the determination of optical pathlengths in tissue: temporal and frequency analysis. *Physics in medicine and biology*, 37(7):1531, 2000.

[38] T. J. Huisman. Faster than diffusive light. *Internship Thesis*, 2011.

[39] R. Elaloufi, R. Carminati, and J.-J. Greffet. Time-dependent transport through scattering media: from radiative transfer to diffusion. *Journal of Optics A: Pure and Applied Optics*, 4(5):S103, 2002.

[40] Rachid Elaloufi, Rémi Carminati, and Jean-Jacques Greffet. Diffusive-to-ballistic transition in dynamic light transmission through thin scattering slabs: a radiative transfer approach. *J. Opt. Soc. Am. A*, 21(8):1430–1437, August 2004.

[41] I. M. Vellekoop. Time resolved measurements on diffusion of light. 2003.

[42] Erik Alerstam, Tomas Svensson, and Stefan Andersson-Engels. Parallel computing with graphics processing units for high-speed Monte Carlo simulation of photon migration. *J Biomed. Opt.*, 13(6):060054, 2008.

[43] W. L. Dunn and J. K. Shultis. *Exploring Monte Carlo Methods*. Elsevier Science, 2011.

[44] http://mathworld.wolfram.com/SpherePointPicking.html, December 2012.

[45] A. B. Davis. *Radiation Transport in Scale Invariant Optical Media*. PhD thesis, MCGILL UNIVERSITY (CANADA), January 1992.

[46] A.B. Davis, A. Marshak, and K.P. Pfeilsticker. Anomalous Lévy photon diffusion theory: toward a new parameterization of shortwave transport in cloudy columns. *9th ARM Science Team Meeting Proceedings*, 1999.

[47] Daniel ben Avraham and Shlomo Havlin. *Diffusion and reactions in fractals and disordered systems*. Cambridge University Press, 2000.

[48] Aristide Dogariu, Jun Uozumi, and Toshimitsu Asakura. Enhancement factor in the light backscattered by fractal aggregated media. *Optical Review*, 3(2):71–82, March 1996.

[49] Katsuhiro Ishii, Toshiaki Iwai, and Toshimitsu Asakura. Polarization properties of the enhanced backscattering of light from the fractal aggregate of particles. *Optical Review*, 4(6):643–647, November 1997.

[50] M. E. Cates. Brownian dynamics of self-similar macromolecules. *Journal de Physique*, 46(7):19, 1985.

[51] E. Bonnet, O. Bour, N. E. Odling, P. Davy, I. Main, P. Cowie, and B. Berkowitz. Scaling of fracture systems in geological media. *REVIEWS OF GEOPHYSICS-RICHMOND VIRGINIA THEN WASHINGTON-*, 39(3):347–384, 2001.

[52] L. De Arcangelis, A. Hansen, HJ Herrmann, and S. Roux. Scaling laws in fracture. *Physical Review B*, 40(1):877, 1989.

[53] S. Havlin, SV Buldyrev, AL Goldberger, RN Mantegna, SM Ossadnik, C. K. Peng, M. Simons, and HE Stanley. Fractals in biology and medicine. *Chaos, Solitons & Fractals*, 6:171–201, 1995.

[54] J. H. Brown, V. K. Gupta, B. L. Li, B. T. Milne, C. Restrepo, and G. B. West. The fractal nature of nature: power laws, ecological complexity and biodiversity. *Philosophical Transactions of the Royal Society of London. Series B: Biological Sciences*, 357(1421):619–626, 2002.

[55] C. Song, S. Havlin, and H. A. Makse. Self-similarity of complex networks. *Nature*, 433(7024):392–395, 2005.

[56] A. L. Barabási and R. Albert. Emergence of scaling in random networks. *science*, 286(5439):509–512, 1999.

[57] Rainer Klages, Gunter Radons, and Igor M. Sokolov. *Anomalous Transport: Foundations and Applications*. Wiley-VCH, September 2008.

[58] B. B. Mandelbrot. *The fractal geometry of nature*. Times Books, 1982.

[59] Shlomo Havlin and Daniel Ben-Avraham. Diffusion in disordered media. *Advances in Physics*, 51:187–292, 2002.

[60] O. Malcai, D. A. Lidar, O. Biham, and D. Avnir. Scaling range and cutoffs in empirical fractals. *Physical Review E*, 56(3):2817, 1997.

[61] Jean-Philippe Bouchaud and Antoine Georges. Anomalous diffusion in disordered media: Statistical mechanisms, models and physical applications. *Phys. Rep.*, 195(4-5):127–293, November 1990.

[62] S. Havlin, R. Nossal, B. Trus, and G. H. Weiss. Photon migration in disordered media. *Physical Review A*, 45:7511–7519, 1992.

[63] J. Klafter, G. Zumofen, and A. Blumen. Non-Brownian transport in complex systems. *Chemical Physics*, 177(3):821–829, December 1993.

[64] S. Condamin, O. Benichou, V. Tejedor, R. Voituriez, and J. Klafter. First-passage times in complex scale-invariant media. *Nature*, 450:77–80, 2007.

[65] Raffaella Burioni, Luca Caniparoli, and Alessandro Vezzani. Lévy walks and scaling in quenched disordered media. *Physical Review E*, 81(6):060101, June 2010.

[66] J. Nolan. *Stable distributions: models for heavy-tailed data*. Birkhauser, 2003.

[67] GM Viswanathan, S. V. Buldyrev, S. Havlin, MGE Da Luz, EP Raposo, and H. E. Stanley. Optimizing the success of random searches. *Nature*, 401(6756):911–914, 1999.

[68] L. Hufnagel, D. Brockmann, and T. Geisel. Forecast and control of epidemics in a globalized world. *Proceedings of the National Academy of Sciences of the United States of America*, 101(42):15124–15129, 2004.

[69] D. Brockmann, L. Hufnagel, and T. Geisel. The scaling laws of human travel. *Nature*, 439(7075):462–465, 2006.

[70] Rosario N. Mantegna and H. Eugene Stanley. Scaling behaviour in the dynamics of an economic index. *Nature*, 376:46–49, 1995.

[71] G. Zumofen and J. Klafter. Scale-invariant motion in intermittent chaotic systems. *Physical Review E*, 47:851–863, 1993.

[72] P. Lévy and M. É. Borel. *Théorie de l'addition des variables aléatoires*, volume 1. Gauthier-Villars Paris, 1954.

[73] A. Janiki and A. Weron. *Simulation and Chaotic Behavior of Stable Processes*. M. Dekker, New York, 1993.

[74] R. Metzler and J. Klafter. The restaurant at the end of the random walk: recent developments in the description of anomalous transport by fractional dynamics. *Journal of Physics A: Mathematical and General*, 37(31):R161, 2004.

[75] Ralf Metzler and Joseph Klafter. The random walk's guide to anomalous diffusion: a fractional dynamics approach. *Physics Reports*, 339(1):1–77, December 2000.

[76] PM Drysdale and PA Robinson. Lévy random walks in finite systems. *Physical Review E*, 58(5):5382, 1998.

[77] T. H. Solomon, Eric R. Weeks, and Harry L. Swinney. Observation of anomalous diffusion and lévy flights in a two-dimensional rotating flow. *Phys. Rev. Lett.*, 71(24):3975–, December 1993.

[78] A. Ott, J. P. Bouchaud, D. Langevin, and W. Urbach. Anomalous diffusion in "living polymers": A genuine levy flight? *Phys. Rev. Lett.*, 65(17):2201–, October 1990.

[79] K. M. Douglass, S. Sukhov, and A. Dogariu. Superdiffusion in optically controlled active media. *Nature Photonics*, 6(12):834–837, 2012.

[80] PP Zabreyko, AI Koshelev, MA Krasnosel'skii, SG Mikhlin, LS Rakovshchik, and V. Y. Stet'senko. *Integral equations: A reference text*. Noordhoff International Publishing Leyden, 1975.

[81] A. Davis and A. Marshak. *Fractal Frontiers*, chapter Lévy kinetics in slab geometry: scaling of transmission probability, pages 63–72. World Scientific, Singapore, 1997.

[82] S. V. Buldyrev, S. Havlin, A. Ya. Kazakov, M. G. E. da Luz, E. P. Raposo, H. E. Stanley, and G. M. Viswanathan. Average time spent by lévy flights and walks on an interval with absorbing boundaries. *Physical Review E*, 64(4):041108, 2001.

[83] K. M. Yoo and R. R. Alfano. Time-resolved coherent and incoherent components of forward light scattering in random media. *Opt. Lett.*, 15(6):320–322, Mar 1990.

[84] Rik H. J. Kop, Pedro de Vries, Rudolf Sprik, and Ad Lagendijk. Observation of anomalous transport of strongly multiple scattered light in thin disordered slabs. *Phys. Rev. Lett.*, 79(22):4369–4372, December 1997.

[85] I. M. Vellekoop, P. Lodahl, and A. Lagendijk. Determination of the diffusion constant using phase-sensitive measurements. *Phys. Rev. E*, 71(056604: 1-11):056604, 05/2005 2005.

[86] R. Sapienza, P. Costantino, D. Wiersma, M. Ghulinyan, C. J. Oton, and L. Pavesi. Optical analogue of electronic bloch oscillations. *Physical review letters*, 91(26):263902, 2003.

[87] R. Trebino. *Frequency-resolved optical gating: the measurement of ultrashort laser pulses*. Springer, 2000.

[88] J. Shah. Ultrafast luminescence spectroscopy using sum frequency generation. *Quantum Electronics, IEEE Journal of*, 24(2):276–288, 1988.

[89] AG Yodh, PD Kaplan, and DJ Pine. Pulsed diffusing-wave spectroscopy: high resolution through nonlinear optical gating. *Physical Review B*, 42:4744–4747, 1990.

[90] C. Toninelli, E. Vekris, G. A. Ozin, S. John, and D. S. Wiersma. Exceptional reduction of the diffusion constant in partially disordered photonic crystals. *Physical review letters*, 101(12):123901, 2008.

[91] L. Dal Negro, C. J. Oton, Z. Gaburro, L. Pavesi, P. Johnson, A. Lagendijk, R. Righini, M. Colocci, and D. S. Wiersma. Light transport

through the band-edge states of fibonacci quasicrystals. *Physical review letters*, 90(5):55501, 2003.

[92] R. W. Boyd. *Nonlinear optics*. Academic press, 2002.

[93] Y. R. Shen. The principles of nonlinear optics. *New York, Wiley-Interscience, 1984, 575 p.*, 1, 1984.

[94] R. Trebino. Second-harmonic-generation rings and refractive-index measurement in uniaxial crystals. *Applied Optics*, 20(12):2090–2096, 1981.

[95] H. Rhee and T. Joo. Noncollinear phase matching in fluorescence upconversion. *Optics letters*, 30(1):96–98, 2005.

[96] R. Carminati, J. J. Sáenz, J. J. Greffet, and M. Nieto-Vesperinas. Reciprocity, unitarity, and time-reversal symmetry of the s matrix of fields containing evanescent components. *Physical Review A*, 62(1):012712–, 06 2000.

[97] Tomas Svensson, Erik Adolfsson, Märta Lewander, Can T. Xu, and Sune Svanberg. Disordered, strongly scattering porous materials as miniature multipass gas cells. *Phys. Rev. Lett.*, 107(14):143901, September 2011.

[98] D. L. Wood and K. Nassau. Refractive-index of cubic zirconia stabilized with yttria. *Appl. Opt.*, 21(16):2978–2981, 1982.

[99] Leonid A. Dombrovsky, Herve Kamdem Tagne, Dominique Baillis, and Laurent Gremillard. Near-infrared radiative properties of porous zirconia ceramics. *Infrared Phys. Techn.*, 51(1):44–53, July 2007.

[100] J. Manara, R. Caps, and J. Fricke. Characterization of the pore structure of ceramics via propagation of light and infrared radiation. *Int. J. Thermophys.*, 26:531–542, 2005.

[101] Jacopo Bertolotti, Kevin Vynck, Lorenzo Pattelli, Pierre Barthelemy, Stefano Lepri, and Diederik S. Wiersma. Engineering disorder in superdiffusive lévy glasses. *Advanced Functional Materials*, 20(6):965–968, 2010.

[102] Matteo Burresi, Vivekananthan Radhalakshmi, Romolo Savo, Jacopo Bertolotti, Kevin Vynck, and Diederik S. Wiersma. Weak localization of light in superdiffusive random systems. *Phys. Rev. Lett.*, 108(11):110604, March 2012.

[103] Pierre Barthelemy, Jacopo Bertolotti, Kevin Vynck, Stefano Lepri, and Diederik S. Wiersma. Role of quenching on superdiffusive transport in two-dimensional random media. *Physical Review E*, 82(1):011101, July 2010.

[104] Jacopo Bertolotti, Kevin Vynck, and Diederik S. Wiersma. Multiple scattering of light in superdiffusive media. *Phys. Rev. Lett.*, 105(16):163902–, October 2010.

[105] Raffaella Burioni, Luca Caniparoli, and Alessandro Vezzani. Lévy walks and scaling in quenched disordered media. *Phys. Rev. E*, 81(6):060101, June 2010.

[106] Raffaella Burioni, Luca Caniparoli, Stefano Lepri, and Alessandro Vezzani. Lévy-type diffusion on one-dimensional directed Cantor graphs. *Phys. Rev. E*, 81(1):011127, January 2010.

[107] P. Buonsante, R. Burioni, and A. Vezzani. Transport and scaling in quenched two- and three-dimensional Lévy quasicrystals. *Phys. Rev. E*, 84(2):021105, August 2011.

[108] C. W. Groth, A. R. Akhmerov, and C. W. J. Beenakker. Transmission probability through a lévy glass and comparison with a lévy walk. *Physical Review E*, 85:021138, 2012.

[109] Gordon L. Olson, David S. Miller, Edward W. Larsen, and Jim E. Morel. Chord length distributions in binary stochastic media in two and three dimensions. *J. Quant. Spectrosc. Radiat. Transfer*, 101(2):269–283, September 2006.

[110] W. J. M. De Kruijf and J. L. Kloosterman. On the average chord length in reactor physics. *Ann. Nucl. Energy*, 30(5):549–553, 2003.

[111] S. Torquato and B. Lu. Chord-length distribution function for two-phase random media. *Phys. Rev. E*, 47(4):2950–2953, April 1993.

[112] David Guéron and Alain Mazzolo. Properties of chord length distributions across ordered and disordered packing of hard disks. *Phys. Rev. E*, 68(6):066117, December 2003.

[113] S. Torquato. *Random Heterogeneous Materials: Microstructure and Macroscopic Properties*. Springer, 2001.

[114] K.M. Yoo, F. Liu, and R.R. Alfano. When does the diffusion-approximation fail to describe photon transport in random-media? *Phys. Rev. Lett.*, 64(22):2647–2650, 1990.

[115] R. Graaff, J.G. Aarnoudse, F.F.M. Demul, and H.W. Jentink. Similarity relations for anisotropic scattering in absorbing media. *Opt. Eng.*, 32(2):244–252, February 1993.

[116] Edward Vitkin, Vladimir Turzhitsky, Le Qiu, Lianyu Guo, Irving Itzkan, Eugene B. Hanlon, and Lev T. Perelman. Photon diffusion near the point-of-entry in anisotropically scattering turbid media. *Nat. Commun.*, 2:587, December 2011.

[117] D. J. Durian and J. Rudnick. Photon migration at short times and distances and in cases of strong absorption. *J. Opt. Soc. Am. A*, 14(1):235–245, January 1997.

[118] V. Ntziachristos and B. Chance. Accuracy limits in the determination of absolute optical properties using time-resolved NIR spectroscopy. *Medical Physics*, 28(6):1115–1124, 2001.

[119] Ad Lagendijk and Bart A. van Tiggelen. Resonant multiple scattering of light. *Phys. Rep.*, 270:143–215, 1996.

[120] R. Pierrat, L. J. Greffet, and R. Carminati. Photon diffusion coefficient in scattering and absorbing media. *J. Opt. Soc. Am. A*, 23(5):1106–1110, May 2006.

[121] A. Pifferi, P. Taroni, G. Valentini, and S. Andersson-Engels. Real-time method for fitting time-resolved reflectance and transmittance measurements with a Monte Carlo models. *Appl. Opt.*, 37(13):2774–2780, May 1998.

[122] E. Alerstam, S. Andersson-Engels, and T. Svensson. White Monte Carlo for time-resolved photon migration. *J. Biomed. Opt.*, 13:041304, 2008.

[123] E. Alerstam, S. Andersson-Engels, and T. Svensson. Improved accuracy in time-resolved diffuse reflectance spectroscopy. *Opt. Express*, 16(14):10440–10454, 2008.

[124] T. Svensson, E. Alerstam, M. Einarsdóttír, K. Svanberg, and S. Andersson-Engels. Towards accurate in vivo spectroscopy of the human prostate. *J. Biophoton.*, 1(3):200–203, 2008.

[125] Jean-Pierre Bouchard, Israël Veilleux, Rym Jedidi, Isabelle Noiseux, Michel Fortin, and Ozzy Mermut. Reference optical phantoms for diffuse optical spectroscopy. part 1 – error analysis of a time resolved transmittance characterization method. *Opt. Express*, 18(11):11495–11507, 2010.

[126] DR Kirkby and DT Delpy. Parallel operation of monte carlo simulations on a diverse network of computers. *Physics in medicine and biology*, 42(6):1203, 1999.

[127] A. Colasanti, G. Guida, A. Kisslinger, R. Liuzzi, M. Quarto, P. Riccio, G. Roberti, and F. Villani. Multiple processor version of a monte carlo code for photon transport in turbid media. *Computer physics communications*, 132(1-2):84–93, 2000.

[128] D. Blythe. Rise of the graphics processor. *P. IEEE*, 96(5):761–778, 2008.

[129] C. Nvidia. Nvidia cuda programming guide, 2011.

[130] Qianqian Fang and David A. Boas. Monte Carlo simulation of photon migration in 3D turbid media accelerated by graphics processing units. *Opt. Express*, 17(22):20178–20190, Oct 2009.

[131] N. Ren, J. Liang, X. Qu, J. Li, B. Lu, and J. Tian. Gpu-based monte carlo simulation for light propagation in complex heterogeneous tissues. *Optics express*, 18(7):6811–6823, 2010.

[132] L.G. Henyey and J.L. Greenstein. Diffuse radiation in the galaxy. *Astrophys. J.*, 93(1):70–83, 1941.

Summary

In this work we investigate experimentally, numerically and theoretically the dynamic features of light transport in disordered media, focusing on the effects produced by the disorder heterogeneity. We consider three different situations: a fractal-like heterogeneity, a generic distribution of heterogeneities with sizes smaller that the size of the system and the homogeneous disorder case.

In Chapter 1 and Chapter 2 , which are an introductory part, we give the ingredients to link the properties of light transport in disordered media with those of anomalous transport in heterogeneous fractal systems. When the disorder is heterogeneous at all length scale (fractal), the transport is expected to be anomalous. We focus on the differences between the diffusive and the superdiffusive transport regime on finite systems, looking for characteristic dynamic observables which can be measured in a lab by optical characterizations. We find that, in theory, the dependence on the system size (the *scaling*) of the decay constant of a time-resolved transmission can discern between diffusive and superdiffusive dynamics.

In Chapter 3 we describe the optical-gating setup used for measuring the time-resolved transmission of the investigated structures. Our experimental implementation gives a very good stability (drift less than 1 fs in 1 hour), temporal resolution (femtosecond scale), dynamic range (seven order of magnitude in principle). We show test measurements performed on homogeneous disordered samples for two different optical configurations. The setup is able to resolve in time both the on-axis transmission and the total-transmission, depending on the optical components used to collect the light. By injecting light with a collimated beam and by collecting the on-axis light we show evidence of reciprocity for diffused light. We also characterize the optical transport properties of zirconia nanoporous ceramics, observing that the measured transport-mean-free path depends on the degree of porosity.

In Chapter 4 we investigate the pulse response of Lévy glasses by total-transmission time-resolved measurements.We observe peculiar intensity fluctuations at earlier time, caused by the strong heterogeneity of the disorder, and an exponentially decaying long-time transmission. We investigate the dependence of the long-time lifetime on the thickness of the sample for two values of the fractal parameter β. In both cases we observe an anomalous scaling of the lifetime, which deviates from the diffusive one. The measured exponents are significantly smaller than one, which is a dynamical feature expected for superdiffusive transport. We discuss the possible effects of the sample boundaries on the measured exponents, which could be characteristic of a pre-asymptotic transport regime. We propose a first method to retrieve the asymptotic value of the scaling exponent, which, in the considered assumptions, represents the walk dimensions of light inside the sample. The obtained walk dimensions are still significantly smaller than one, allowing for a rescaling of the axis which produce a very good collapse of the data. These dynamical signatures of superdiffusion have never been observed before. Moreover our experimental scaling analysis results to be sensitive to the degree of heterogeneity of the samples. It could represent an innovative investigation method to assess structural informations in generic optical heterogeneous media.

In Chapter 5 we investigate, theoretically and numerically, the effects on transport of scatterers voids in unbounded systems. Via a simple model of the quenched disorder we derive analytical expressions for the mean step, the mean squared step, the diffusion constant and void crossing probabilities. We show that the mean step equals the homogenized (exponential) scattering mean free path, being dependent only on void filling fraction. Moreover we derive that for holey systems in the form of random sphere packings, in the limit of weak scattering, the asymptotic diffusion constant is affected by the presence of the non scattering regions. All the theoretical results are well supported by Monte Carlo simulations of random walks in holey systems based on random sphere packings. We finally present transport simulations in a 3D ideal Lévy glass, with exponentially spaced spheres categories. This simulations gives important insights into the affect of quenching and spheres multicrossing in a Lévy glass-like system. Given the abundance of turbid materials where scatterers are not homogeneously distributed, we believe that both our viewpoint and our results can be of value for a wide range of topics, from fundamental work on light transport to applied spectroscopy of heterogeneous media such as biological tissues, food products, and powder compacts.

In Chapter 6 we investigate light transport dynamics at early time in homogeneous disordered slabs. We work in the regime of diffusion breakdown and of similarity breakdown. By comparing experiments with simulations we show that single scattering characteristics (g and ℓ_s) can be inferred by multiply scattered light also after long propagation distances. The accuracy

and precision of the approach depends on the transport regime (e.g. L/ℓ_t) and the details of angular collection and conversion, being important matters to be addressed in future research. Insights beyond the simplicity of the HG phase function are also needed, since the shape of the phase function impact similarity breakdown. Finally, it should be noted that measurements do not require ultrafast setups *per se*, as required temporal stability and resolution depends on system scale. We therefore anticipate widespread applicability of the approach, from characterization of turbid liquids and porous media to biological tissues.

List of publications

Publications related to this thesis:

- T. Svensson, E. Adolfsson, M. Burresi, R. Savo, C. T. Xu, D. S. Wiersma, S. Svanberg, *Pore size assessment based on wall collision broadening of spectral lines of confined gas: experiments on strongly scattering nanoporous ceramics with fine-tuned pore sizes*, Applied Physics B, pages 1-8, (2012))

- Tomas Svensson, Romolo Savo, Erik Alerstam, Kevin Vynck, Matteo Burresi, and Diederik S. Wiersma, *Exploiting breakdown of the similarity relation for diffuse light transport: simultaneous retrieval of scattering anisotropy and diffusion constant*, on the arXiv (2012), (Accepted by Optics Letters).

- Tomas Svensson, Kevin Vynck, Marco Grisi, Romolo Savo, Matteo Burresi, and Diederik S. Wiersma, *Holey Random Walks: Optics of Heterogenous Turbid Composites*, on the arXiv (2012)

- Romolo Savo, Matteo Burresi, Kevin Vynck, Tomas Svensson and Diederik S. Wiersma, *Observation of anomalous scaling of light dynamic in heterogeneous fractal-like disordered media*, In preparation

Other publications:

- M. Burresi, V. Radhalakshmi, R. Savo, J. Bertolotti, K. Vynck, D.S. Wiersma, *Weak localization of light in superdiffusive random systems*, Phys. Rev. Lett. 108, 110604 (2012)

- P.Orgiani, A.Guarino, C.Aruta, C.Adamo, A.Galdi, A.Y.Petrov, R.Savo and L.Maritato, *Magnetotransport Properties of epitaxial strain-less La0.7Ba0.3MnO3 thin films*, Journal of Applied Physics,101,033904,(2007)

Acknowledgements

This thesis is the result of team work in trying to solve (what I think has been) a rather complicated "puzzle", that is why I'm very proud of all the efforts, knowledge and creativity we putted in.

All the work has been carried out at LENS-European Laboratory for Nonlinear Spectroscopy in Sesto Fiorentino (Firenze), a very nice and exciting environment for research. I want to thanks all the staff (scientific and administrative) for their support.

I want to thank Diederik. He gave me the freedom to learn and to be wrong, but in particular some precious hints I will bring with me.

I'm very grateful to "my" postdocs, who, in a sort of chronological order have been Matteo Burresi, Kevin Vynck and Tomas Svensson. Matteo, thanks for showing me how to align a couple of lenses. Everything started there. Kevin, thanks for you ability in placing the right concept in the right context. Tomas, all I know about time-resolved measurements is thanks to you (thanks also for the kindly phone call of tonight). I want to thank these guys also because during these three years they gave me their friendship, which has been as important as their scientific teachings.

I want to thank Raffaella Burioni e Alessandro Vezzani, who have been my lighthouse in the world of scaling. Thanks for your constant enthusiasm about my measurements (which sometimes has been bigger than mine!). Thanks to Erik Alerstam, for your contributions to this work. Thanks to Jacopo Bertolotti and Pierre Barthelemy, who started with Lévy glasses (should I really thank you?!).

I also want to thank many of the people from my group, from LENS or who has been at LENS for a short period, who have shared with me scientific and less scientific experiences. Thanks to Rajesh, who shared with me the pressure of a Phd thesis. To Jean-Cristophe, try to came back from Barcelona before I'll leave, we still have to go to the CUS. To Lorenzo, for saving me when I was out of gas. To Filippo, who termed me a"fructarian".

Giacomo, who are we going to vote this here in the end? To Sepideh, who believes that this research can be really interesting. To Camilla, who introduced me to the use of Steri-Strips. Thanks to Francesco, Francesca e Niccolò. To Sara, Hao, Hoa (Joyce), Piotr e Daniele. Thanks to Thomas (Huisman), for being in lab with me until two in the night. Thanks to Marco, for the nice time spent together (especially that OUT of the lab), and to Gora. Thanks to Karina, for the simple advises you gave me in the corridors.

I want to thank some of the people who, in the few spare time out of the lab, shared and enjoyed with me the last three years. Thanks to Sandra, and to the whole yoga class at the Shanti center, your teaching on how to use feet and lags have been very precious to conclude this work. Ringrazio Max, per il suo sforzo di passare per l'ufficio anche se non gli andava, le tue foto sono stupende anche per la scienza. Thanks to Nicco, who shared with me my first kilometers, and troubles, on a motorbike, "on these streets drawn among the hills". Thanks to all his family, I Brogelli. Thanks to Denny, my unofficial doctor here in Florence. Grazie ad Angelo, per le tue infinite storie di pesca.

I want to thank my brother Salvatore, who, being a good bigger brother and a good scientist, has spent these last few days reviewing the manuscript. And thanks to Rita, who just accepted to marry him. Thank to my mother, for having waited my phone calls more than what she could do . I say thanks to Ludo, especially becouse I never had to ask your support, you just gave it to me, as your love.

I finally want to remember my father, and say thanks to him as well. Eventually, we are not so far in the physics that we like.